7-11-2013

# Cryogenic optical refrigeration: Laser cooling of solids below 123 K

Seth Melgaard

Seth D. Melgaard
*Candidate*

Optical Science and Engineering
*Department*

This dissertation is approved, and it is acceptable in quality and form for publication:

*Approved by the Dissertation Committee:*

Mansoor Sheik-Bahae , Chairperson

Luke Lester

Kevin Malloy

Markus Hehlen

# Cryogenic optical refrigeration: Laser cooling of solids below 123 K

by

**Seth D. Melgaard**

B.S., Physics, Univ. of New Mexico, 2002
M.S., Optical Science and Engineering, Univ. of New Mexico, 2011

DISSERTATION

Submitted in Partial Fulfillment of the
Requirements for the Degree of

Doctorate of Philosophy
Optical Science and Engineering

The University of New Mexico

Albuquerque, New Mexico

February, 2013

# Dedication

*To my family*

# Acknowledgments

The scientific process is inherently collaborative. Seemingly insignificant suggestions can lead to wondrous insights and new discoveries. It is therefore impossible for me to be complete in acknowledging everyone who have impacted my life which led to the work presented in this dissertation. Additionally, the relatively small contributions I have made to science rests on the ideas of previous generations who have struggled to answer the questions preceding my own. There are however some obvious contributors I wish to acknowledge.

I would like to thank my advisor, Mansoor Sheik-Bahae, for his guidance, support and patience. I would also like to thank Denis Seletskiy for his knowledge, scientific understanding and most importantly his time. Mike Hasselbeck, Richard Epstein, Markus Hehlen and Kevin Malloy have graciously shared their insights and have given a piece of their experience on how to be a good scientist which I will no doubt continue to use throughout my own career. Working with fellow graduate students Chengao Wang, Chia-Yeh Li, Aram Gragossian, Zhou Yang and Mohammed Ghasemkhani has been pleasurable and enlightening.

I've had the joy of attending classes with many great teachers who inspired me through their own passions. Professors: Pedro Embid, Ron Lumia, Sudhakar Prasad, Nitant Kenkre, Rob Duncan and Vakhtang Putkaradze, each had an indispensable impact on me as a person and my life as a student.

My wife, my parents, my sister and my friends have all supported me without hesitation. Without them in my life, this work would be empty.

# Cryogenic optical refrigeration: Laser cooling of solids below 123 K

by

**Seth D. Melgaard**

B.S., Physics, Univ. of New Mexico, 2002
M.S., Optical Science and Engineering, Univ. of New Mexico, 2011

Ph.D., Optical Sciences and Engineering, University of New Mexico, 2013

## Abstract

This dissertation compiles recent achievements in optical refrigeration, cooling a 10% wt. Ytterbium doped Yttrium Lithium Fluoride ($Yb^{+3}$:YLF) crystal via anti-Stokes fluorescence to a record low temperature ~114±1K (below NIST-defined cryogenic 123 K) from room temperature ($\Delta$T ~185 K) in a single stage with a cooling power of 190mW. The demonstration of the coldest temperature to date, without the use of liquid cryogens or mechanical refrigerators, is achieved by taking advantage of the Stark manifold resonance and high doping concentration available in a crystalline host, outperforming multi-stage Peltier coolers. A novel technique probing local temperature changes experimentally verifies the cooling efficiency model with expected cooling to 93 K with the current crystal. With modest improvements to parasitic background absorption through the reduction of identified impurities, theory predicts cooling that approaches liquid nitrogen temperatures at 77 K. With this accomplishment, implementation of an all solid-state cryo-cooling has begun.

# Contents

# List of Figures

# Glossary

| | |
|---|---|
| $\eta_a$ | Absorption efficiency. |
| $\eta_c$ | Cooling efficiency. |
| $\eta_{ext}$ | External quantum efficiency. |
| $\eta_e$ | Extraction efficiency. |
| $\alpha_b$ | Parasitic background absorption. |
| $\alpha_r$ | Resonant absorption. |
| $P_{cool}$ | Cooling power. |
| $P_0$ | Incident pump power. |
| $P_{abs}$ | Absorbed power. |
| $P_{exit}$ | Unabsorbed pump power. |
| $Yb^{3+}$:YLF | Trivalent Ytterbium doped Yttrium Lithium Fluoride crystal. |
| $Yb^{3+}$:ZBLAN | Trivalent Ytterbium doped $ZrF_4$-$BaF_2$-$LaF_3$-$AlF_3$-NaF glass. |
| $Yb^{3+}$:ZBLANP | Trivalent Ytterbium doped $ZrF_4$-$BaF_2$-$LaF_3$-$AlF_3$-NaF-$PbF_2$ glass. |
| $S(\lambda)$ | Spectral density. |

| | |
|---|---|
| $W_{rad}$ | Radiative recombination rate. |
| $W_{nr}$ | Non-radiative recombination rate. |
| $\bar{\lambda}_f$ | Mean fluorescence wavelength. |
| $\lambda_{cross}$ | Zero crossing wavelength. |
| E$\|$c | Electric field oriented parallel to c, the crystal axis. |
| E$\perp$c | Electric field oriented perpendicular to c, the crystal axis. |
| TIR | Total internal reflection. |
| $\Omega_{cone}$ | Escape cone solid angle. |
| $\Omega_{ext}$ | Solid angle outside of the escape cone. |
| $F_{trapped}$ | Fraction of trapped photons due to total internal reflection. |
| DLT | Differential luminescence thermometry, see Appendix A. |
| SMA | Sub multi assembly fiber optic cable connector. |
| MAT | Minimum achievable temperature. |
| sMAT | Spectroscopic minimum achievable temperature. |
| gMAT | Global minimum achievable temperature. |
| Ti:Sa | Solid state laser, based on a sapphire crystal doped with titanium ions. |

# Chapter 1

# Introduction

The association between light and heat is universal. This association is understandable; simply move your hand near an illuminated lightbulb, walk outside into the sunlight, or sit next to a campfire on a cold evening. When light becomes more intense, the so does that perception of increased heat. Lasers, which generate high intensity light, have a reputation for destruction. Indeed practical applications use lasers for cutting and welding or remodeling the cornea, and less practically, a quick internet search reveals a method of heating coffee or modifying a laser pointer into a fire-starter. But there is a counterintuitive and arguably more interesting use: laser cooling. Lasers can be used to cool matter in gas, liquid or solid phase; with the two most developed fields dealing with gasses and solids. Even though the mechanisms are different for laser cooling of different phases, the same general principle applies: heat removal through energy transfer from low energy to high energy light. Laser cooling of gases is a well developed field achieving temperatures <1 nK by reducing the translational motion of atoms via doppler cooling, culminating in a Nobel Prize [1]. The cooling mechanism for solids is very different. The translational motion cannot be reduced because the atom locations in space are fixed by the surrounding atomic structure, therefore doppler cooling does not apply to a solid. There is

instead vibrational motion. This dissertation concentrates on the laser cooling process which reduces the vibrational motion of atoms in a solid through anti-Stokes fluorescence, also known as optical refrigeration. It should be understood that the minimum achievable temperature range for a solid is much higher than for gasses because of the constant interaction between atoms in a solid. Therefore solids are capable of somewhere between 10-100 K as a minimum temperature. The mechanism for cooling a solid is discussed in the Chapter 2, and provides the structure for the work presented in this dissertation. Included is the discussion of cooling performance, modeled by the cooling efficiency and cooling power.

The cooling performance in optical refrigeration has been dictated by the purity with which the solid is made. The optical fiber industry, also driven by the need for materials with impurities <100 parts per billion (ppb), has given optical refrigeration the opportunity to use as a host material the same fluorozirconate glass, ZBLAN and ZBLANP, used for optical fibers. Testing the cooling properties in other host materials, including crystals, was limited until recent advancements in starting material purity provided the opportunity. Chapter 3 develops an empirical model of the cooling efficiency in a new host material, Yttrium Lithium Fluoride (YLF), doped with the ternary rare-earth (RE) ion, Ytterbium ($Yb^{3+}$). Also included in this chapter is a discussion of the importance of host material as related to the cooling performance, as well as the benefits rare earths (RE) elements provide optical refrigeration and which RE to choose. The National Institute of Standards and Technology (NIST) has defined temperatures 150° below zero (or 123K) as a cryogenic temperature. Empirical modeling of the 5% wt. Ytterbium doped Yttrium Lithium Fluoride ($Yb^{3+}$:YLF) crystal predicts cooling down to ∼110 K which has been experimentally verified locally, classifying the performance as cryogenic. Additionally, a second 5% wt. $Yb^{3+}$:YLF crystal has cooled to 118 K, the global minimum achievable temperature (gMAT) for this sample, and a 10% wt. $Yb^{3+}$:YLF crystal has cooled to 114 K with potential to cool to 93 K. Further purity improvements discussed in

Ch. 6 provide a pathway for optical refrigeration to reach the liquid nitrogen ($LN_2$) temperature, 77 K, in solids.

Because of the cryogenic performance demonstrated via optical refrigeration, the potential to be used as a cryogenic cooling device is within reach. Sensitivity of many optical sensors increases at low temperature. The electron-multiplying charge-coupled device (EMCCD), for example, becomes 10× more sensitive at -70°C than at room temperature. Attaching an EMCCD sensor or any other device to a cooling crystal provides a stable cryogenic platform that improves performance. Space-born sensors are an excellent application. Satellites use sensors requiring even lower temperatures, and not only is maximum sensitivity necessary, but so is vibrational stability. Traditionally, the low temperature requirements have meant mechanical refrigerators are the only option to cool satellite sensors, even though these refrigerators have moving parts which introduce vibration and mechanically degrade over time. The driving force behind the advancements in optical refrigeration is the desire to reach cryogenic temperatures and develop an all solid-state optical cryocooler to be used on satellite as sensor cooling device. An all solid-state optical-cryocooler device, Fig. 1.1, is inherently vibration free, and can be designed to be light-weight, nimble, and compact. With no moving parts, the pump laser diode becomes the lifetime-limiting component of a solid-state optical cryocooler [2] and with (ever improving) lifetimes >100000 hours [3], reliability >10 years can be anticipated. When optical refrigeration satisfies the sensor temperature requirements, an all solid-state optical cryocooler will be the ideal replacement for the mechanical refrigerator for space-based applications. Chapter 4 presents the advancements in optical refrigeration which reached the coldest temperatures to date, 114 K, for any solid-state refrigeration by using a 10% wt. $Yb^{3+}$:YLF crystal. And with model predictions below 100 K, development of an all solid-state optical cryocooler is soon to be realized.

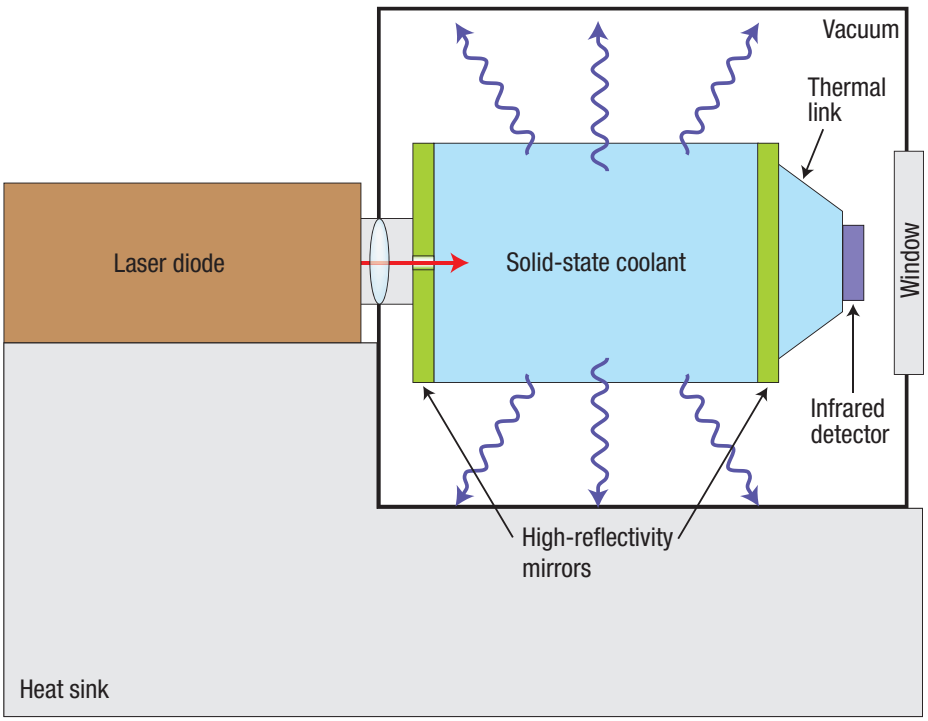


Figure 1.1: Conceptual representation of an all solid-state optical cryocooler. A pump source, in this case a laser diode, pumps the solid state cooler under vacuum, generating fluoresce. Heat is carried away by a heat sink. A detector attached to a thermal link is visible through a window.

## 1.1 Historical Background

A beautiful demonstration of the scientific process comes from the many years of research that preceded the ability to develop an optical refrigeration device. During the $19^{th}$ century, it was believed that light irradiated from a source must always be red-shifted (emit longer wavelengths) from the absorbed light. At the time it was called "Stokes' law" expressing the certitude with which this was believed and was stated: "the rays emitted by a fluorescent substance **always** have a smaller refrangibility than the exciting rays" [4]. Refrangibility is a term used to express the amount of deflection light undergoes through a prism, where red light has smaller refrangi-

bility than blue. Evidence to the contrary supporting the observation of blue-shifted fluorescence was emerging, however, and by the beginning of the $20^{th}$ century, anti-Stokes radiation was accepted though not yet understood. In 1929, Pringsheim first theorized the possibility of using anti-Stokes fluorescence to cool a fluorescent gas with radiation [5], because blue light has higher energy than red light. Disagreements emerged based on entropy, but Landau formally showed that the process does not violate the second law of thermodynamics [6] by assigning entropy to the fluorescence. Subsequently, Kastler proposed that not only gases, but rare-earth ions in transparent solids, could cool through anti-Stokes fluorescence [7]. The invention of the laser in the 1960's with narrow spectral power distribution, and later the purification of materials, led laser cooling of solids to realized its first experimental verification when Epstein et al. achieved net cooling of a 1 wt. % $Yb^{+3}$-doped ZBLANP ($ZrF_4$-$BaF_2$-$LaF_3$-$AlF_3$-NaF-$PbF_2$) glass [8], pumping near the $1\mu$m transition. Years of research followed [9, 10, 11, 12, 13], achieving the best performance of 208K [14] from room temperature with a highly purified $Yb^{3+}$:ZBLAN ($ZrF_4$-$BaF_2$-$LaF_3$-$AlF_3$-NaF) glass. Since then, cryogenic operation has been achieved and will be discussed in the following chapters of this dissertation.

So far the best performance has been accomplished utilizing the $Yb^{3+}$ rare-earth (RE) ion, however other trivalent RE ions have also been cooled. Both $Tm^{3+}$ and $Er^{3+}$ have been shown to cool [15, 16, 17, 18, 19], pumping around the $2\mu$m and $1.5\mu$m transitions respectively for the first excited state. Unlike the single 4f electronic state in $Yb^{3+}$, both thulium and erbium have multiple transition levels available for pumping, so it is also possible to utilize a higher energy transition for cooling [20, 21]. There are advantages for each of the different cooling ions, some of which will be discussed in Ch. 3, and others which still need to be investigated.

# Chapter 2

# Theory of Optical Refrigeration

Optical refrigeration in solids is achieved through anti-Stokes fluorescence. For the simplified case of a two manifold system, Fig. 2.1, radiation with energy h$\nu$ is absorbed by the cooling ion, exciting electrons from the top of the ground state manifold to the bottom of the excited state manifold. From there the electrons thermalize quickly ($\tau \approx 10^{-12}$s) by absorbing phonons. When the electrons relax back to the ground state radiatively ($\tau \approx 10^{-3}$s), a radiation is emitted with average energy h$\nu_f$>h$\nu$, removing the difference in energy and cooling the host. The cooling efficiency is defined as the ratio of the cooling power $P_{cool}$ to the absorbed power $P_{abs}$,

$$\eta_c = \frac{P_{cool}}{P_{abs}} = \frac{h\nu - h\nu_f}{h\nu} = \frac{\lambda_f - \lambda}{\lambda_f}, \tag{2.1}$$

with the emitted light having mean fluorescence energy h$\nu_f$ given by the expression

$$h\nu_f = \frac{\int h\nu\Phi(\nu)d\nu}{\int \Phi(\nu)d\nu}, \tag{2.2}$$

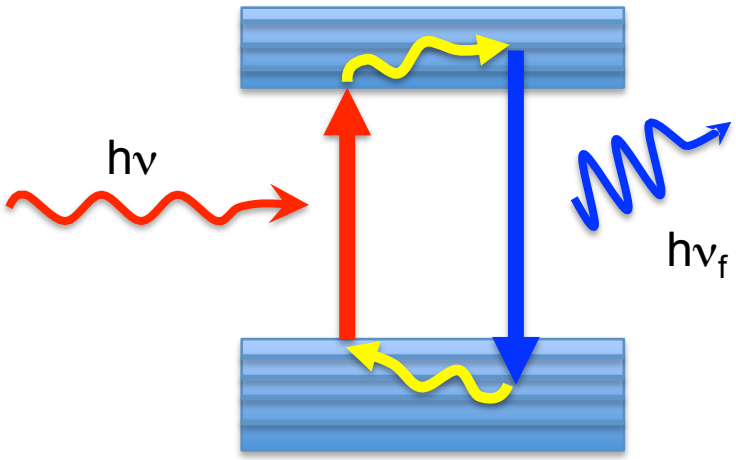


Figure 2.1: Ideal cooling cycle with ground state and excited state manifolds.

where $\Phi(\nu)$ is the emitted photon flux density. [1] When conducting an experiment, the emission spectral density S($\lambda$) is the measured quantity, so Eq. 2.2 should be modified by the relationship of the emission spectral density (units of power per wavelength interval, d$\lambda$) to the photon flux density (units of number of photons per time per frequency interval, d$\nu$), $d\nu/d\lambda = c/\lambda^2$ [24],

$$S(\lambda) = \frac{hc}{\lambda}\Phi(\lambda) = \frac{hc}{\lambda}\Phi(\nu)\frac{d\nu}{d\lambda}. \tag{2.3}$$

When combining Eqns.2.2, 2.3 the result is,

$$h\nu_f = \frac{\int h\nu\Phi(\nu)d\nu}{\int \Phi(\nu)d\nu} = \frac{\int \frac{hc}{\lambda}\frac{\lambda}{hc}S(\lambda)\frac{d\lambda}{d\nu}d\nu}{\int \frac{\lambda}{hc}S(\lambda)\frac{d\lambda}{d\nu}d\nu} = hc\frac{\int S(\lambda)d\lambda}{\int \lambda S(\lambda)d\lambda} = \frac{hc}{\lambda_f}. \tag{2.4}$$

Rearranging gives,

$$\lambda_f = \frac{\int \lambda S(\lambda)d\lambda}{\int S(\lambda)d\lambda}. \tag{2.5}$$

Eq. 2.1 shows that increasing the pump wavelength increases cooling efficiency. In reality, there is a practical limit for detuning the pump that is determined by

[1] Initially it was assumed that S($\nu$) should instead be integrated instead of $\Phi(\nu)$ in Eq. 2.2, but this was found incorrect, although the error is negligible ($\sim 0.5nm$) [22, 23]. The correct expression is given in the text.

two quantities that were omitted from the ideal scenario: (1) the external quantum efficiency to account for the fact that non-radiative processes are present, and not all of the radiated light exits the host material. and (2) the parasitic background absorption was neglected which is caused by small amounts of impurities which absorb radiation and return that energy back into the host as a form of heat.

To account for the change in the external quantum efficiency, consider a simple four-level system. Fig. 2.2 shows the levels in which the ground-state manifold con-

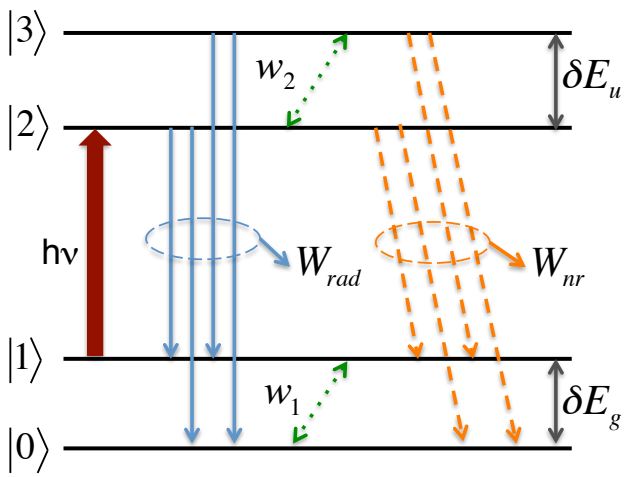


Figure 2.2: The four-level energy model for optical refrigeration consisting of two pairs of closely spaced levels, $|0\rangle$ and $|1\rangle$ in the ground state and $|2\rangle$ and $|3\rangle$ in the excited-state manifolds..

sists of two closely spaced levels of $|0\rangle$ and $|1\rangle$ with an energy separation of $\delta E_g$ and the excited manifold also consists of two states $|2\rangle$ and $|3\rangle$ with an energy separation $\delta E_u$. Laser excitation at $h\nu$ is tuned to be in resonance with the minimum transition from the ground state manifold to the excited state manifold, i.e. the $|1\rangle - |2\rangle$ transition, as shown by the bold red arrow. The blue arrows depict the spontaneous emission transitions from the upper level to the ground states with a rate of $W_{rad}$ which is assumed to be the same for all four transitions. The the orange dotted lines indicating non-radiative decay rates, also assumed to be equal, are given by

$W_{nr}$. The population in each manifold reaches a quasi-thermal equilibrium via an electronphonon interaction rate given by $w_1$ for lower states and $w_2$ for upper states.

The rate equations governing the density populations $N_0$, $N_1$, $N_2$, and $N_3$ are [24]:

$$\frac{dN_1}{dt} = -\sigma_{12}\left(N_1 - \frac{g_1}{g_2}N_2\right)\frac{I}{h\nu} + \frac{R}{2}(N_2+N_3) - w_1\left(N_1 - \frac{g_1}{g_0}N_0 e^{-\delta E_g/k_B T}\right), \quad (2.6)$$

$$\frac{dN_2}{dt} = \sigma_{12}\left(N_1 - \frac{g_1}{g_2}N_2\right)\frac{I}{h\nu} - RN_2 + w_2\left(N_3 - \frac{g_3}{g_2}N_2 e^{-\delta E_u/k_B T}\right), \quad (2.7)$$

$$\frac{dN_3}{dt} = -RN_3 - w_2\left(N_3 - \frac{g_3}{g_2}N_2 e^{-\delta E_u/k_B T}\right), \quad (2.8)$$

$$N_t = N_0 + N_1 + N_2 + N_3, \quad (2.9)$$

where $R = 2W_{rad} + 2W_{nr}$ is the total upper state decay rate, $\sigma_{12}$ is the absorption cross-section associated with the $|1\rangle$-$|2\rangle$ transition, $I$ is the incident laser irradiance, and the $g_i$ terms represent degeneracy factors for each level. The weighting factor in the electron-phonon interaction terms ($w_1$ and $w_2$) maintains the Boltzmann distribution among each manifold at quasi-equilibrium. The net power density deposited in the system is the difference between the absorbed and the radiated contributions:

$$P_{net} = \sigma_{12}N_1 I - \frac{g_1 N_2}{g_2 N_1}I - W_{rad}[N_2(E_{21}+E_{20}) + N_3(E_{31}+E_{30})] + \alpha_b I, \quad (2.10)$$

where the first term is the laser excitation ($|1\rangle$-$|2\rangle$ transition) and the second term includes the spontaneous emission terms from levels $|2\rangle$ and $|3\rangle$ with their respective photon energies. Also included is a term that represents the parasitic absorption of the pump laser with an absorption coefficient of $\alpha_b$. It is straightforward to

evaluate the steady-state solution to the above rate equations by setting the time derivatives to zero, i.e $\frac{dN_1}{dt} = \frac{dN_2}{dt} = \frac{dN_3}{dt} = 0$. To emphasize certain features, we ignore saturation and assume a degeneracy of unity for all levels. The net power density is then obtained as:

$$\mathbf{P}_{net} = \alpha_b I + \alpha_r I \left[1 - \frac{h\nu_f}{h\nu}\left(\frac{\eta_e W_r}{\eta_e W r + W_{nr}}\right)\right]. \tag{2.11}$$

The term in the parentheses is defined as the external quantum efficiency,

$$\eta_{ext} = \frac{\eta_e W_r}{\eta_e W_r + W_{nr}}, \tag{2.12}$$

which accounts for the non-radiative recombination $W_{nr}$ and extraction efficiency $\eta_e$ neglected earlier. Rare-earth doped solids typically have very high extraction efficiency due to low index of refraction which simplifies the external quantum efficiency to simple a function of the ratio of non-radiative to radiative recombination rates:

$$\eta_{ext} = \frac{1}{1 + W_{nr}/W_r}. \tag{2.13}$$

The mean fluorescence energy h$\nu_f$ is given by:

$$h\nu_f = h\nu + \frac{\delta E_g}{2} + \frac{\delta E_u}{1 + (1 + R/w_2)e^{\delta E_u/k_B T}}, \tag{2.14}$$

and the ground state resonant absorption $\alpha_r$ is:

$$\alpha_r = \sigma_{12} N_t \left(1 + e^{\delta E_g/k_B T}\right)^{-1}, \tag{2.15}$$

Even though the four level model is simple, it highlights important features of solid-state optical refrigeration that should be addressed. First, Eq. 2.14 shows that the mean fluorescence photon energy is redshifted at low temperatures, reducing the cooling efficiency. This shift is amplified if the upper state recombination rate ($R$) is faster than the electron-phonon interaction rate ($w_2$). This means that if $w_2 < R$, the excited state can decay before thermalization with the lattice, in which case energy

cannot be extracted from the crystal, i.e. no fluorescence upconversion, and no cooling. Rare-earth doped solids typically have long upper state lifetimes resulting in adequate thermalization times. Second, Eq. 2.15 shows diminishing pump absorption due to thermal depletion of the top ground state (i.e. $|1\rangle$) at low temperatures, $k_B T < \delta E_g$. Therefore the width of the ground-state manifold ($\delta E_g$), which in rare-earth doped systems is host dependent through crystal field splitting, must be narrow to achieve cooling at low temperatures with reasonable efficiency. The physics of this situation is very different for semiconductors which instead follow the Fermi-Dirac distribution and hence indistinguishable electrons populate the top of the valence band regardless of temperature and are available for excitation.

The next step is to consider the effect of an external pump source. Incident laser power, $P_0$, is attenuated through the sample such that the absorbed power is $P^i_{abs} = P_0(\alpha_i/\alpha_{total})[1 - e^{-\alpha_{total}L}]$, where $i = r, b$ for resonant and background absorption, $\alpha_{total}$ accounts for all of the absorption processes, and L is the length of the sample. Inserting this into Eq. 2.11 for the background and resonant absorbed powers the net power contributing to cooling is recovered,

$$P_{net} = P_0(1 - e^{-\alpha L}) \left[ \frac{\alpha_b + \alpha_r(\nu) - \alpha_r(\nu)\eta_{ext}\frac{h\nu_f}{h\nu}}{\alpha_r(\nu) + \alpha_b} \right] = P_{abs}\eta_{cool}. \tag{2.16}$$

The term preceding the brackets is the total absorbed power, $P_{abs} = P_0(1 - e^{-\alpha L})$, where $\alpha = \alpha_r(\lambda) + \alpha_b$ is the total absorption. The term inside the brackets is the cooling efficiency, $\eta_c$. This term can be simplified,

$$\eta_{cool} = \left[ \frac{\alpha_b + \alpha_r(\nu) - \alpha_r(\nu)\eta_{ext}\frac{h\nu_f}{h\nu}}{\alpha_r(\nu) + \alpha_b} \right] = \left[ 1 - \eta_{ext}\frac{h\nu_f}{h\nu}\left( \frac{\alpha_r(\nu)}{\alpha_r(\nu) + \alpha_b} \right) \right], \tag{2.17}$$

where again the term in parentheses is defined, this time as the absorption efficiency,

$$\eta_{abs} = \left( \frac{\alpha_r(\nu)}{\alpha_r(\nu) + \alpha_b} \right). \tag{2.18}$$

We can now define the full form for the cooling efficiency Eq. 2.17 in its compact form taking into account the small shift in the mean fluorescence associated with reabsorption ($\nu_f \rightarrow \tilde{\nu}_f$) and the temperature dependence [16, 23, 25, 26, 27],

$$\eta_c(\nu, T) = 1 - \eta_{ext}\eta_{abs}(\nu, T)\frac{h\tilde{\nu}_f(T)}{h\nu}, \tag{2.19}$$

accounting for each photon which extracts energy from the crystal lattice[2]. Eq. 2.19 is defined where negative values of the cooling efficiency denote cooling.

From here it is useful to look at a few limits in the cooling efficiency to discover the physics that it predicts. The first thing to notice is that if the limit is taken where $\alpha_b = 0$ and $\eta_{ext} = 1$, the ideal cooling efficiency Eq. 2.1 is recovered. It should be clear that the parasitic heating caused by background absorption is intentionally reduced as much as possible. When pumping near $\lambda \approx \tilde{\lambda}_f$, $\alpha_b \ll \alpha_r(\lambda)$, simplifying the absorption efficiency, $\eta_{abs} \rightarrow 1$. Therefore the cooling efficiency is linear around the mean fluorescence and a measurement of the external quantum efficiency can be made from where this linear relationship crosses zero,

$$\eta_{ext} = \frac{\tilde{\lambda}_f}{\lambda_{cross}}, \tag{2.20}$$

defining $\lambda_{cross}$ as the zero crossing wavelength, where the sample crosses over from heating to cooling. Both $\eta_{ext}$ and $\alpha_b$ are independent of wavelength. Therefore, by extending the pump wavelength to those longer than $\tilde{\lambda}_f$, resonant absorption decreases, as does $\eta_{abs}$. Eventually, heating must reoccur for a finite background absorption, and this second zero crossing provides a measurement of $\alpha_b$ by fitting the full form of the cooling efficiency (Eq. 2.19) with the value of $\eta_{ext}$ determined from Eq. 2.20.

It is useful to illustrate an example to understand what the product $\eta_{ext}\eta_{abs}$ must be to realize cooling. Requiring the cooling efficiency $\eta_c < 0$, and considering

[2]Throughout this thesis the form of Eq. 2.19 will be used where negative values of $\eta_c$ denote cooling. In other publications [16, 23, 25], both this form and its negative can be found defined as the cooling efficiency.

detuning the pump by $k_BT$, where $k_B = 1.38 \times 10^{-23}$J/K is the Boltzmann constant at temperature T, the product is found [26, 27]:

$$\eta_{ext}\eta_{abs} > 1 - \frac{k_BT}{h\nu_f}. \tag{2.21}$$

Taking the specific case for $Yb^{3+}$ at 300K which has a mean fluorescence $\lambda_f \approx 1\mu$m corresponding to energy $h\nu_f$ ≈1.24eV, the product $\eta_{ext}\eta_{abs}$ >98%. If the temperature is reduced to 100K, the product must increase to $\eta_{ext}\eta_{abs}$ >99% for cooling to be possible.

When a heat load is applied, temperature changes as

$$C(T)\frac{dT}{dt} = -P_{cool} + P_{load}. \tag{2.22}$$

where C(T)= $\rho c_v(T)V_s$ is the heat capacity given density $\rho$, temperature-dependent specific heat $c_v(T)$ from Debye theory, the sample volume $V_s$ and $P_{load}$ is the heat load. Bringing the sample to equilibrium means the cooling power must equal the heat load power, $P_{cool}$ =$P_{load}$. There are three sources of heat load, convective, conductive and radiative. Including these sources for a chamber with temperature, $T_c$, and sample at temperature, T, expands Eq. 2.22 into,

$$C(T)\frac{dT}{dt} = \eta_c P_{abs} + A_s\kappa_h(T_c - T_s) + \frac{N\kappa_L(T)A_L}{d_L}(T_c - T_s) + \frac{\varepsilon_s A_s \sigma}{1+\chi}(T_c^4 - T_s^4). \tag{2.23}$$

The first term to the right of the equal sign for $\eta_c < 0$ is the cooling power derived in Eq. 2.16. The second term is the convective heat characterized by the sample area $A_s$ and convective heat transfer coefficient $\kappa_h$. The third term is the conductive heat load where N is the number of contacting points with area $A_L$, length $d_L$ and conductivity $\kappa_L$. The final term is the black-body radiation heat load including the Stefan-Boltzmann constant $\sigma = 5.67 \times 10^{-8}$W/m$^2$/K$^4$. The subscripts $s, c$ denote the sample and chamber respectively with thermal emissivity $\varepsilon$ and area A, and,

$$\chi = (1 - \varepsilon_c)\frac{\varepsilon_s A_s}{\varepsilon_c A_c}. \tag{2.24}$$

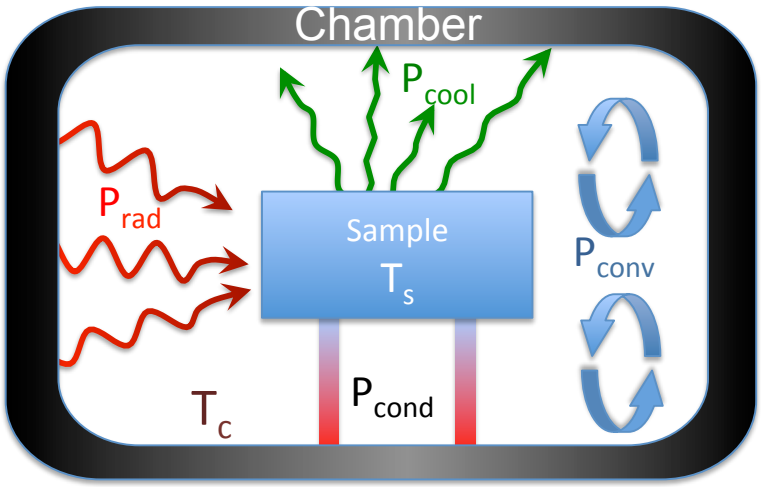


Figure 2.3: The model depicts the three sources of heat load, convective in blue ($P_{conv}$), conductive with a gradient from red to blue ($P_{cond}$) and radiative in red ($P_{rad}$). The sample sits in the middle with emissivity $\varepsilon_s$, area $A_s$ and temperature $T_s$. The chamber has the same parameters as the sample. $P_{cool}$ is shown in green.

Experimentally, it is necessary to understand the source and relative magnitude of each heat load source to minimize $P_{load}$ and maximize the temperature difference between the sample and chamber as discussed in Ch. 4.

Considering Eq. 2.23 where the radiative load assumes small temperature changes so that the radiative term, $P_{rad}$, can be approximated as [28],

$$P_{rad} = \left(\frac{1}{1+\chi}\right) 4\varepsilon_s \sigma A T_c^3 \Delta T, \tag{2.25}$$

it becomes possible to simplify the temperature dynamics. Under steady state conditions in Eq. 2.22, ($\frac{dT}{dt} = 0$), the cooling power equals the heat load, where the heat load is the sum of the three sources mentioned above. Therefore

$$\eta_c P_{abs} \approx (C_{rad} + C_{cond} + C_{conv})\Delta T \approx K\Delta T. \tag{2.26}$$

where $C_{rad}, C_{cond}, C_{conv}$ are the constants associated with each of the respective heat

sources and combined into a heat load parameter K. Rewriting,

$$\Delta T \approx \frac{\eta_c P_{abs}}{K}. \tag{2.27}$$

This means the largest temperature deviation the crystal can obtain from its surroundings depends on increasing the cooling efficiency, increasing absorbed power, and decreasing the heat load.

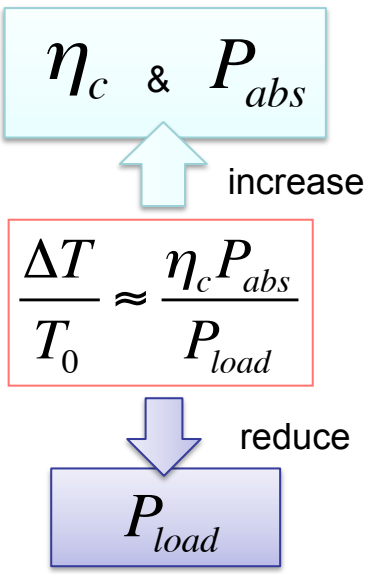


Figure 2.4: Obtaining the largest ΔT between a crystal and its surroundings requires maximizing $\eta_c$ and $P_{abs}$ while minimizing $P_{load}$.

# Chapter 3

# Empirical cooling efficiency model

## 3.1 Introduction

Until recently, the most investigated and best performing material system in optical refrigeration was Yb-doped ZBLAN. As mentioned in the Ch. 1, the purity necessary for ZBLAN in the telecommunications industry allowed for the first observation of net cooling. Since then there has been investigation of other hosts and ternary rare-earth (RE) ions as cited in the Ch. 1 and summarized in Table 3.1. With so many combinations of RE ions and host materials, criteria are needed to narrow down the field into educated choices. ZBLAN was the ideal starting material because of purity, and Ytterbium is a good choice of cooling ion because of the available pump sources around 1030nm. Now that other materials are approaching the same purity levels along with development of pump sources further into the infra-red (IR), full characterization of different combinations can lead to clues as to what materials are optimal for optical refrigeration.

Utilizing optical refrigeration theory of Ch. 2, this chapter covers the characterization techniques necessary to obtain cooling performance expected for any RE-doped

| Optical refrigeration | | |
|---|---|---|
| RE ion | Glasses | Crystals |
| $Yb^{3+}$ | ZBLAN [8]<br>BIG* [30]<br>CNBZn* [30] | YAG [29]<br>$Y_2SiO_5$ [29]<br>$KPb_2Cl_5$* [12]<br>$KGd(WO_4)_2$* [11]<br>$BaY_2F_8$ [23]<br>$LiYf_4$ [31, 32, 33, 28, 34, 25] |
| $Tm^{3+}$ | ZBLAN [18] | $BaY_2F_8$ [23] |
| $Er^3+$ | CNBZn [20] | $KPb_2Cl_5$ [20] |

Table 3.1: Rare earth ions in hosts which have shown bulk cooling. Starred items showed local cooling as detected by photo-thermal deflection [23].

solid. In particular, record cooling results were characterized and obtained in 1%, 5%, 7% and 10% wt. Ytterbium doped Yttrium Lithium Fluoride ($Yb^{3+}$:YLF) crystals. Characterization of other combinations of RE ion and host entails analysis similar to the one presented in this chapter which can therefore act as a basis by which cooling performance . Discussion of benefits as well as possible areas of improvement, including discussion of the spectroscopic minimum achievable temperature (MAT), are presented.

Sec. 3.2 will discuss rare-earth ions and the importance of host material. Sec. 3.3 covers the four important components of cooling efficiency applied to the $Yb^{3+}$:YLF crystal, along with the associated experimental measurements. The methods presented in this section can be extended to other RE ion-host combinations. Sec. 3.4 compiles the results into a form which provides the complete spectroscopic picture of predicted cooling performance.

## 3.2 Rare-earth ions and host materials

So far the only mention of ions which produce cooling are rare-earth ions. These ions, made up of the Lanthanide series and Actinide series which are physically separated from the other elements on the periodic table, Fig. 3.1, are chemically advantageous

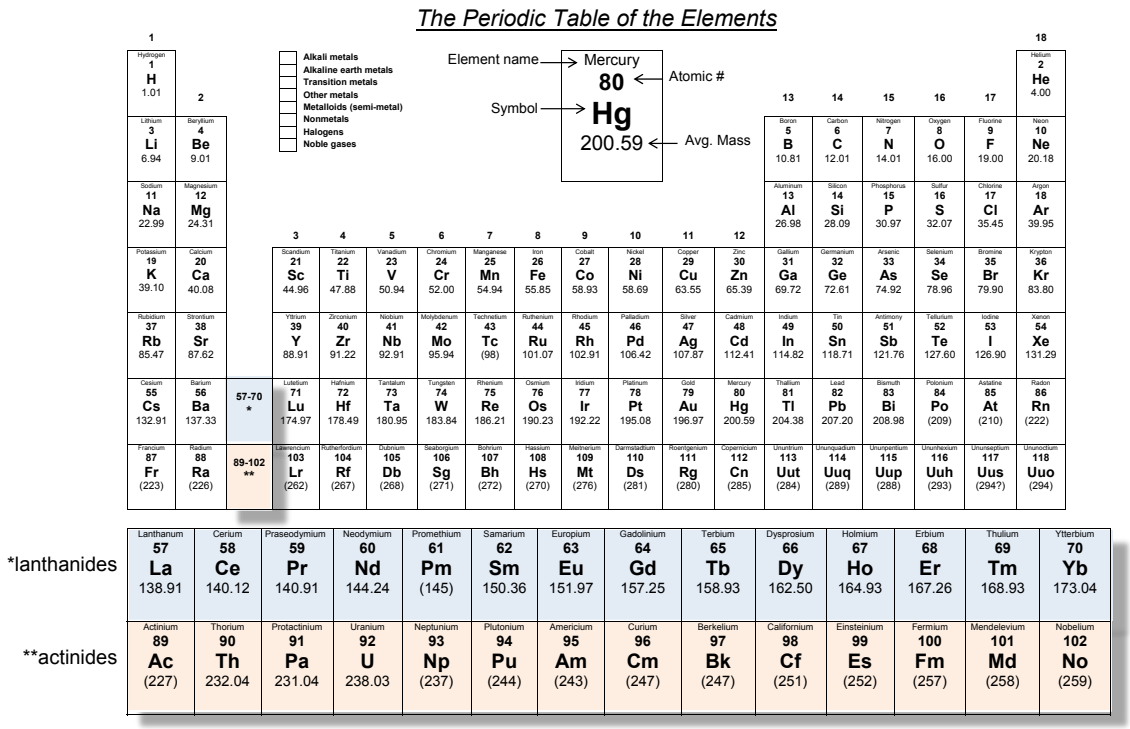


Figure 3.1: The periodic table of elements highlighting the rare earths.

for cooling. The Lanthanide series with atomic numbers between 58-71, are composed of a Xenon structure for the inner shells, a partially filled 4f state, a filled 6s state and on occasion an electron in the $5d^1$ state (a filled 6s shell implies the 5s and 5p shells are also filled without being explicitly stated in the notation).

When lanthanides form a ternary ionic bond, the three highest energy electrons are used. Therefore the two $6s^2$ electrons with one electron from the $5d^1$ or 4f shell form a bond with neighboring atoms, often Fluorine (F) or Oxygen (O) atoms, and

the $RE^{3+}$ ion is created. As a particular example, the un-ionized Ytterbium atom has filled outer shells $4f^{14}$ and $6s^2$. When bonding to three Fluorine atoms, the Ytterbium atom gives up two $6s^2$ and one of the $4f^{14}$ electrons, leaving a single unoccupied electronic state in the 4f shell. This creates the single optical transition found for glasses and crystals doped with $Yb^{3+}$. Indeed, the optical transitions in all of the rare-earths are the electronic transitions in the 4f shell since those are donated first to form ionic bonds. This creates a unique advantage for cooling and the reason RE ions are used. Fig. 3.2 shows cartoonish orbital shells (left) highlighting the spatially larger 5s and 6s electron shells while the energy as a function of orbital radius (right) shows the 4f electrons with higher energy. Spatially, the 4f electrons are

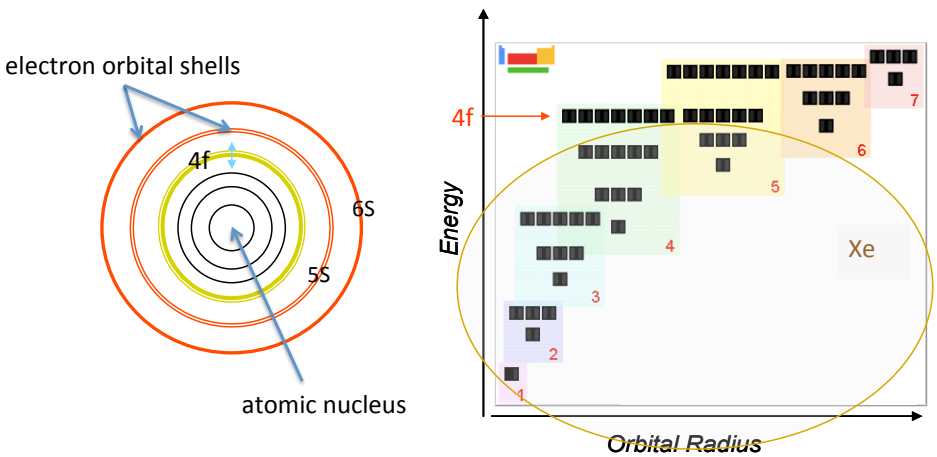


Figure 3.2: (left) Cartoonish electronic orbital shells highlighting the larger orbital shell radius of the lower energy 5s and 6s electrons compared with the 4f electrons. (right) Electronic energy versus orbital radius.

shielded from neighboring electrons by the larger and spherically symmetric filled 5s and 5p shells which do not significantly affect the 4f electrons. This shielding reduces the strength of the vibronic sidebands, sharpens the homogeneous lines (leading to larger absorption coefficients as will become apparent in Ch. 3), and suppress multi-phonon non-radiative relaxation [22]. The 4f optical transitions in the Lanthanide series, shielded by the outer shells, are not typical of what is seen in atomic spectra

with sharp absorption lines, but account for the "atomic-like" behavior with narrow, separated bands leading to sharp absorption peaks corresponding to the Stark splitting.[1].

With the knowledge that RE ions are best for cooling, which rare-earth is the best candidate? Eq. 2.1 shows that for a given separation of between the excitation energy and the mean fluorescence energy, cooling efficiency is increased by choosing a RE ion with lower transition energy. Fig. 3.3 shows the behavior of the cooling efficiency considering a separation of $2.5k_BT$ with the grey line. With Yb having the second largest transition, the comparative cooling efficiency is second worst when considering the first excited state. Additionally, any pump photon of higher energy that recombined non-radiatively or was absorbed in an impurity would give rise to greater heating. For instance Ytterbium requires twice the energy as Thulium.

Of course, there are other considerations in favor of Ytterbium. Mentioned in Ch. 1, high power (>10W continuous wave, CW) pump sources are more readily available for the 1$\mu$m transition for Yb since there are several Yb doped laser crystals which naturally generate stimulated emission from ∼1005nm-1060nm (Yb:YAG, $Yb^{3+}$:YLF, Yb:KGW, Yb:KYW, etc.) and more difficult to obtain for the the other rare earths requiring longer wavelengths, though sources are becoming more readily available. With more availability of pump sources, absorbed power is increased which in turns increases cooling power. Additionally, Yb can be utilized in a wider variety of hosts with higher phonon energies.

When considering which RE ion is best for cooling, host phonon energy must be considered. Fluoride crystals, including YLF, have low phonon energy. The external

[1]Discussion is limited to the Lanthanide series, because optical properties for elements in the Actinide series have not been studied, other than Uranium, and most of the elements are radioactive.

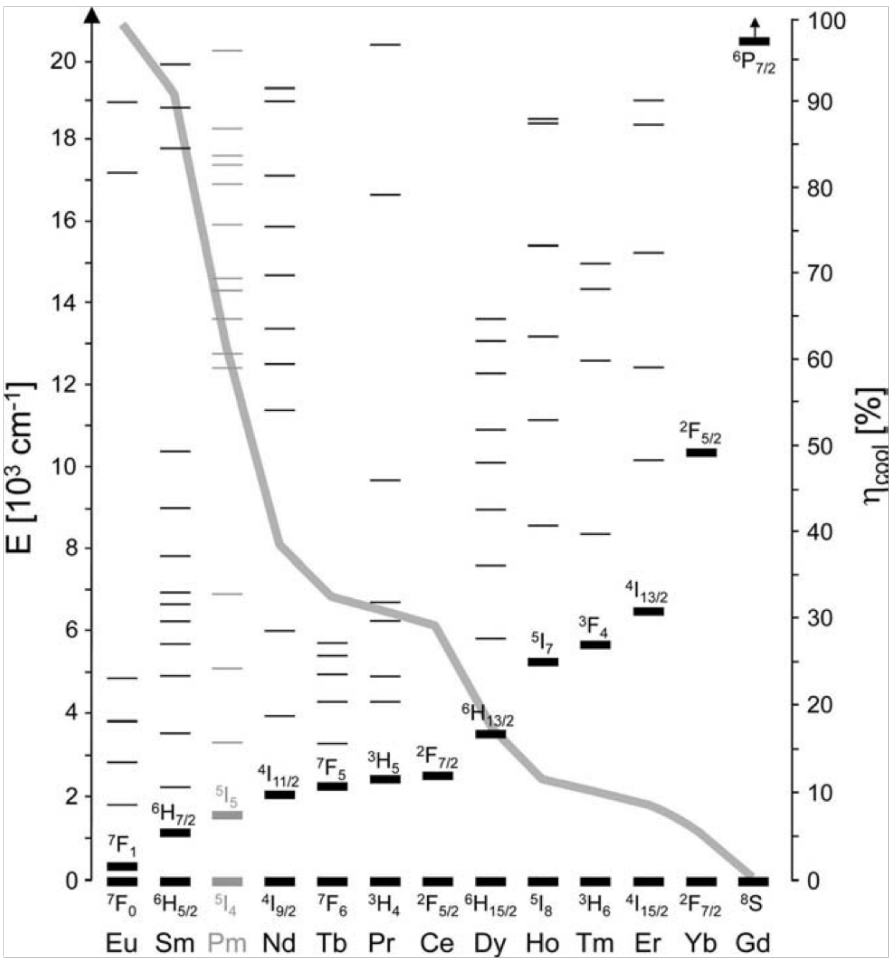


Figure 3.3: This figure is used from the second chapter of the book "Optical Refrigeration" [24]. The left axis shows the energy levels of the 4f transition levels of trivalent RE ions. The ions are ordered with increasing energy of the first excited state (emboldened). The grey line gives the ideal cooling efficiency with value given by the right axis for an energy separation, $h\bar{\nu}_f - h\nu = 2.5\text{kT}$ at 300K.

quantum efficiency, re-written here,

$$\eta_{ext} = \frac{\eta_e W_r}{\eta_e W_r + W_{nr}}, \tag{3.1}$$

is made up of the extraction efficiency $\eta_e$, the radiative recombination rate $W_r$, and the non-radiative recombination rate $W_{nr}$. High external quantum efficiency is desired, so considering the case of multi-phonon relaxation for the non-radiative

recombination rate places a strong dependence on a host with low phonon energy so that $W_{nr} \ll W_r$. The rate $W_{nr}$ depends on the number, m, of phonons that are created during relaxation, m=$\Delta E/\hbar\omega$, where $\Delta E$ is the pump energy from the ground state to the first excited state and $\hbar\omega$ is the energy of the accepting phonon mode. This means m is proportional to the energy gap, $\Delta E$, of the RE ion. Then the rate is described by the energy gap law [35],

$$W_{nr} = \beta e^{-\alpha \Delta E}, \tag{3.2}$$

where $\beta$ and $\alpha$ are strongly dependent on the host material with $\alpha$ proportional to the phonon energy. Fig. 3.4 shows a comparison of RE ions with associated host materials making the assumption that an acceptable quantum efficiency is >90% and a typical relaxation rate is $W_r \sim 10^{-2}$s, where the maximum phonon energy $\hbar\omega_{max} = \Delta E/8$.

YLF has a phonon energy low enough to be used with $Yb^{3+}$, $Er^{3+}$, $Tm^{3+}$, and $Ho^{3+}$ and has given impressive cooling performance with $Yb^{3+}$, so it is worthwhile studying these other RE ions in YLF to get a formal comparison.

Yttrium Lithium Fluoride (YLF) is an appealing host for optical refrigeration for a number of reasons. One advantage in particular arises from the high doping concentrations available by having only a few constituents ($YF_3$, LiF and $YbF_3$, as compared to ZBLAN glass with $YbF_3$:$ZrF_4$-$BaF_2$-$LaF_3$-$AlF_3$-NaF). The Ytterbium (Yb) electron structure is [Xe] $4f^{14}6s^2$ in the ground state. The lanthanides are chemically similar to Yttrium (Y) ([Kr]$4d^15s^2$) and Lanthanum (La) ([Xe]$5d^16s^2$) and in crystal structures can substitutionally replace Y and La in the crystal lattice. For example, when doping Yttrium Lithium Fluoride ($LiYF_4$) with Ytterbium, the Yttrium is substituted by Ytterbium in the chemical structure, allowing for very high doping concentrations, and in principle, Ytterbium can completely replaced Yttrium. Unlike a crystal, amorphous glass hosts "freeze" the constituents in place and therefore do not perform these substitutions. Therefore when considering the

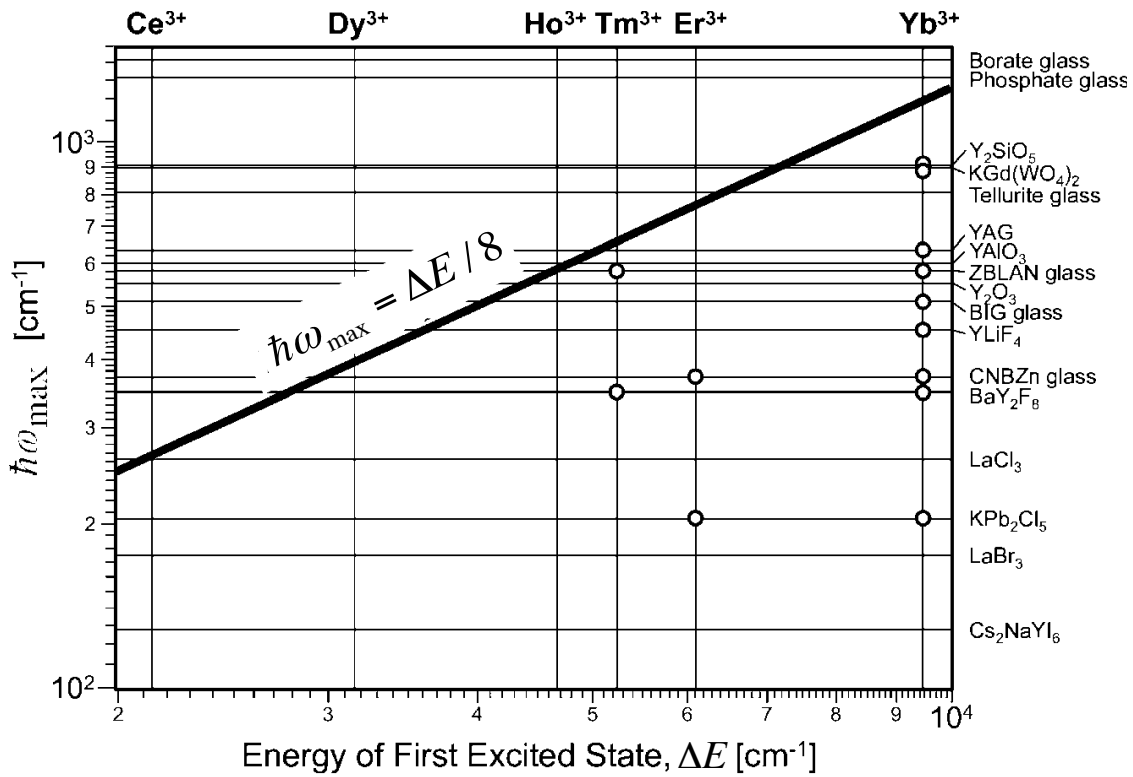


Figure 3.4: This figure shows the phonon energies for different host materials along with the energy gap of the first excited state for six RE ions, helping to illustrate which candidate host and ion combinations have low non-radiative relaxation rates considering a multi-phonon process [24].

full composition, high doping (>3% wt.) in glasses makes them chemically unstable. Also, when creating ZBLAN, several components are necessary for a stable mix ($ZrF_4$-$BaF_2$-$LaF_3$-$AlF_3$-NaF), so adding high concentrations of another component destabilizes the mix. An important second advantage of crystals over amorphous glass hosts is the low inhomogeneous broadening associated with strong crystal field splitting maintaining the sharp resonances in the Stark manifolds which strongly increase resonant absorption. The combination of increased doping along with low inhomogeneous broadening greatly enhance resonant absorption.

Additional advantages for YLF are high thermal conductivity, non-hygroscopic,

good mechanical hardness, and low phonon energy. Features such as high thermal conductivity, good mechanical hardness, and being non-hygroscopic are useful for the practicality of forming an all solid state optical cryocooler. High thermal conductivity leads to improved heat extraction from an externally applied load. Good mechanical hardness lends benefits to surface preparation which helps prevent surface inclusions from generating unwanted heat. And being non-hygroscopic means it is not plagued by unwanted $OH^-$ bonds which reduce quantum efficiency.

With some understanding of RE ion and host properties, $Yb^{3+}$:YLF was chosen to perform optical refrigeration. The next step is to characterize the cooling performance of the crystals.

## 3.3 The cooling efficiency of $Yb^{3+}$:YLF

In order to characterize the cooling performance of $Yb^{3+}$:YLF, it is first necessary to understand the properties of the cooling efficiency that need to be measured. As mentioned in Ch. 2, there is an inherent temperature dependence associated with the cooling efficiency. The electron distribution in each of the $Yb^{3+}$ manifolds, under local thermal equilibrium, is determined by a Boltzmann distribution $N(E) \propto N_0 e^{-E/k_B T}$ [36]. The temperature dependence of this distribution means the spectroscopic components, specifically the absorption and emission, of the cooling efficiency are temperature dependent. Rewriting Eq. 2.16 and Eq. 2.17 with the explicit temperature dependence for a single pass through the crystal gives,

$$P_{cool} = P_0(1 - e^{-\alpha(\lambda,T)L}) \left[1 - \eta_{ext} \frac{\lambda}{\lambda_f(T)} \left(\frac{\alpha_r(\lambda,T)}{\alpha_r(\lambda,T) + \alpha_b}\right)\right]. \tag{3.3}$$

A multi pass setup substitutes $L$ for the effective path length $NL$, where $N$ is the number of passes through the crystal. The cooling efficiency (the term in square brackets) has four quantities that need to be measured in order to characterize the

cooling performance of each $Yb^{3+}$:YLF crystal: the mean fluorescence wavelength $\lambda_f(T)$, the resonant absorption $\alpha_r(\lambda, T)$, the background absorption $\alpha_b$ and the external quantum efficiency $\eta_{ext}$. This study is performed under the assumption that the temperature dependence in the background absorption $\alpha_b$ and the external quantum efficiency $\eta_{ext}$ is negligible [23] [24]. Samples tested include several 5%, one 7.5% and one 30% wt.$Yb^{3+}$:YLF crystals grown by the Czochralski technique at the University of Pisa, Italy. Additional samples from AC Materials, Inc. in Tarpon Springs, FL, were grown to perform a doping study of undoped YLF, 1%, 5%, 7% and 10% wt. $Yb^{3+}$:YLF crystals as well as trace elemental analysis to find impurities described in Ch. 6.

### 3.3.1 Temperature dependent mean fluorescence wavelength

Measurement of the temperature dependent mean fluorescent wavelength is performed in a carefully controlled experiment. YLF is birefringent so there are two different polarizations, E$\|$c and E$\perp$c, that need to be measured. Measurement of both E$\|$c and E$\perp$c is needed for the determination of the resonant absorption, while the average gives $\lambda_f(T)$. Since fluorescence can be reabsorbed in the crystal, in order to get an accurate measurement of mean fluorescence, care should be taken to have a known and consistent reabsorption depth consistent with the power cooling experiments which are presented in Ch. 4. Additionally, a minimal reabsorption depth should be used when measuring the fluorescence used in calculating the resonant absorption in Sec. 3.3.2.

Fig. 3.5 shows a diagram of the fluorescence measurement experiment. The crystal is clamped and thermally linked to a copper cold-finger inside a cryostat, using Indium foil to ensure very good thermal contact, and oriented such that a polarizer can be placed between the crystal and collection optics to measure both E$\|$c and

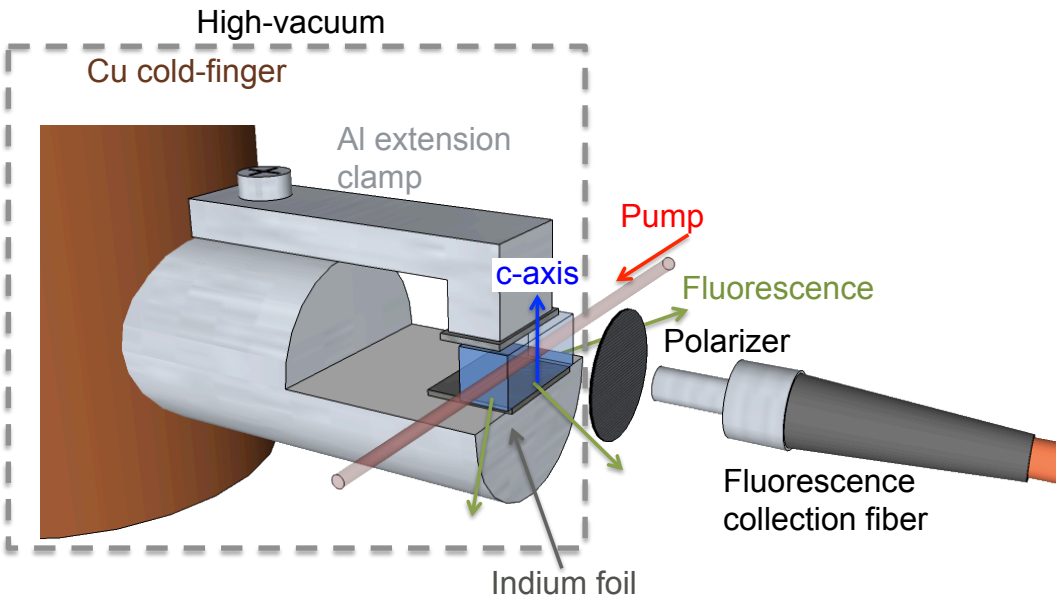


Figure 3.5: The copper (Cu) cold-finger with aluminum (Al) extension clamps the crystal with indium foil. After introducing high vacuum, the temperature is varied from 300K-30K. Fluorescence is collected through a 600$\mu$m fiber.

E$\perp$c, or removed for the combination. A high vacuum is pulled on the cryostat which is attached to a closed cycle helium refrigerator, and the cold-finger temperature controlled with a Proportional-Integral-Derivative (PID) controller and heater coil. A thermocouple is integrated with the PID controller, attached inside the cold-finger. A second thermocouple is used to independently monitor the clamp temperature. The cryostat has four windows to admit pump light through the cryostat and fluorescence collection. The crystal is placed close enough to one of the windows to collect fluorescence through a 600$\mu$m fiber in a radiometrically calibrated Ocean Optics (model HR4000) with sensitivity over the range of 200nm-1100nm. A laser tuned to a highly absorbing wavelength near the mean luminescent wavelength pumps the crystal. The wavelength is chosen such that it lies in a featureless region of the emission spectra near $\lambda_f$ to ensure that: (i) post-process removal does not alter the spectra, and (ii) so that it does not introduce significant heating. Spectra is col-

lected from 300K-30K in increments of 10K for both spectral orientations. With the

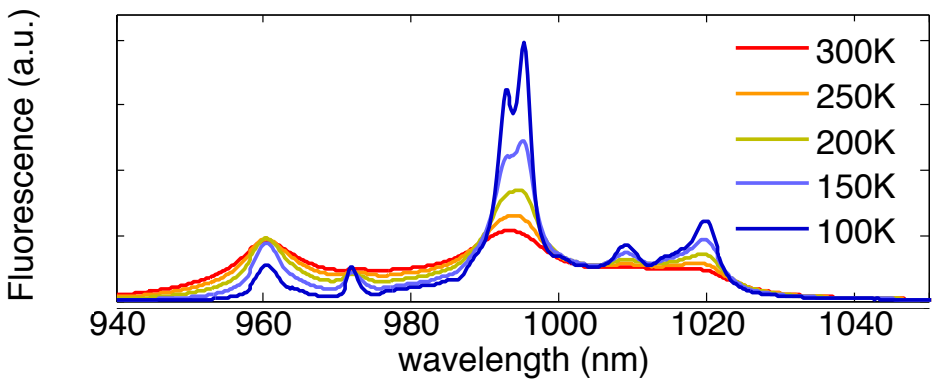


Figure 3.6: Fluorescence spectra of $Yb^{3+}$:YLF for E‖c.

spectra collected, the temperature dependent mean fluorescence wavelength can be measured using Eq. 2.5, rewritten here with the explicit temperature dependence,

$$\lambda_f(T) = \frac{\int \lambda S(\lambda, T))d\lambda}{\int S(\lambda, T)d\lambda}, \tag{3.4}$$

Fig. 3.7 shows the temperature dependence of $\lambda_f(T)$ measured from the unpolarized fluorescence spectra for the 5% wt $Yb^{3+}$:YLF samples.

### 3.3.2 Measuring $\alpha_r(\lambda, T)$

Anti-Stokes fluorescence relies on the absorption of photons red-shifted from the mean luminescence wavelength. In this region of the absorption spectra, known as the cooling tail, direct measurement is difficult to do directly, due to the exponential decrease in absorption. Traditionally absorption is measured using Fourier transform infrared (FTIR) spectrophotometer, but at low temperatures, the absorption drops to levels close to zero in the cooling tail, and cannot be measured directly by FTIR. Instead, calculating the absorption by measuring the emission is done using a reciprocal relationship between the absorption and emission cross-sections that was first

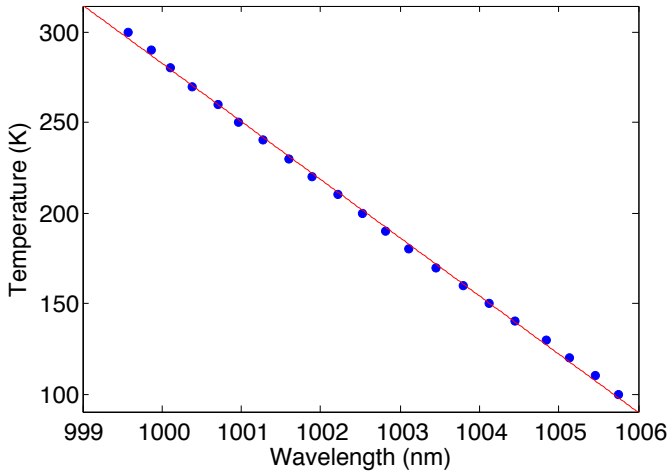


Figure 3.7: Temperature dependence of the mean fluorescence wavelength (blue) with a linear fit (red).

established by McCumber [37] (the term reciprocity is used to denote this reciprocal relationship).

Following the treatment provided by Verdeyen [36], assume a two manifold system, such as in Fig. 3.8, that assumes the populations of each manifold that thermalize quickly with respect to radiative decay (the local thermal equilibrium (LTE) model), and so are related by the Boltzmann factor. Integrating over the energy distributions in each manifold gives the stimulated emission, $\sigma_{em}$, and absorption, $\sigma_{abs}$, cross sections. The ratio of these cross sections is [36],

$$\frac{\sigma_{abs}(\nu)}{\sigma_{em}(\nu)} = \left[\frac{g_2/\Delta E_2}{g_1/\Delta E_1}\frac{Z_2(T)}{Z_1(T)}e^{(-E_0)/kT}\right]e^{(h\nu)/kT} = \frac{N_{2eq}}{N_{1eq}}e^{(h\nu)/kT} \tag{3.5}$$

where $g_{1,2}$ are the degeneracies, and $h\nu$ is the photon energy. $Z_{1,2}(T)$=1-exp[1-$e^{-\Delta E_{1,2}/kT}$ ] and is inversely proportional to $N^0_{1,2}$, the density per quantum level at the respective band edges. $N_{1eq,2eq}$ are the populations of each manifold at equilibrium. Defining an "excitation" potential, $\epsilon$, where $e^{-\epsilon/kT} = N_{2eq}/N_{1eq}$ allows Eq. 3.5 to be rewritten as,

$$\sigma_{abs}(\nu) = e^{(h\nu-\epsilon)/k_BT}\sigma_{em}(\nu), \tag{3.6}$$

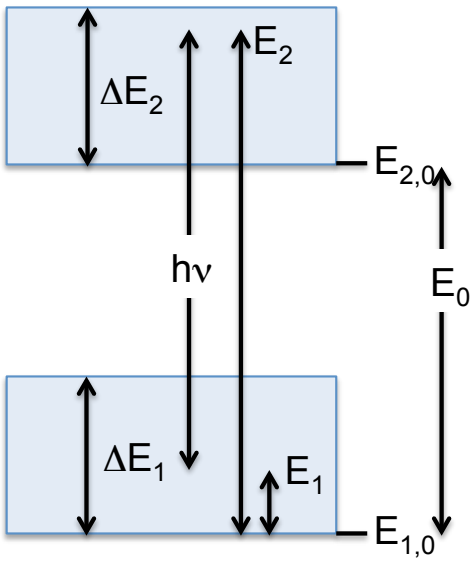


Figure 3.8: Example manifold diagram for the McCumber [37] relations.

where the relationship between absorption and stimulated emission has been obtained. Stimulated emission is then related to spontaneous emission by,

$$\sigma_{em}(\nu) = A_{21} g(\nu) \frac{\lambda_0^2}{8\pi n^2}, \tag{3.7}$$

where the $A_{21}$ Einstein A-coefficient, $g(\nu)$ is the lineshape function, $\lambda_0$ is the free-space wavelength and n is the index of refraction. Next, the absorption cross section is related to absorptivity, $\alpha(\nu)$ and population density $N_1$ by,

$$\sigma_{abs}(\nu) = \frac{\alpha(\nu)}{N_1}, \tag{3.8}$$

Absorptivity, $\alpha(\nu)$, is described by the Beer-Lambert Law [38] by the attenuation of light traveling through an medium of length L, with $I(z) = I_0 e^{-\alpha(\nu)L}$. To get to the ratio in Eq. 3.5, Eq. 3.7 is multiplied by $N_2$ giving,

$$N_2 \sigma_{em} = F_P(\nu) \frac{c^2}{\nu^2 n^2} \tag{3.9}$$

where $F_p(\nu)$ is the number of fluorescent photons emitted from a volume per element

frequency per element solid angle. Finally, absorptivity can be expressed as [39],

$$\alpha(\lambda, T) \propto \lambda^5 S(\lambda, T) e^{hc/\lambda k_B T}, \tag{3.10}$$

where $\alpha(\lambda, T)$ is the absorption coefficient at wavelength $\lambda$ and temperature T. $S(\lambda)$ is the measured spectral intensity at temperature $T$.

Using this relationship and the measured temperature dependent fluorescence spectra allows one to calculate the relative spectral dependence of the temperature dependent $\alpha(\lambda, T)$. Using the Beer-Lambert law allows for determination of the absolute value of $\alpha(\lambda, T)$ by measuring the absorber length along with input and output intensities at a wavelength and temperature where absorption is high enough to give accurate measurement via a power meter. Since the beginning of this section discussed the difficulty with directly measuring the absorption in the cooling tail, it is useful to see a comparison. Fig. 3.9 shows the direct comparison between the absorption spectra measured by a spectrophotometer and that calculated through reciprocity. Good agreement is shown for high absorption regions while the spec-

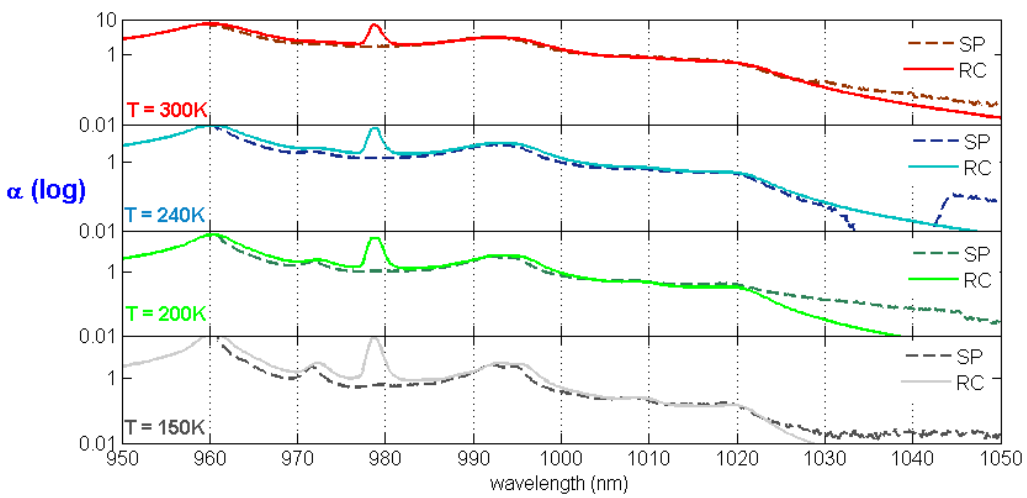


Figure 3.9: Comparison of reciprocity (RC) and spectrophotometer (SP) measurements. The excitation line at 978nm was not removed here for SC.

trophotometer measurements become unreliable beyond 1020nm, especially at low temperatures [16]. Because this is the particular region of interest, reciprocity is used to calculate absorption for each sample with direct absorption verification at various wavelengths via a power meter.

Temperature dependent absorption spectra determined from the emission spectra (Fig. 3.6) for E‖c using Eq. 3.10 is shown in Fig. 3.10. Two orders of magnitude

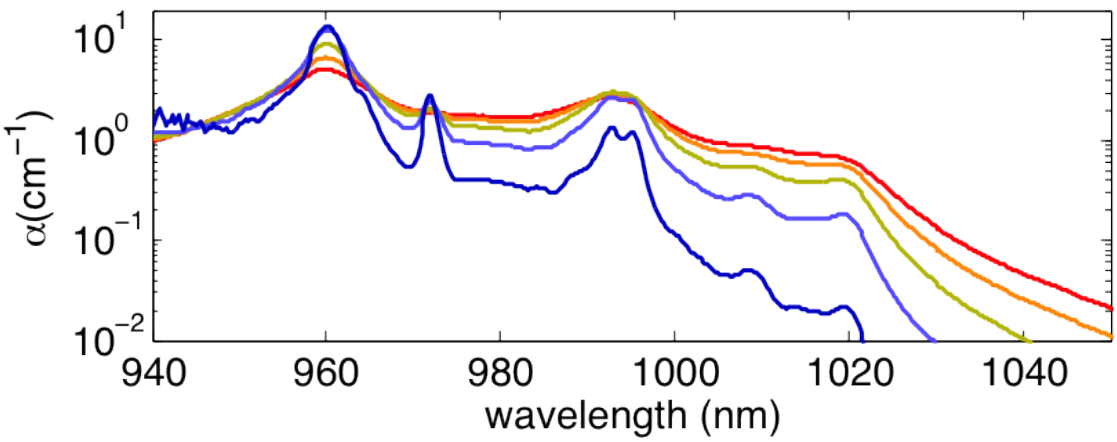


Figure 3.10: Temperature dependent absorption spectra for $Yb^{3+}$:YLF at E‖c, calculated from the temperature spectra in Fig. 3.6 with Eq. 3.10.

decrease or more in absorption is observed for wavelengths beyond 1020nm, and the rest of the cooling tail decreases by one and a half orders of magnitude. When considering the absorption efficiency, Eq. 2.18, even for an extremely small, constant background absorption, eventually $\alpha_r$ reduces enough that $\eta_{abs}$ cannot sustain cooling. This is a direct consequence of the temperature dependence in the resonant absorption, Eq. 2.15.

Now that the temperature dependent absorption spectra have been obtained, it is important to analyze the advantages supplied by a crystalline host, particularly in the cooling region of interest known as the "cooling tail". The "cooling tail" is the region in the absorption spectra for wavelengths longer than $\lambda_f$. For 300K,

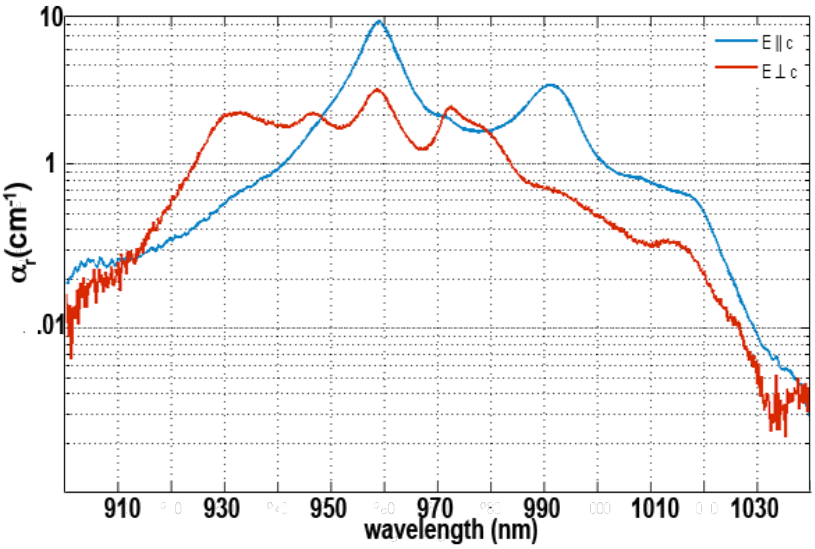


Figure 3.11: Resonant absorption for 5% $Yb^{3+}$:YLF for E∥c and E⊥c at 300K as obtained by a spectrophotometer.

the mean fluorescence is ∼1000nm according to Fig. 3.7. In order to achieve the greatest absorption efficiency for a constant background absorption, it is necessary to utilize the polarization with the maximum resonant absorption in the cooling tail. There are two polarizations for resonant absorption, $E \parallel c$ and $E \perp c$. Fig. 3.11 shows $\alpha_r(\lambda, 300K)$ for the two different polarizations. For wavelengths longer than ∼1000nm, E∥c is $\sim 2.5\times$ $E \perp c$, therefore it is advantageous to pump at this polarization. With this knowledge, samples are intentionally prepared such that pump light at $\pi$-polarization is coupled entirely into the crystal by cutting the faces of the crystal at Brewster angle relative to the pump polarization, with the crystal axis parallel to that polarization after accounting for the angular deflection caused by a change in index of refraction. An image of a brewster cut $Yb^{3+}$:YLF crystal can be seen in Fig. 3.12. compares Taking into account the maximum absorption relative to the crystal axis, we can now see the advantage of utilizing a crystal host. As temperatures decrease, the absorption peaks sharpen, thanks to the crystal field splitting,

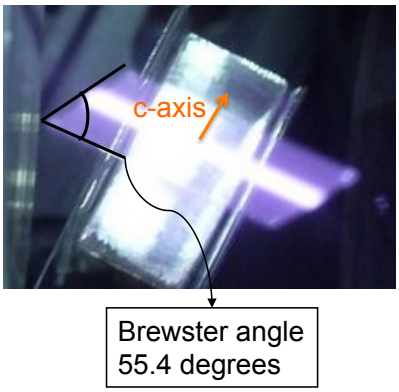


Figure 3.12: Brewster cut $Yb^{3+}$:YLF crystal. The white light through the center of the crystal is a false color image of the fluorescence as seen by a CCD camera which is propagating perpendicular to the c-axis as indicated with E‖c.

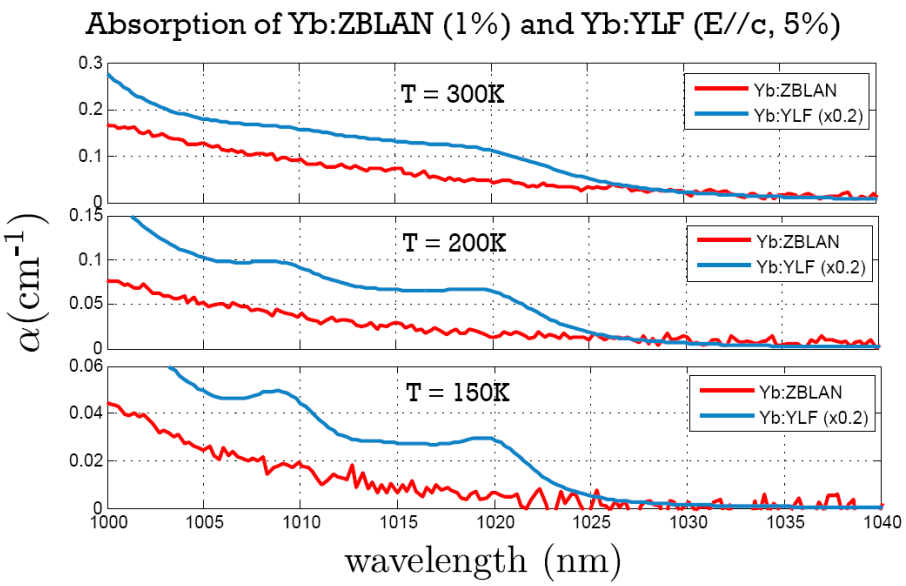


Figure 3.13: Absorption comparison between $Yb^{3+}$:ZBLAN and $Yb^{3+}$:YLF (normalized to 1% doping)

leading to high absorption in the cooling tail when compared to an amorphous glass host. Fig. 3.13 compares the absorption in the cooling tail absorption for $Yb^{3+}$:YLF and Yb:ZBLAN, normalized to a 1% doping concentration. Even after normalization, $Yb^{3+}$:YLF maintains higher absorption and clear absorption peaks, especially

as temperatures decrease. It is especially useful to note the absorption amplification at 1020 nm. In reality, the absorption is five times higher than the ZBLAN sample due to higher doping.

### 3.3.3 Measuring the external quantum efficiency and background absorption

Ch. 2 discussed a few of the limits associated with the cooling efficiency Eq. 2.19, noting that the relationship between cooling efficiency and wavelength should behave linearly around the mean luminescence wavelength and pumping at longer wavelengths should reveal the behavior of the background absorption. Assuming cooling occurs, measurement of $\eta_{ext}$ and $\alpha_b$ can be done by fitting the two zero crossing points, one near $\lambda_f$ and the other at longer wavelengths. The cooling efficiency given by Eq. 2.16 states $\eta_c = P_{net}/P_{abs}$, where the net power is proportional to the change in temperature. The absorbed power can be determined by taking the difference of incident power $P_0$ and transmitted power $P_{tr}$, but this method introduces significant error. Even though the sample is cut at Brewster's angle to minimize reflection R, tuning over the range of 970nm-1070nm requires accurate measurement of a change in absorption nearly three orders of magnitude. Instead, photo-luminescence excitation (PLE) spectroscopy [40] is used as a sensitive absorption measurement technique. The number of absorbed photons is proportional to the absorption cross section, the dopant density, the number of pump photons, and the absorber length. Therefore in steady state, assuming $\eta_{ext} = 1$, the number of emitted photons per second equals the number of absorbed photons. At a given pump wavelength, the magnitude depends on the efficiency of the collection optics and detector, etc. Therefore, integrating the fluorescence spectra is proportional to the absorbed power,

$$P_{abs} \propto \int S(\lambda) d\lambda. \tag{3.11}$$

Therefore,

$$\eta_c \propto \frac{\Delta T}{\int S(\lambda) d\lambda}. \tag{3.12}$$

Determination of $\eta_{ext}$ and $\alpha_b$ is done with the same experiment aptly named: Laser Induced Temperature Modulation Spectrum (or LITMoS) test. Since the colloquial definition of litmus is used to describe the general nature or behavior of an object, a LITMoS test in this case is used to characterize the cooling performance of crystals. A simple diagram of the experimental setup can be seen in Fig. 3.14. The

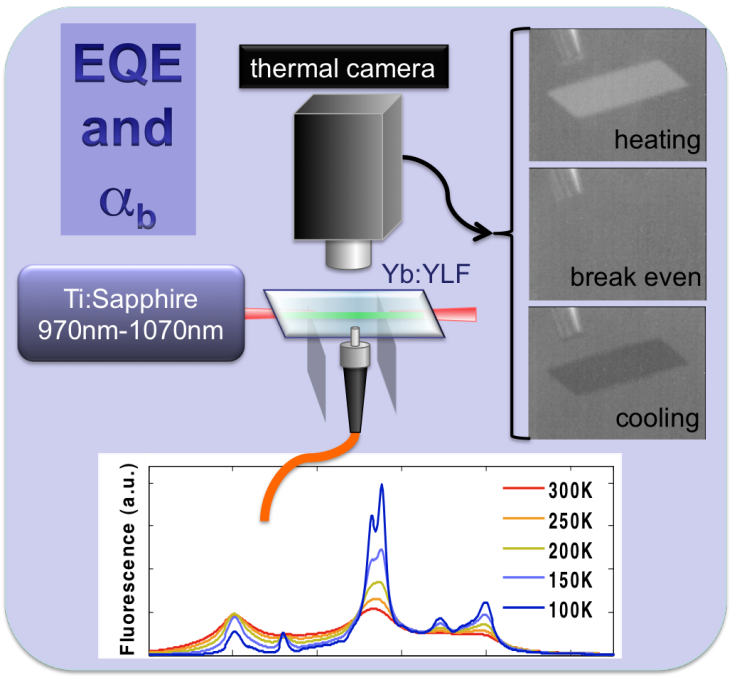


Figure 3.14: Experimental setup for measurement of $\eta_{ext}$ and $\alpha_b$

crystal is set on two 150$\mu$m thick glass slides to minimize the effect of any external conductive load, and pumped by a tunable Ti:Sapphire laser between 970nm-1070nm with ~2W of available power. The crystal temperature is monitored using a highly sensitive thermal camera and fluorescence is collected through a 600$\mu$m core fiber connected to the same Ocean Optics HR4000 used to measure the mean fluorescence

wavelength. The incident pump power $P_0$ is measured just before the crystal and the transmitted power $P_{tr}$ just after. The thermal image is collected using a Scion image frame grabber where measuring the change in pixel value is proportional to a change in temperature. Pixel values range from 0 to 256 with 1°C change corresponding to a pixel value change of 22 [16]. The linear response of the thermal camera is limited to temperature changes ±2°C (or 128±44 pixels), so the input power, $P_0$, is adjusted (and recorded) to maintain linearity. The change in pixel value normalized by the absorbed power is proportional to the cooling efficiency,

$$\eta_c \propto \frac{\Delta pixel}{P_{abs}}. \tag{3.13}$$

Beginning at 970nm, significant heating is observed. The steady state crystal temperatures are measured as the laser is tuned to successively longer wavelengths in increments of 10nm from 970nm-1070nm. $P_0$ is maintained to keep strong signal without saturating the thermal camera as absorption changes. Two zero crossing wavelengths are observed where the crystal changes from heating to cooling, and then from cooling back to heating.

The first zero crossing wavelength is defined as $\lambda_{cross}$, and allows the determination of $\eta_{ext}$ at room temperature from,

$$\eta_{ext} = \frac{\lambda_f(300K)}{\lambda_{cross}}. \tag{3.14}$$

The second crossing wavelength determines the background absorption by fitting the full form of Eq. 2.19 given the measured value of $\eta_{ext}$ and the room temperature quantities $\lambda_f$ and $\alpha_r$. The measured values (red) are plotted in Fig. 3.15 and fit (blue) with values of $\eta_{ext} = 99.5 \pm 0.1\%$, and $\alpha_b = 4 \pm 0.2 \times 10^{-4}(\text{cm}^{-1})$.

Continuing with the LITMoS test studies of other crystals, a wide range of results were found. The University of Pisa supplied four Brewster cut 5% wt. $Yb^{3+}$:YLF crystals, one Brewster cut 7.5% wt. $Yb^{3+}$:YLF crystal, one Brewster cut 30% wt. $Yb^{3+}$:YLF crystal, and four small ($\sim 3mm^3$) samples. AC Materials provided two

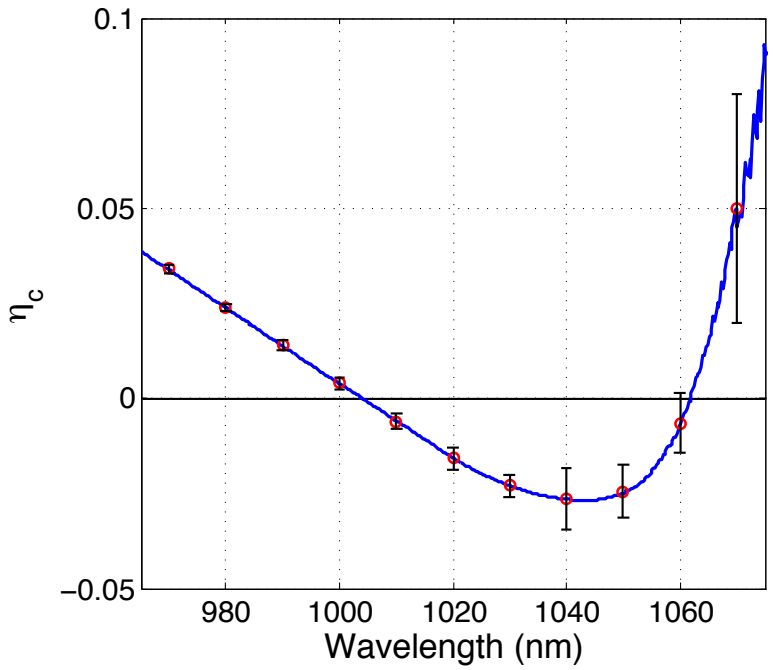


Figure 3.15: Experimental measurement and fit where $\eta_{ext} = 99.5 \pm 0.1\%$ and $\alpha_b = 4 \pm 0.2 \times 10^{-4}(\text{cm}^{-1})$ for the calculated $\alpha_r(\lambda, 300K)$. Only $\alpha_r$ for $E \parallel c$ is being considered since the absorption is significantly higher than $E \perp c$.

$\sim 1cm^3$ samples, one 1% and one 5% $Yb^{3+}$:YLF, and doping study samples with undoped, 1%, 5%, 7% and 10% doping with boules. The 10% boule sample was cut into two Brewster cut crystals for cooling experiments. Three of the Pisa crystals exhibited only heating. The 30% $Yb^{3+}$:YLF sample did not fit the cooling efficiency model, so no fit for $\eta_{ext}$ or $\alpha_b$ could be provided. All of the fits for each sample are shown in Figs.3.16, 3.17, 3.18, 3.19, 3.20, and 3.21 at the end of this section. The fits clearly show the line for zero crossings if the crystal exhibits cooling for reference.

In each fit, it can be seen that a higher background absorption is a direct result of where heating occurs at longer wavelengths. The clearest example is Fig. 3.20 where the shift in the long wavelength zero crossing correlates with significantly improved background absorption. In this figure, it appears that the short wavelength zero

| LITMoS test results for $Yb^{3+}$:YLF ctystal characteristics | | |
|---|---|---|
| | $\eta_{ext}$ (%) | $\alpha_b$ ($cm^{-1}$) |
| **University of Pisa Samples** | | |
| Brewster 5% $Yb^{3+}$:YLF #1 | 99.5(±0.1) | $4.0(\pm0.2)\times10^{-4}$ |
| Brewster 5% $Yb^{3+}$:YLF #2 | 98.8(±0.1) | $4.6(\pm0.2)\times10^{-4}$ |
| Brewster 5% $Yb^{3+}$:YLF #3 | 99.4(±0.1) | $4.4(\pm0.2)\times10^{-4}$ |
| Brewster 5% $Yb^{3+}$:YLF #4** | 97.0(±0.2) | $6.5(\pm0.1)\times10^{-3}$ |
| Brewster 7.5% $Yb^{3+}$:YLF** | 96.2(±0.6) | $7.0(\pm0.1)\times10^{-3}$ |
| Brewster 30% $Yb^{3+}$:YLF** | N/A heating only | N/A |
| $2mm^3$ 5% $Yb^{3+}$:YLF (a) | 99.6(±0.2) | $6.0(\pm0.2)\times10^{-4}$ |
| $2mm^3$ 5% $Yb^{3+}$:YLF (b) | 99.4(±0.2) | $4.4(\pm0.2)\times10^{-4}$ |
| $2mm^3$ 5% $Yb^{3+}$:YLF (c) | 99.25(±0.2) | $9.0(\pm0.2)\times10^{-4}$ |
| $2mm^3$ 5% $Yb^{3+}$:YLF (d) | 98.9(±0.2) | $1.6(\pm0.1)\times10^{-3}$ |
| **AC Materials, Inc.** | | |
| $1cm^3$ 1% $Yb^{3+}$:YLF | 99.3(±0.1) | $4.2(\pm0.2)\times10^{-4}$ |
| $1cm^3$ 5% $Yb^{3+}$:YLF | 99.7(±0.1) | $2.5(\pm0.1)\times10^{-3}$ |
| 1% $Yb^{3+}$:YLF 2mm ×10mm ×10mm | 99.6(±0.1) | $4.0(\pm0.2)\times10^{-4}$ |
| 5% $Yb^{3+}$:YLF 2mm ×10mm ×10mm | 99.5(±0.1) | $3.5(\pm0.2)\times10^{-4}$ |
| 7% $Yb^{3+}$:YLF 2mm ×10mm ×10mm | 99.5(±0.1) | $3.0(\pm0.2)\times10^{-4}$ |
| 10% $Yb^{3+}$:YLF 2mm ×10mm ×10mm | 99.6(±0.1) | $2.0(\pm0.2)\times10^{-4}$ |
| Brewster 10% $Yb^{3+}$:YLF #1 (melted) | 99.6(±0.1) | $2.0(\pm0.1)\times10^{-4}$ |
| Brewster 10% $Yb^{3+}$:YLF #2 | 99.6(±0.1) | $2.0(\pm0.1)\times10^{-4}$ |

Table 3.2: $Yb^{3+}$:YLF LITMoS test sample characterization. **Sample only exhibits heating. No fit could be made for the 30% sample. Blue samples exhibited the best performance from each source, therefore cooling experiments were performed.

crossing should effect the measurement of $\eta_{ext}$, however, because of higher doping in equally shaped samples, reabsorption shifts the mean fluorescence wavelength to longer wavelengths thereby maintaining the ratio $\lambda_f/\lambda_{cross}$ and therefore $\eta_{ext}$. Reducing the size of each crystal so that the reabsorption length for higher doped samples is equal to the lower doped samples will shift the short wavelength zero crossings on top of one another.

The sensitivity of the background absorption measurement is highlighted in Fig.

3.16 where sample #1, #2 and #3 all show background absorption values between $4.0\times10^{-4}\text{cm}^{-1}$ and $4.6\times10^{-4}\text{cm}^{-1}$. The zero crossing at 1060 nm moves from slight cooling (sample #1), to slight heating (sample #2) and break even (sample #3). Fig. 3.21 shows the comparison between the long wavelength heating in the 1% $Yb^{3+}$:YLF sample with un-doped YLF. When resonant absorption in the 1% $Yb^{3+}$:YLF sample goes to zero, the amount of heating should be equivalent to an un-doped sample, and therefore the background absorption of the un-doped sample is measured to be $4.4\times10^{-4}\text{cm}^{-1}$. This is useful for making a comparison with the trace element analysis in Ch. 6.

The source of the background absorption is impurities which cause heating and is taken to be independent of temperature [41]. In ZBLAN, the impurities that contribute to heating are the transition metals, which have broad absorption spectra. For instance, the absorption spectra of $Cu^{2+}$ spans ∼600nm-3000nm. For cooling to be observed, the purity levels must be low, <100 parts per billion (ppb) for most impurities, with copper, being particularly detrimental for cooling, must be <2 ppb [24]. In the cooling tail with a relatively small region of interest 1000nm-1060nm, and $\alpha_b$ on the order of $10^{-4}$, absorption in these impurities appear temperature independent. The source of background absorption for $Yb^{3+}$:YLF crystals has not been characterized previously. In Ch. 6, trace element analysis was performed to determine the concentrations of impurities, including the transition metals.

Along with the background absorption, the external quantum efficiency is also taken to be independent of temperature. High $\eta_{ext}$ such as the measured value of 99.5±0.1% means a very small non-radiative recombination rate. Small changes in non-radiative recombination would result in very small temperature dependence. Hoyt et al. [16] found a small increase (0.5%) in the external quantum efficiency for Tm:ZBLAN over a large temperature range (300K-77K). A similar increase for $Yb^{3+}$:YLF (∼0.25%) is comparable to the measurement error.

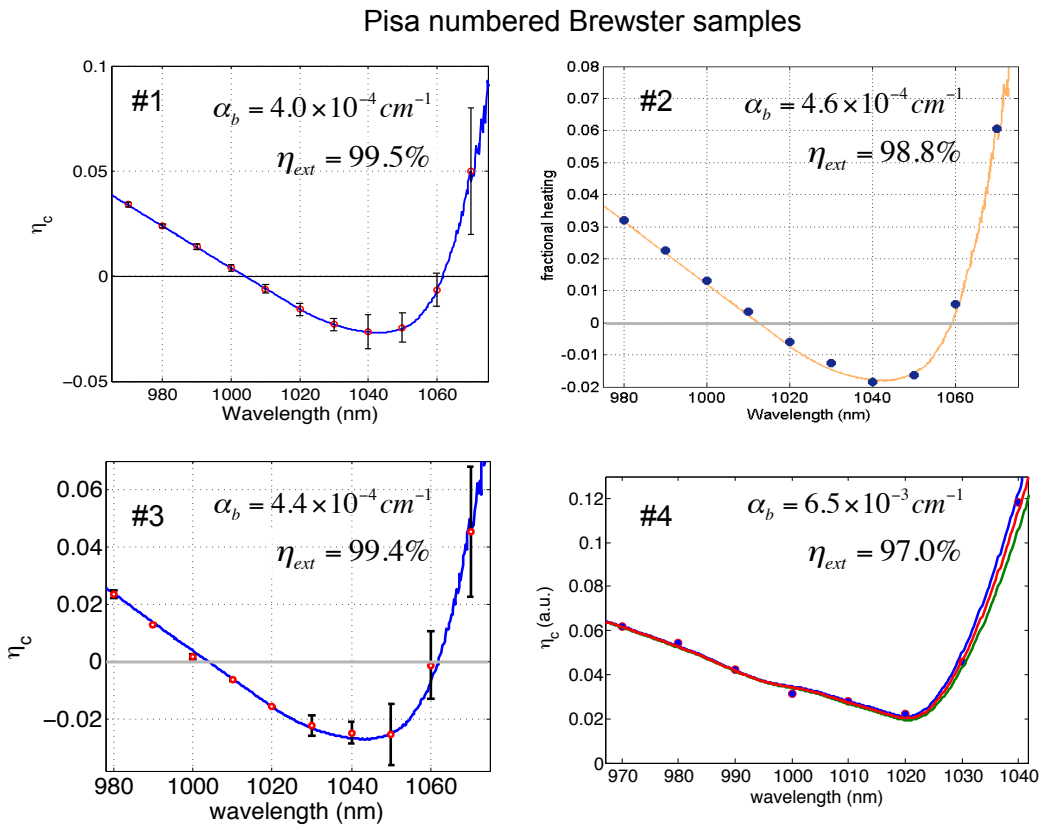


Figure 3.16: LITMoS test for Pisa samples $\#1 - \#4$. Without crossing zero, sample #4 does not cool.

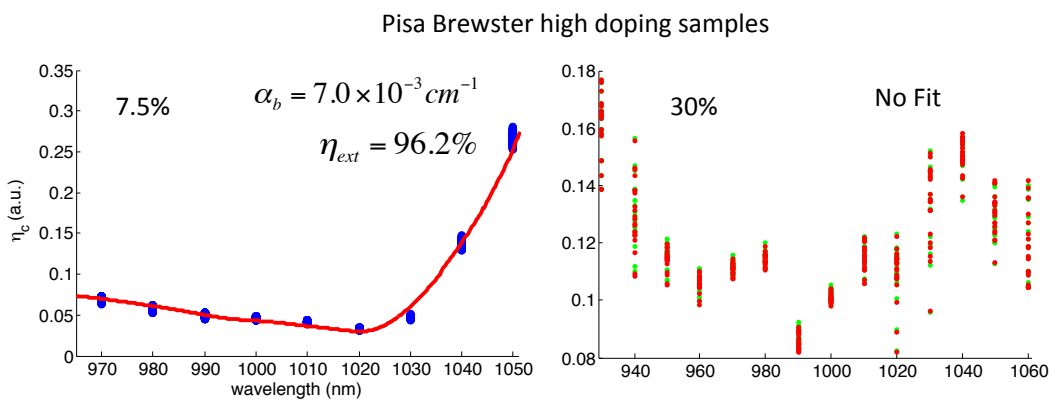


Figure 3.17: LITMoS test for Pisa samples 7.5% and 30%. Neither sample crosses zero, and hence do not cool. The 30% sample could not be fit.

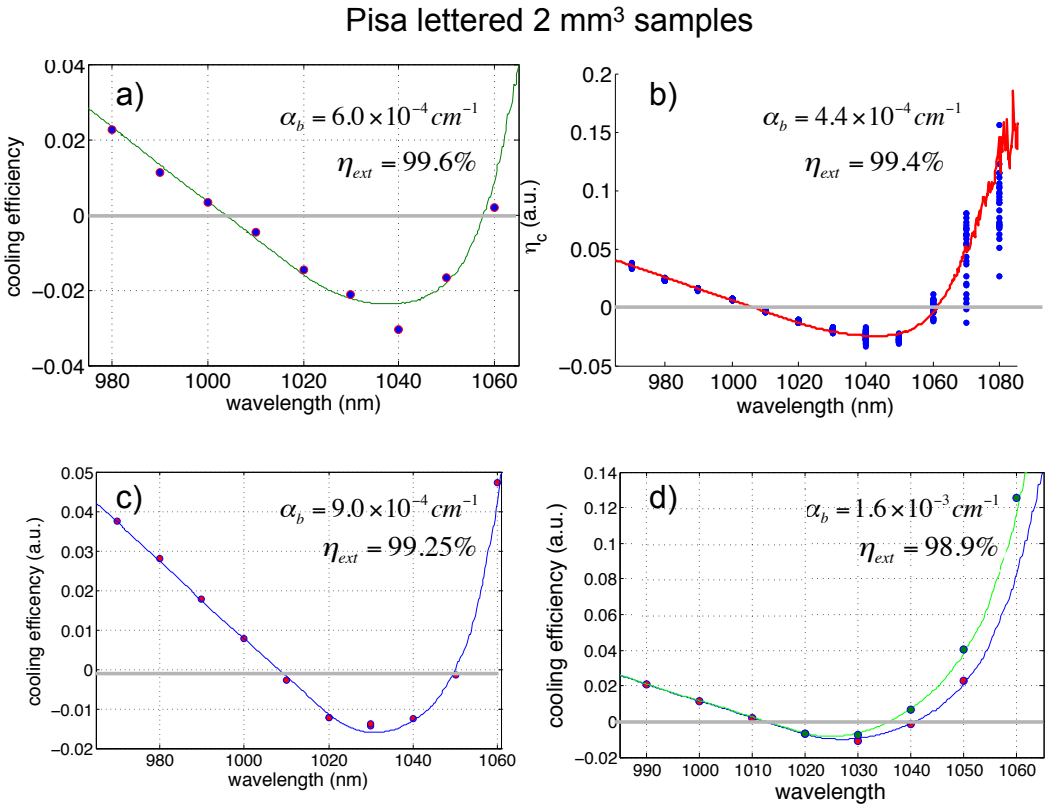


Figure 3.18: LITMoS test for lettered Pisa samples a)−b).

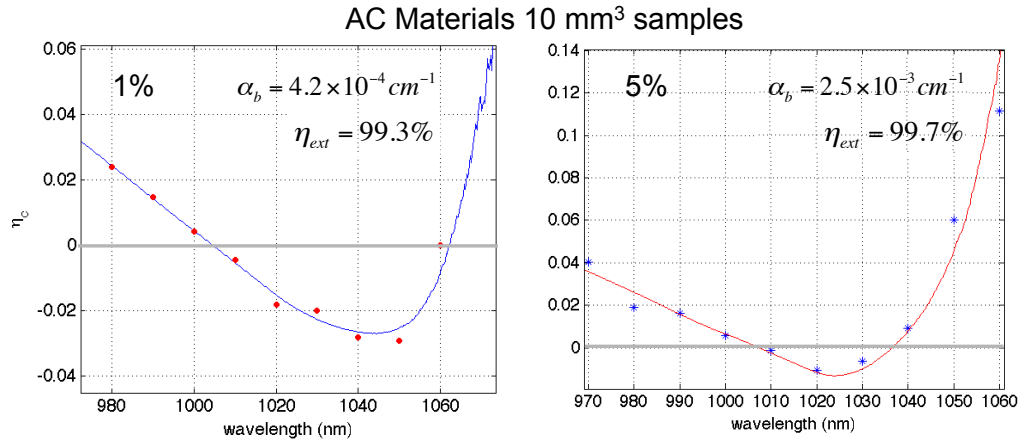


Figure 3.19: LITMoS test for 10 mm$^3$, 1% and 5% Yb$^{3+}$:YLF samples from AC Materials.

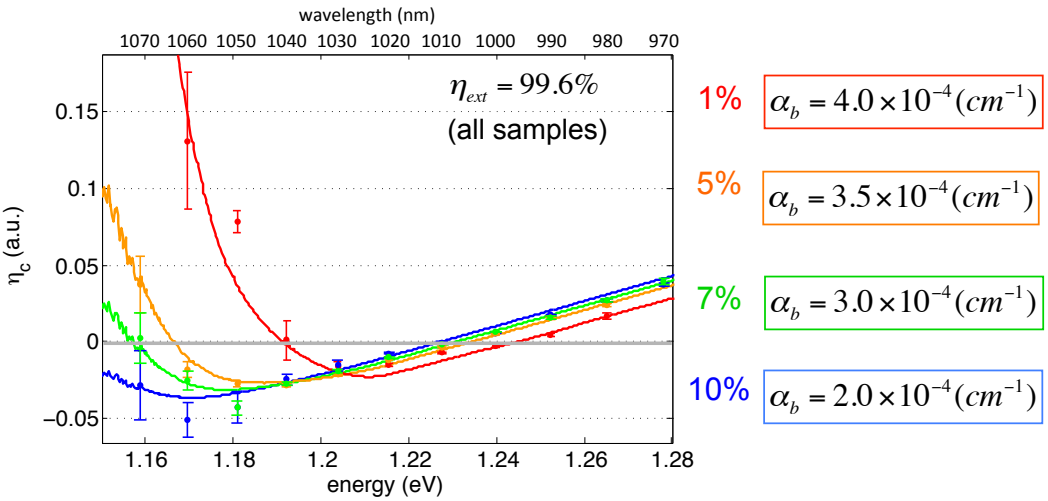


Figure 3.20: LITMoS test doping study samples 1%, 5%, 7% and 10% $Yb^{3+}$:YLF samples from AC Materials. The test was performed and converted to energy, therefore the x-axis is reversed. Above the plot gives wavelength.

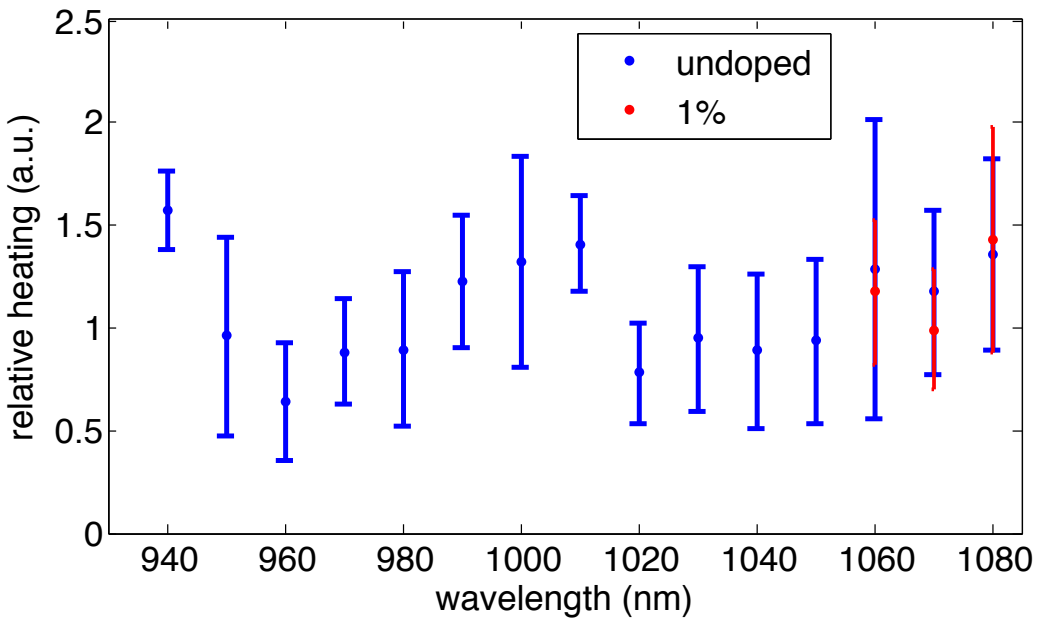


Figure 3.21: LITMoS test for un-doped YLF sample from AC Materials. Relative heating compared with the 1% sample at long wavelengths (low absorption) should reveal the relative background absorption.

## 3.4 Temperature dependent characterization of the cooling efficiency

The full form of the cooling efficiency, Eq. 2.19, requires four parameters to be measured for each of the samples. The four quantities measured in the previous section: the mean fluorescence wavelength $\lambda_f(T)$, the resonant absorption $\alpha_r(\lambda, T)$, the background absorption $\alpha_b$ and the external quantum efficiency $\eta_{ext}$, are combined, including the thermal dependence of the mean fluorescence and resonant absorption. The empirical model in Fig. 3.22 is created for temperature decreasing from 300K to 100K for sample #1 from the University of Pisa. (Each sample can create a series of curves similar to Fig. 3.22). Values below $\eta_c = 0$ denote cooling, and

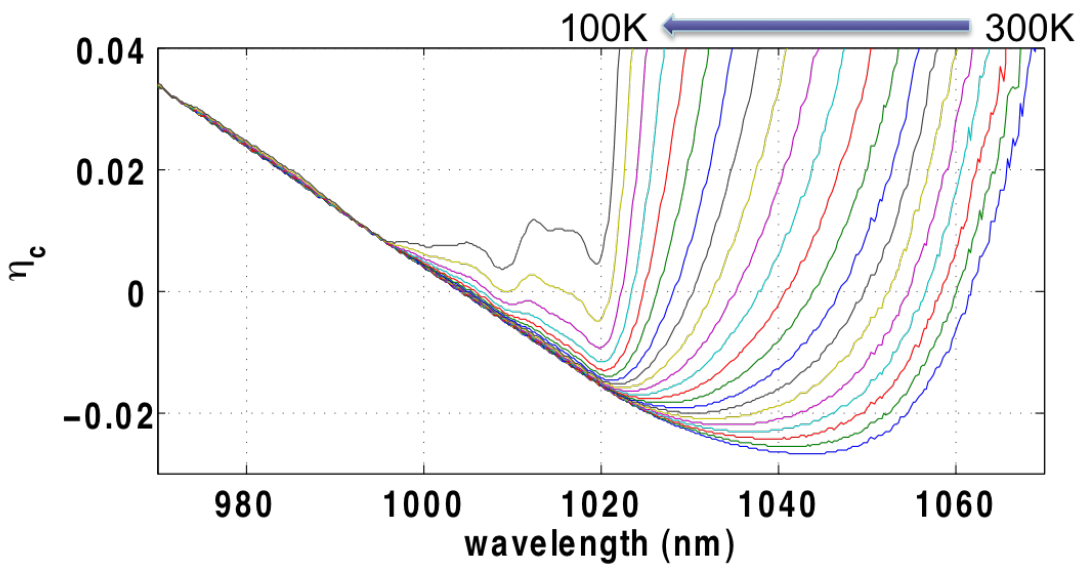


Figure 3.22: Calculated $\eta_c(\lambda, T)$ highlighting the thermal dependence.

therefore the minimum achievable temperature (MAT), given $\eta_{ext} = 99.5 \pm .1\%$ and $\alpha_b = 4.0 \pm .2 \times 10^{-4}(\text{cm}^{-1})$, is 110±5K. Re-plotting Fig. 3.22 as a contour map, Fig. 3.23, reveals the spectroscopic minimum achievable temperature (MAT) as the

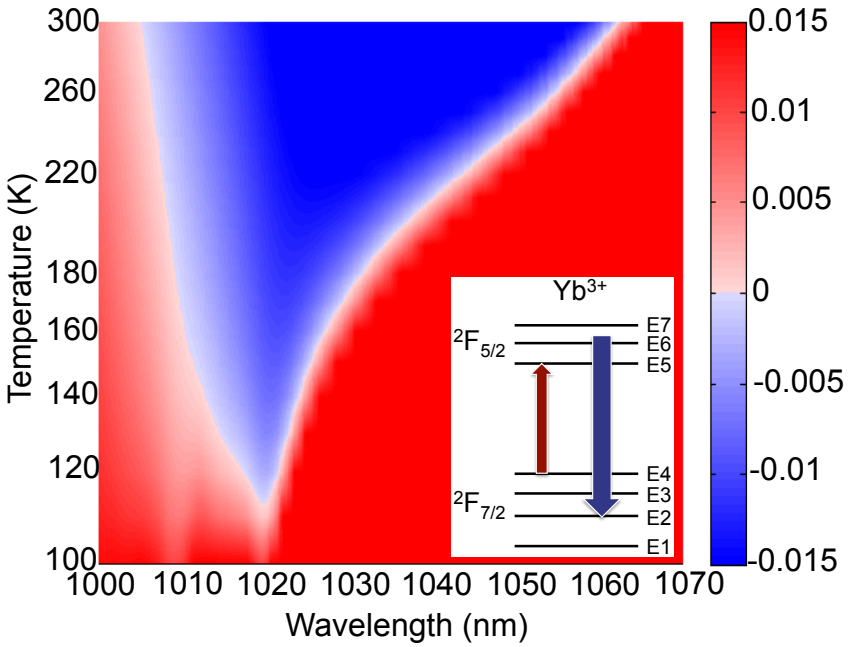


Figure 3.23: Cooling efficiency contour plot, $\eta_c(\lambda, T)$ for our Brewster cut 5% $Yb^{3+}$:YLF. Red regions denote heating, while blue denotes cooling. The global minimum temperature (gMAT) reaches 110K at 1020 nm corresponding to the E4−E5 transition in the Ytterbium ion.

white line transitioning between cooling (blue) and heating (red) regions. MAT is the temperature where, for a given wavelength, the cooling efficiency goes to zero, and regardless of increased absorbed power, lower temperatures cannot be reached. Fig. 3.23 also shows a clear global minimum achievable temperature (gMAT) which occurs when the sample is pumped at 1020nm. This wavelength corresponds to the E4-E5 transition in the Stark manifold, and given enough absorbed power, the crystal would reach temperatures near 110K. This cooling efficiency contour map is specific to sample #1 from Pisa. Improvements in any of the four quantities will push MAT to lower temperatures.

As a comparison, the cooling efficiency map for the 10% $Yb^{3+}$:YLF sample from AC Materials is plotted in Fig. 3.24. The clear advantages of this sample are doubled

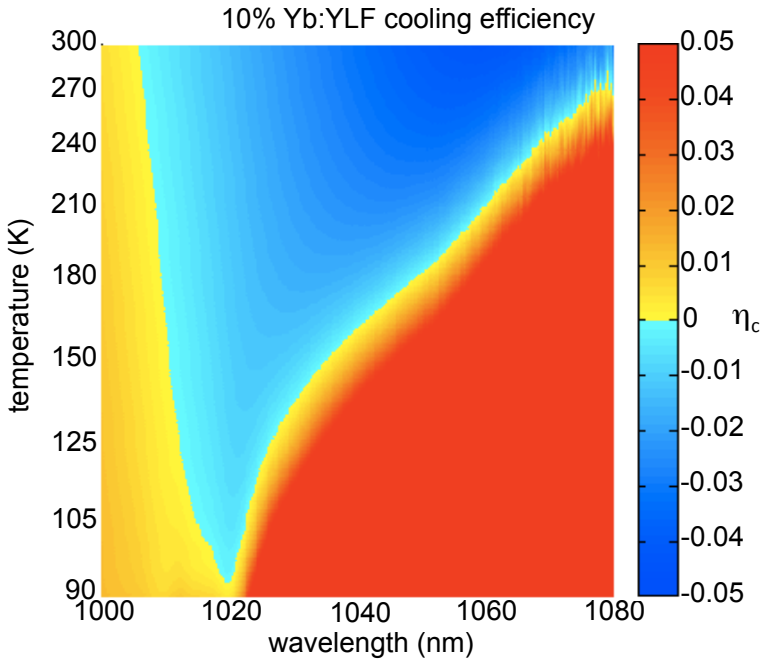


Figure 3.24: Cooling efficiency contour plot, $\eta_c(\lambda, T)$ for the Brewster cut 10% $Yb^{3+}$:YLF sample grown by AC Materials.. Red regions denote heating, while blue denotes cooling. The global minimum temperature (gMAT) reaches 93K at 1020 nm corresponding to the E4−E5 transition in the Ytterbium ion, marking the first sample anticipated to cool below 100K via optical refrigeration.

resonant absorption with half of the background absorption. If we look at the effect on the absorption efficiency, Eq. 2.18, rewritten as,

$$\eta_{abs} = \frac{1}{1 + \alpha_b/\alpha_r(\lambda, T)}, \tag{3.15}$$

the ratio of $\alpha_b/\alpha_r(\lambda, T)$ increase four times while the minimum achievable temperature improves from 110K to 93K. This sample marks an important milestone in optical refrigeration: it is the first sample anticipated to cool **below 100K**.

The cooling performance of these crystals is truly cryogenic. The National Institute of Standards & Technology (NIST) defines cryogenic as -150°C corresponding to 123K. This is the just above the boiling point of methane (112K). Both the 5% $Yb^{3+}$:YLF crystal with a gMAT of 110K and the 10% $Yb^{3+}$:YLF crystal with gMAT

of 93K place the performance of optical refrigeration below the cryogenic temperature defined by NIST, a major milestone on the path towards creating an all solid-state optical cryo-cooler. Improved cooling performance can be accomplished by further decreasing the background absorption, or equivalently increasing doping while maintaing background absorption. Modeling has been performed for a sample with 5% doping concentration and external quantum efficiency of 99.5% with reducing background absorption. Fig. 3.25 shows that substantial improvements have already been

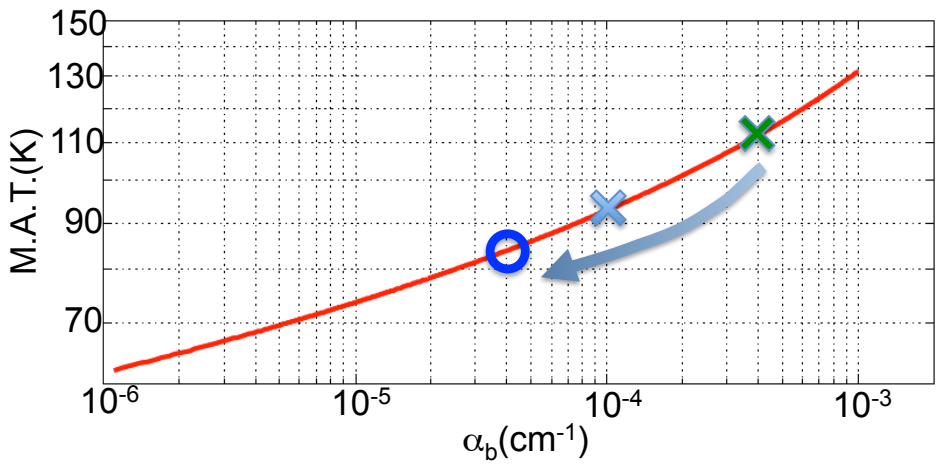


Figure 3.25: Modeling which shows the decrease in minimum achievable temperature (MAT) as the parasitic background absorption is decreased.

accomplished. For the case of the 10% $Yb^{3+}$:YLF crystal, the equivalent background absorption improvement is four times shown as the light blue X. Continuing on this path to success, optical refrigeration will begin approaching liquid nitrogen temperatures (77K). LITMoS

# Chapter 4

# Cryogenic Optical Refrigeration

## 4.1 Introduction

According to the empirical modeling in Ch. 3, cooling in $Yb^{3+}$:YLF crystals easily surpasses the capabilities of all other solid state cooling devices and even goes beyond cryogenic temperatures. It is now necessary to experimentally verify the cooling performance. This chapter is concerned with maximizing the change in temperature of $Yb^{3+}$:YLF crystals. Referencing Fig. 2.4, $\eta_c$ has been addressed and improved. The next step is two fold: minimize $P_{load}$ and maximize $P_{abs}$. A number of major milestones in optical refrigeration were achieved and highlighted, including the first temperatures below the NIST defined cryogenic temperature of 123 K by all solid state means. This was accomplished for a 5% $Yb^{3+}$:YLF crystal, grown at the University of Pisa, where MAT was reached at ∼118 K. Additionally cooling was performed for the 10% $Yb^{3+}$:YLF sample with MAT of ∼93 K from AC Materials where a record low temperature of ∼114 K was achieved.

Achieving this record result required overcoming several experimental challenges, such as: heat load management, absorption enhancement, and non-contact tempera-

ture measurement. Presented first are the significant efforts regarding heat load management, then the full experimental results utilizing two different photon trapping schemes as well as the performance comparison with the empirical values discussed are in Ch. 3.

## 4.2 Heat load management

As discussed in Ch. 2, there are three heat load sources which need to be minimized: convective, conductive and radiative. A high vacuum removes the convective load which will be described briefly. To reduce the conductive and radiative loads required significantly more attention, and is addressed through the design and machining of a specialized copper structure. Estimations are made near the end of this section with the parameters of the completed structure. Rewriting the Eq. 2.23 here for convenience,

$$C(T)\frac{dT}{dt} = \eta_c P_{abs} + A_s \kappa_h (T_c - T_s) + \frac{N\kappa_L(T) A_L}{d_L}(T_c - T_s) + \frac{\varepsilon_s A_s \sigma}{1+\chi}(T_c^4 - T_s^4). \quad (4.1)$$

it is possible to see what should be done experimentally to reduce each source of heat load by minimizing the parameters.

The convective heat load is minimized by placing the crystal inside an aluminum vacuum chamber which is evacuated to a pressure of $10^{-6}$ torr. The aluminum vacuum chamber is not ideal for pulling high vacuums due to outgassing, however the achieved pressure is two orders of magnitude lower than the acceptable pressure of $10^{-4}$ torr. An Edwards XDS5 (oil free) scroll pump primes the chamber while an Alcatel 5150 turbo-molecular pump pulls a high vacuum over the period of about 12 hours. Pressure is initially measured through a thermocouple pressure gauge while priming the chamber and an ion gauge gives the final value after lengthy pumping.

To address the conductive and radiative heat loads, a specialized copper structure

was designed and machined. Using Google SketchUp, a free program, a solid model was designed to scale. The program can be understood quickly and allows the user to design an entire structure component-wise to visualize the fitment and address any real world problems prior to manufacturing. The fundamental issues that needed to be addressed include:

- Safely mounting a delicate sample with an absolute minimum amount of contact with its enclosure to reduce the conductive load;
- Enclosure closely surrounding the crystal, with $< 1$ mm separation between the crystal and the internal walls of the structure, and lining its enclosure with a low emissivity material to reduce radiative load;
- Rigidly mounting mirrors and coupling mirror mounts to create a cavity (resonant and non-resonant) in which to place the crystal while still being able to adjust the mirrors for alignment;
- Supplying a high voltage feedthrough to actively control one of the piezo-activated mirrors externally;
- Maintaining clamshell, base and mirrors at room temperature with water line feedthroughs;
- Good thermal contact between each component.
- Access to fluorescence via a fiber feedthrough with an SMA connector. This is to monitor the crystal temperature through a novel, non-contact method known as differential luminescence thermometry (DLT), which will be discussed in Appendix A and mentioned in the text;
- Pump access accounting for the Brewster geometry of the crystal;
- Vented screws to prevent virtual leaks.

Taking into consideration all of these concerns as well as keeping the manufacturability practical (i.e. standard hole sizes, standard screws, reasonable tolerances, etc.), a design was created and can be seen in Fig. 4.1. Three different views are used to help visualize the full structure. Fig. 5.14(b) and Fig. 5.14(d) show the entire struc-

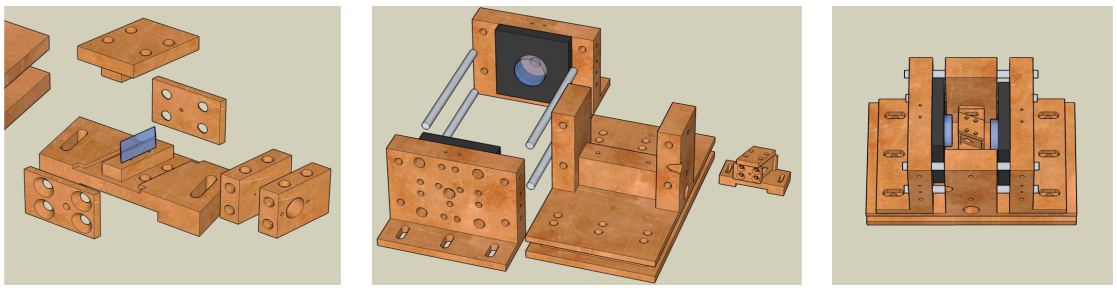

(a) Exploded clamshell view (b) Exploded component view. Mirror mounts, base, and clamshell (c) Complete model

Figure 4.1: These are images of the 3-D model created using Google SketchUp

ture in a separated view and assembled view respectively. Perhaps the most crucial component, Fig. 5.14(a) is an expanded view of the "clamshell", the term coined to describe the tight fitting structure surrounding the crystal. The clamshell walls are $< 1mm$ from the crystal when assembled. This tight fitting structure reduces the radiative load by increasing $\chi$ in Eq. 2.24.

Each clamshell surface facing the crystal is lined with a solar selective coating. A solar selective coating has high absorption at short wavelengths and low emission at long wavelengths. Experiments were performed with the solar selective coating Maxorb (absorptance at near infra-red (NIR) $\alpha = 0.88 - 0.96$, emittance $\varepsilon = 0.03 - 0.10$). More recently a second coating was acquired, the Acktar Nano Black coating, which is provided as a foil with adhesive backing, or direct deposition on the clamshell pieces. Fig. 4.2 shows the reflectivity properties of the Nano Black coating. An estimate for the effectiveness of Maxorb show that it minimizes the black-body radiative load by a factor of six while dumping nearly all of the optically emitted heat into

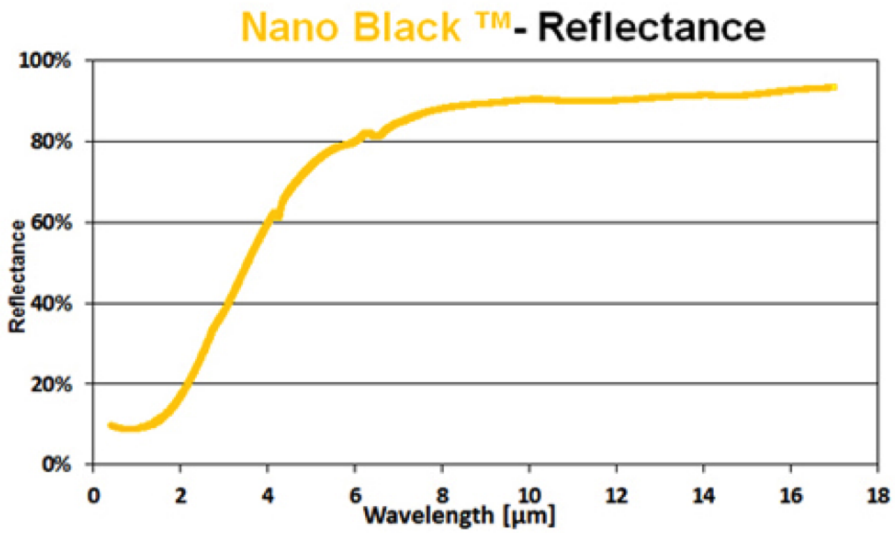


Figure 4.2: Acktar Nano Black solar selective coating reflectance available from their website: http://www.acktar.com/category/NanoBlack.

the clamshell [14]. Two images of Maxorb next to aluminum foil can be seen in Fig. 4.3. The image on the left is an image from a thermal camera, and on the right is a visible image. It is clear from these images that Maxorb is highly absorbing of visible wavelengths, including the near-IR $Yb^{3+}$ fluorescent wavelengths, while it is highly reflective in the mid-IR.

The clamshell not only reduces the radiative load, but also provides a way to mount the crystal while minimizing the conductive load. The clamshell itself is maintained at room temperature through good thermal contact with the base. To minimize the conductive heat load, it is necessary to remove as much contact the crystal has with the clamshell as possible. This is accomplished by supporting the crystal on six, 500$\mu$m glass fibers, three vertical supports and three horizontal. These fibers are sturdy enough to provide adequate support for the crystal with minimal contact. Each fiber is manually cleaved and filed to a point so that very little of the surface is in direct contact with the crystal. The base and side walls of the clamshell

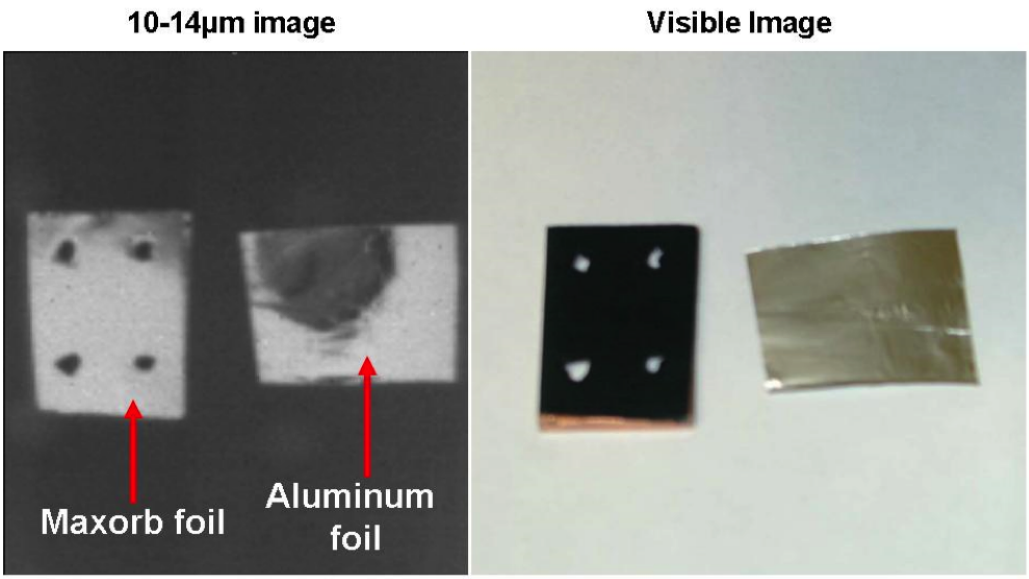


Figure 4.3: Images of Maxorb and aluminum foil at IR and visible wavelengths. Visually, Maxorb is clearly highly reflective at $10-14\mu$m and highly absorptive at visible wavelengths

in Fig. 5.14(a) have been fitted with small holes which provide various locations to glue the fibers supporting the crystal. Extra holes were made to allow for mounting adjustment.

Now that each of the heat loads have been addressed, it is useful to analyze each heat load source to ensure adequate reduction. The convective load from Eq. 2.23 is $A_s\kappa_h(T_c-T)$. A crude estimate of the reduction in convective heat load as a function of pressure can be done using,

$$\frac{\tilde{\kappa}_h}{\kappa_h} = \frac{1}{1+\frac{C}{Pd/T}}. \tag{4.2}$$

where $\tilde{\kappa}_h$ is the reduced convective heat transfer coefficient at lower pressure P to $\kappa_h$ at standard pressure, with a sample at temperature T separated from a chamber with distance d. The constant, C= $7.6\times10^{-5}N/mK$ approximates the relationship [42]. Reducing pressure to $10^{-5}$ torr from 760 torr in a chamber where d= 1mm at 300K reduces the coefficient by $h_e/h\approx 6\times10^{-5}$, and at 100K by $h_e/h\approx 17\times10^{-5}$.

At 300K air has convective heat transfer coefficient between 5-25 $W/m^2K$ therefore at $10^{-5}$ torr, the product $A_s h \approx 1.5\times10^{-7}$W/K.

The conductive heat load is reduced by minimizing the contact the sample has with the chamber. Considering the case where six, 500$\mu$m diameter, glass fibers support the sample with thermal conductivity $\kappa \approx 1.0$ W/mK with a distance d= 1mm from the chamber, $\frac{N\kappa_L(T)A_L}{d_L} \approx 1.1 \times 10^{-3}$W/K. This estimate accounts for perfect thermal contact between the sample and the supports as well as between the supports and the chamber, when in reality, a small fraction of each fiber support is actually in contact with either surface. Generously estimating perfect contact with the chamber and $A_L/10$ of each fiber contacting the sample leads to $\frac{N\kappa_L(T)A_L}{d_L} \approx 1.2\times10^{-5}$W/K. Obviously from these estimates, the convective load from the previous paragraph can be ignored.

The radiative load has always been assumed to be the largest contributor to $P_{load}$, and has been verified as the largest contributor when monitoring the warming dynamics after turning off the pump at low temperatures [31]. To make a proper comparison, assume small temperature changes so that the radiative term, $P_{rad}$, can be approximated as,

$$P_{rad} = \left(\frac{1}{1+\chi}\right) 4\varepsilon_s \sigma A T_c^3 \Delta T. \tag{4.3}$$

A non-trivial numeric fit to the warming dynamics in [31] gives $\chi = 2.1$ and $\varepsilon_s \sim 0.8$ for a sample with area $A_s \sim 1.5\text{cm}^2$, bearing in mind measurements were taken to reduce the radiative load by factor of six which will be discussed in Ch. 4 [14]. With $T_c$=300K, the factor preceding $\Delta$T is calculated to be $\left(\frac{1}{1+\chi}\right) 4\varepsilon_s \sigma A T_c^3 \approx 2.4 \times 10^{-4}$W/K, 20 times larger than the conductive load, and removing the factor of six increases to $\approx 4.4 \times 10^{-3}$W/K.

Taking into account the relative contributions of the heat loads with the radiative

load largest by two orders of magnitude, in steady state (dT/dt=0),

$$P_{cool} = P_{rad} = \left(\frac{1}{1+\chi}\right)\varepsilon_s \sigma A_s (T_c^4 - T_s^4). \tag{4.4}$$

To minimize this load, $\chi$ defined in Eq. 2.24 should be maximized. This is accomplished by enclosing the sample in a tightly fitting clamshell chamber so that $A_s \approx A_c$, while the emissivity of the chamber walls is reduced as much as possible so that $\varepsilon_c \ll \varepsilon_s$ by coating with a solar selective material. Any further reduction of the heat load can be accomplished by reducing the temperature of the clamshell. This reduction was performed as a proof of principle experiment in Sec. 4.3.5 to verify the MAT condition of the 5% $Yb^{3+}$:YLF crystal.

Each of the remaining concerns were addressed (i.e. proper mirror mount dimensions, etc.) and the structure was machined out of oxygen free high conductivity (OFHC) copper. The actual structure can be seen, in-situ, in Fig. 4.4, where it shows the crystal, with visible blue/green up-conversion, placed inside the copper clamshell (the lids of the vacuum chamber and clamshell have been removed for visible access). The copper mirror mounts were designed to accept standard Thorlabs mirror mounts which can be adjusted for alignment prior to evacuating the chamber. One of the mirror mounts can be controlled externally by a 3-axis piezo controller once the experiment is under vacuum, allowing for small adjustments when using a resonant cavity (Sec. 4.3.1). Three thermocouples monitor the temperatures of a mirror mount, the clamshell, and the base, to provide real time temperature measurement. A fiber feed-though allows access to the fluorescence of the crystal which is monitored using an Ocean Optics HR4000 spectrometer (200 nm-1100 nm wavelength range, ~1nm resolution using 10$\mu$m slits). Because the fluorescence shape changes with the crystal temperature, it is possible, after careful calibration, to measure the crystal temperature simply by monitoring its fluorescence. This non-contact measurement technique, called differential luminescence thermometry (DLT), does not introduce a heat load. It was developed for use in semiconductors [43], crystals

and glasses, [17], [44], or a combination[45], [28], [33] and will be discussed in Appendix A. A labview program was written to collect real time temperature data from the thermocouples and calculate the DLT, shown in Figs. 4.10 and 4.15

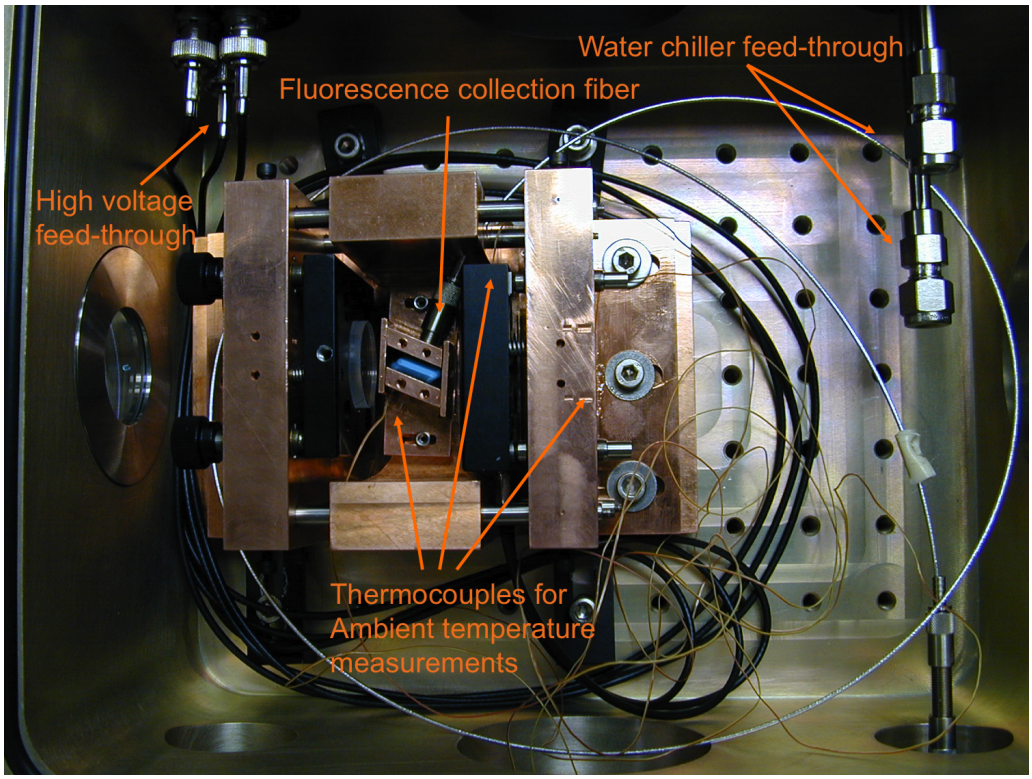


Figure 4.4: Full chamber setup. The copper structure contains a base, mirror mounts and a clamshell. The mirror mounts are held rigidly together via connecting rods to help remove vibrational noise, and the clamshell closely surrounds the $Yb^{3+}$:YLF crystal which mounts directly to the copper base. Water flows through the copper base to maintain it at room temperature. The image shows the water lines disconnected. There is a high voltage feed-through to allow in-situ positional adjustments via a 3-axis piezo-electric mirror mount. The whole assembly is placed inside an aluminum vacuum chamber which is evacuated to $10^{-6}$ torr. There are three thermocouples used to monitor the temperature of the mirror mount, clamshell, and base independently. An optical fiber mounts directly to the clamshell to monitor the fluorescence of the crystal. A 1030 nm mirror was used in front of the camera lens to show the blue/green upconversion and block the IR which appears as a false purplish color in a camera.

## 4.3 Experimental results

Experiments were conducted consisting of two different photon trapping schemes: resonant and non-resonant cavities. Photon trapping is done to increase cooling power by increasing the number of pump photons absorbed in the $Yb^{3+}$:YLF crystal. Mentioned in Ch. 2, cooling power is given by $P_{cool} = P_{abs}\eta_c$, where $P_{abs} = P_0(1 - e^{-\alpha L})$, therefore increasing the absorption length increases the absorbed power. For both of these photon trapping schemes, the absorption length is increased by the number of passes, $N$, through the crystal so that $L = NL$. To improve transmission through the crystal, the entrance and exit faces were cut a Brewster's angle with a $\pi$-polarized pump. With proper alignment, <0.01W is reflected. Two different laser sources were utilized. Initially the available pump source was a tunable Yb:YAG thin disk ELS laser which was only capable of tuning to 1023 nm while maintaining $\sim$ 10 W of pump power. Shorter wavelengths resulted in significantly reduced power and were therefore unusable. This laser was used in both resonant and non-resonant cavity configurations. A new pump source was specially developed by IPG Photonics for optical refrigeration experiments which is a Yb-doped fiber laser providing 55 W CW power near 1020 nm. The 1020 nm fiber laser was only used in a non-resonant configuration since the bandwidth is too broad ($\sim$0.5 nm) for the resonant cavity.

### 4.3.1 Resonant cavity

One possible way to increase absorption is by placing the sample in a resonant cavity, known as resonant cavity-enhanced (RCE) absorption [46, 47, 34, 48][1]. A resonant cavity can, under appropriate conditions (impedance matching, resonance, etc.), be shown to have near unity absorption. To obtain the impedance matching condition [46], first consider the electric field inside the resonator (Fig. 4.5 ), which is the sum

[1]Interestingly, this technique was recently rediscovered and termed an anti-laser [49]

of all the round trips where a single round trip is given by $E_{i,1} = t_1 E_0 r_2 r_1 e^{(2ikd-2\alpha L)}$,

$$E_i = t_1 E_0 \sum_{n=0}^{\infty} (r_1 r_2)^n e^{2n(ikd-\alpha L)} = \frac{t_1 E_0}{1 - r_1 r_2 e^{2(ikd-\alpha L)}}. \tag{4.5}$$

$E_0$ is the incident electric field, $r_{1,2}$ ($t_{1,2}$) are reflection (transmission) coefficients for each mirror, d is the effective cavity length (including any index of refraction), $k = 2\pi/\lambda$ is the wavenumber and $\alpha$ is the absorption coefficient of and absorber length L. The intra-cavity intensity is,

$$I_i = \frac{T_1}{\left|1 - \sqrt{R_1 R_2} e^{(2ikd + i\phi - 2\alpha L)}\right|^2} I_0, \tag{4.6}$$

where $I = |E|^2$ with the transmission and reflection coefficients $t_{1,2} = \sqrt{T_{1,2}} e^{i\phi_{1,2}}$, $r_{1,2} = \sqrt{R_{1,2}} e^{i\phi_{1,2}}$. Then the transmitted field can be calculated from the internal field,

$$E_t = \frac{t_1 t_2 e^{ikd-\alpha L}}{1 - r_1 r_2 e^{2(ikd-\alpha L)}} E_0. \tag{4.7}$$

$$I_t = \frac{T_1 T_2}{\left|1 - \sqrt{R_1 R_2} e^{(2ikd + i\phi - 2\alpha L)}\right|^2} I_0. \tag{4.8}$$

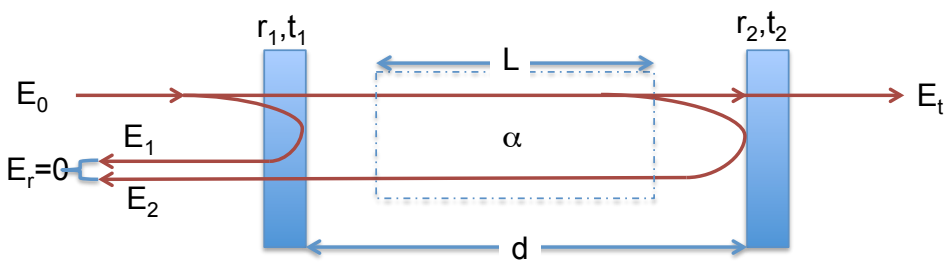


Figure 4.5: Impedance matching cavity diagram. The labels: $r_{1,2}$ are reflection coefficients and $t_{1,2}$ transmission coefficients for the input mirror (1) and the back reflecting mirror (2), $E_0$, $E_r$ and $E_t$ are incident, reflected and transmitted electric field, d is the effective length of the cavity (including any index of refraction changes), L is the length of the absorber with absorption $\alpha$.

The reflected field is composed of two pieces: $E_1$ directly reflected from the first mirror, and $E_2$ the transmitted portion from inside of the resonator. Adding these portions gives,

$$E_r = \left[-r_1 + \frac{r_2 T_1 e^{i2kd-2\alpha L}}{1 - r_1 r_2 e^{2(ikd-\alpha L)}}\right] E_0. \tag{4.9}$$

$$I_r = \frac{\left|-1 + \left(1 + \frac{T_1}{R_1}\right)\sqrt{R_1 R_2} e^{2ikd+i\phi-2\alpha L}\right|^2}{\left|1 - \sqrt{R_1 R_2} e^{(2ikd+i\phi-2\alpha L)}\right|^2} R_1 I_0. \tag{4.10}$$

The exponent on top of the fraction requires two passes through the cavity, and hence absorbing medium, in order to be back-reflected through the first mirror which accounts for the two. When the resonant cavity condition is met, $2kd+\phi = 2n\pi$, the exponent $e^{2ikd+i\phi-2\alpha L} \longrightarrow e^{-2\alpha L}$. Then requiring the impedance matching condition, $I_r = 0$ gives, (substituting $T_1 = 1 - R_1$),

$$0 = -1 + \left(1 + \frac{1 - R_1}{R_1}\right)\sqrt{R_1 R_2} e^{-2\alpha L} \tag{4.11}$$

Rearranging and solving for the reflectivity of the input mirror gives [47, 34, 48],

$$R_1 = R_2 e^{(-2\alpha L)}, \tag{4.12}$$

This is the impedance matching condition. Absorption is the difference between transmitted and reflected intensities, $A = 1 - T - R \sim 1 - R$ as ($R_2 \sim 1$). Absorption on resonance with $R_2 = 1$ is,

$$A = 1 - \left(\frac{\sqrt{R_1} - e^{-\alpha L}}{1 - e^{-\alpha L}\sqrt{R_1}}\right)^2 \tag{4.13}$$

which goes to unity at the impedance matching condition, i.e. $R_1 = e^{-2\alpha L}$. Fig. 4.6 gives reflectivity values for different sample conditions ($\alpha L$). It should be noted that $\alpha$ is both wavelength and temperature dependent, so it is necessary to choose the correct input coupler for the pump wavelength in use and the final temperature

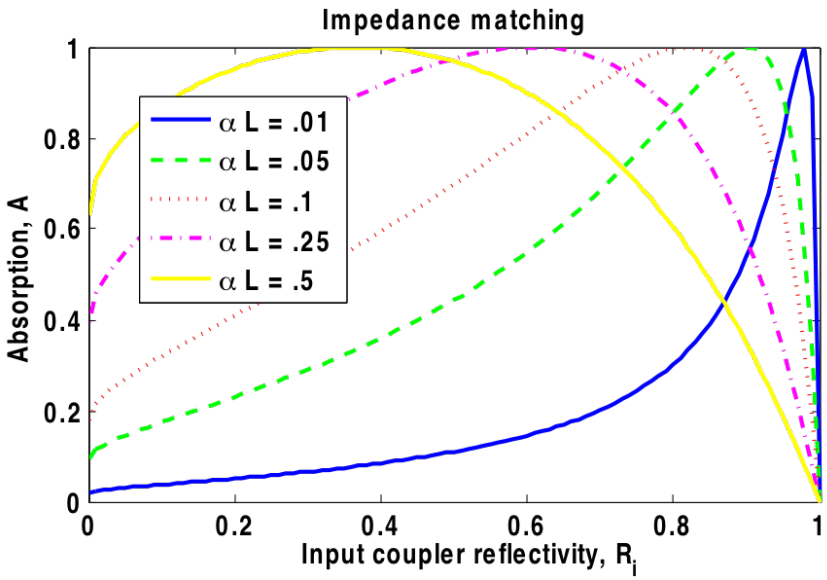


Figure 4.6: Impedance matching conditions for given $\alpha L$. Note that $\alpha$ is really a function of temperature, so the correct choice of input coupler depends on what temperature the experiment is expected to reach.

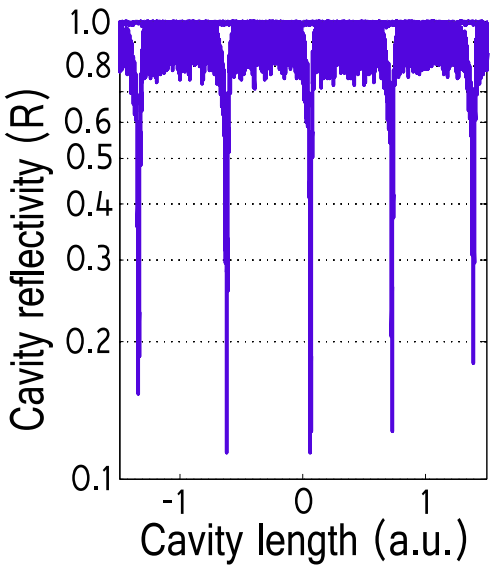


Figure 4.7: Reflectivity measurements in the RCE experiment [47].

that is expected instead of the starting temperature. Fig. 4.7 shows a measurement of reflection from the RCE experiment, where the cavity resonances correspond to absorption of 89±3% (nearly a factor of 20× enhancement compared to single-pass absorption).

### 4.3.2 RCE experimental results with ELS laser

Resonant cavity-enhanced absorption is ideal for laser cooling because cooling power scales with absorbed power, and a resonant cavity provides complete absorption. Indeed, the first record result reaching a temperature of 203 K was achieved using the resonant cavity as can be seen in Fig. 4.10 [48]. Using the newly machined copper structure described in Sec. 4.2, a resonant cavity design was used to maximize absorption, pumping the crystal with an ELS Versadisk laser centered at 1030 nm with $\sim$ 40 W of CW power, Fig. 4.8. The pump is isolated from the cavity by two Faraday rotators (60 dB combined rejection). The high-power half wave-plate with high-power polarizing beam splitter allows for adjustment of the incident power without changing the laser power directly, improving laser stability, as well as splitting a portion of the beam into stability monitoring cavity. Interferometric alignment of the cavity is accomplished via a 3-axis-controlled piezo-actuated mirror, while cavity resonance was maintained my tandem control of the 3-axes simultaneously by means of a feedback loop. The sample is held inside the copper structure discussed in Sec. 4.2 which is inside an aluminum enclosure held at $\sim 10^{-6}$ torr.

Using sample #1 from the University of Pisa, previous experiments were able to achieve a temperature drop of 70 K from room temperature utilizing a resonant cavity, without the radiative load management, pumping with 15 W at 1030 nm (see Fig. 4.9)[34]. Utilizing the clamshell for heat load reduction, and beginning with the pump laser tuned to the peak gain at 1030 nm and  40 W to achieve the maximum

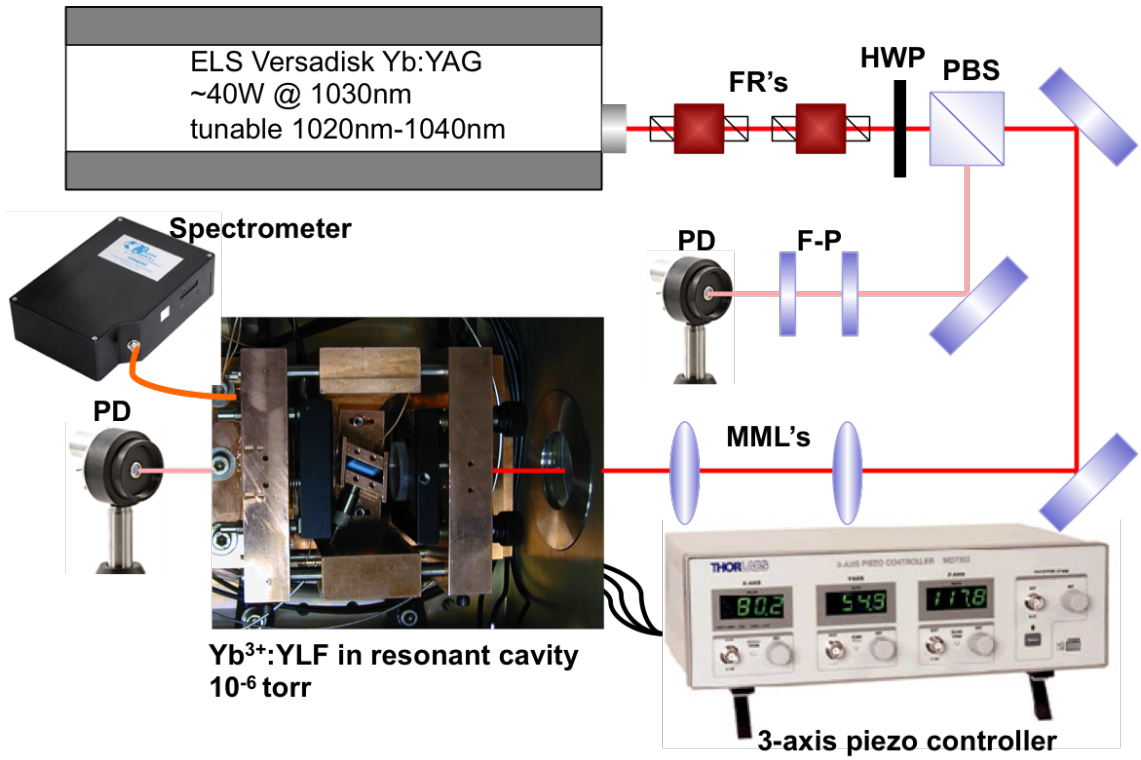


Figure 4.8: RCE setup. The acronyms are as follows: FR's: faraday rotators, HWP: half wave plate, PBS: polarizing beam splitter, PD: photo-detector, F-P: Fabry-Perot interferometer, MML's: mode-matched lenses.

absorbed power, the crystal cooled to 230 K. The laser was then tuned closer to the absorption peak at 1020 nm. Even though the laser power drops rapidly and impedance matching is degraded, improved cooling was observed. A minimum of 203 K was reached at 1023 nm with 9 W of pump power, the first record cooling result. The laser, tuning to wavelengths shorter than 1023 nm, could not result in enough absorbed power to improve cooling. Fig. 4.10 shows the record cooling data for the resonant cavity. The roughness exhibited by the crystal temperature is due to pump tuning , re-optimizing the cavity with the piezo controlled mirror and waiting for the temperature to reach its minimum before making subsequent adjustments. Just after 250 min the pump was reduced to a minimum power such

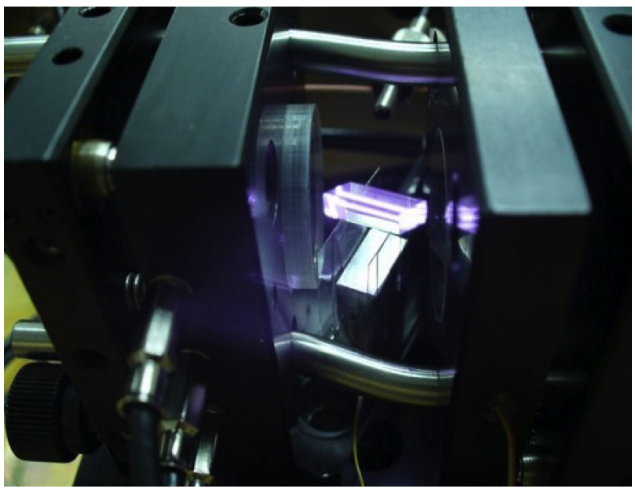

Figure 4.9: Image of the resonant cavity without the clamshell. Unlike Fig. 4.4 the image was taken without any lens filter so it is dominated by the purplish looking IR fluorescence.

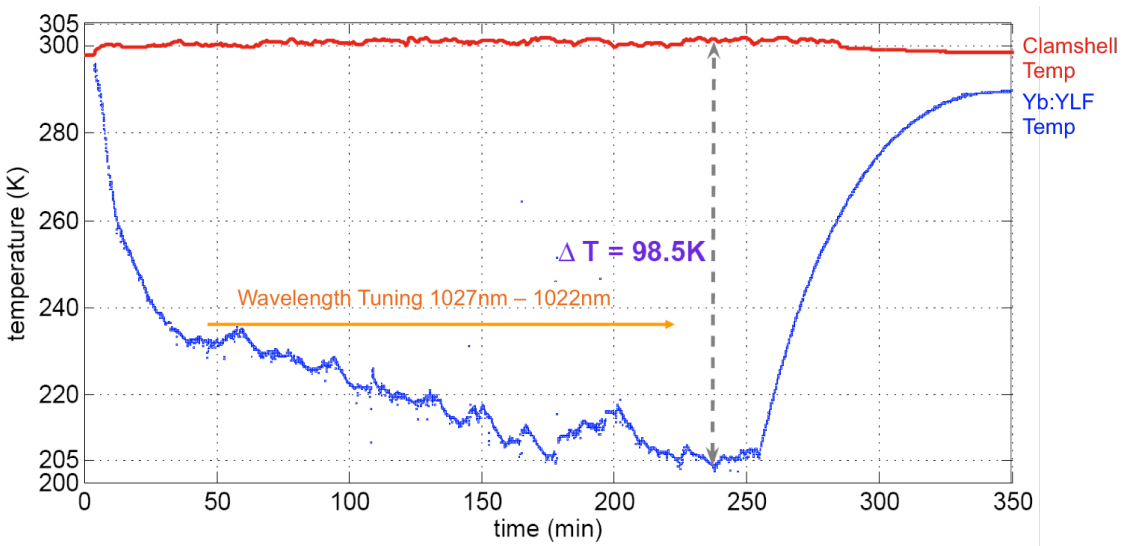


Figure 4.10: Experimental results using a resonant cavity. This is also the first result achieving record cooling via optical refrigeration [48]. The blue line is the $Yb^{3+}$:YLF temperature measured by DLT and the red line is the clamshell temperature as measured by a thermocouple.

that the temperature could still be determined through DLT while having a minimal effect on the crystal temperature. This accounts for the 10 K offset at 350min. Even though RCE absorption is near unity, laser instabilities prevented the ability to stay on resonance by longitudinal mode hopping. The instabilities are the result of feedback, even though two faraday isolators are in place. When resonance is lost, rapid heating is observed followed by gradual cooling once it is regained. Because laser instabilities inhibited further cooling through random loss of resonance and impedance matching was not optimized for 1023 nm, a non-resonant cavity design was utilized to push cooling to the next level.

### 4.3.3 Non-resonant cavity

Non-resonant trapping is maximized by passing pump light through the crystal as many times as possible through a succession of bounces. Some non-resonant trapping schemes which have been proposed and used include the monolithic optical maze (MOM) [16] or dielectric mirrors deposited directly to the cooling sample with a small hole in the input mirror to inject the laser [50], Fig. 4.11. The directly deposited

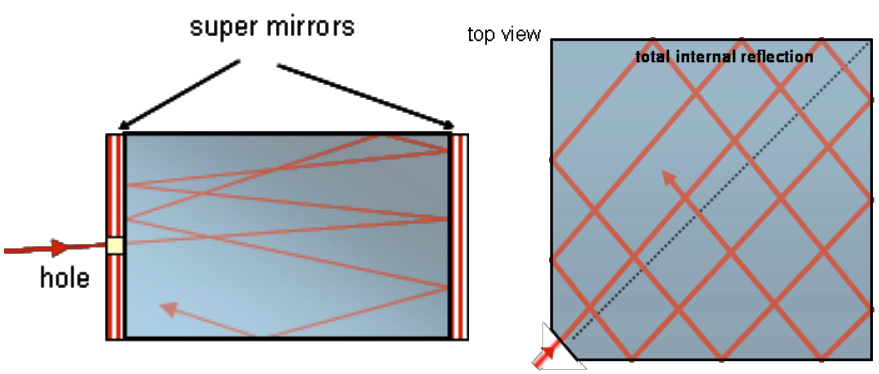


Figure 4.11: Two types of previously used non-resonant cavities. On the left, is a sample with the mirrors directly deposited and on the right is the monolithic optical maze (MOM).

dielectric mirrors provided cooling to 208K (Yb:ZBLAN, [14]), but an improvement is to remove the mirrors from the sample. At the high powers (>10 W) necessary for cooling, heating in the mirrors becomes problematic. Since the mirrors are in contact with the sample directly, there is direct heating where the mirror meets the sample.

Instead, a non-resonant trapping scheme using two high reflectivity mirrors which do no contact the sample was implemented [17], Fig. 4.12. The high reflectivity input

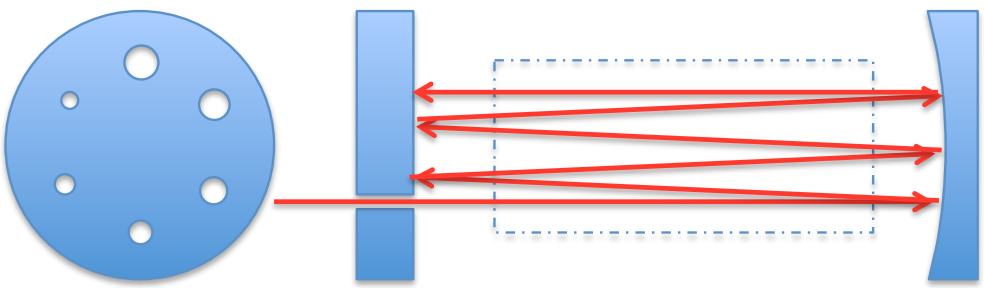

Figure 4.12: On the left is the front view of the input mirror. On the right, the sample lies between the mirrors in a non-resonant orientation.

mirror (R>99.9%) contains several holes of various diameters, with centers placed radially equidistant from the center of the mirror so that the optimal size can be chosen simply by rotating the mirror in-situ. The holes range in size from 1mm to 300$\mu$m. The high reflectivity back reflecting mirror (99.9% reflectivity) is curved (R=15cm) to create a stable non-resonant cavity and is externally mode-match with a pair of lenses to match the beam waist ($w_0$ <150 $\mu$m) at the input mirror and the curvature of the back reflecting mirror. 30 round-trips with an empty cavity have been achieved, Fig. 4.13. Unfortunately, the diameter of the mode-ring of reflections when getting 60 passes is $\sim$ 3 mm which is larger than the cross sectional area of the crystal (3 mm $\times$ 1 mm). Because of this constraint, the cavity is slightly misaligned resulting in $<$ 10 passes which are possible through the crystal. Also, when aligning the cavity with the crystal in place, each pass is partially absorbed which makes it

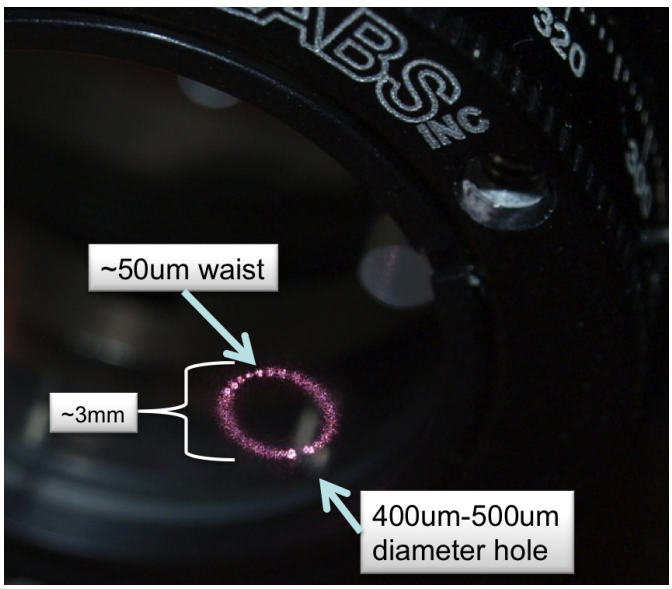


Figure 4.13: Image of the flat mirror in a non-resonant cavity. In view are a few of the input holes as well as a ring of reflections forming a stable non-resonant cavity mode. Each point in the ring corresponds to 2 passes, and 30 points can be seen. The diameter of the ring is $\sim 3mm$.

increasingly difficult to align for a high number of passes. The strong advantage of a non-resonant cavity is the insensitivity to laser longitudinal-mode instabilities, but the disadvantage is unity absorption is not possible.

### 4.3.4 Non-resonant cavity experimental results with ELS laser

The experimental setup is shown in Fig. 4.14 where the pump is the same ELS Versadisk, $Yb^{3+}$YAG thin disk laser tunable from 1020 nm-1040 nm, isolated from the chamber with 2 Faraday rotators (60 dB combined rejection), and mode matched with a pair of lenses, again pumping sample #1 from the University of Pisa. Because maintaining resonance no longer matters, the 3-axis piezo controller as well as the

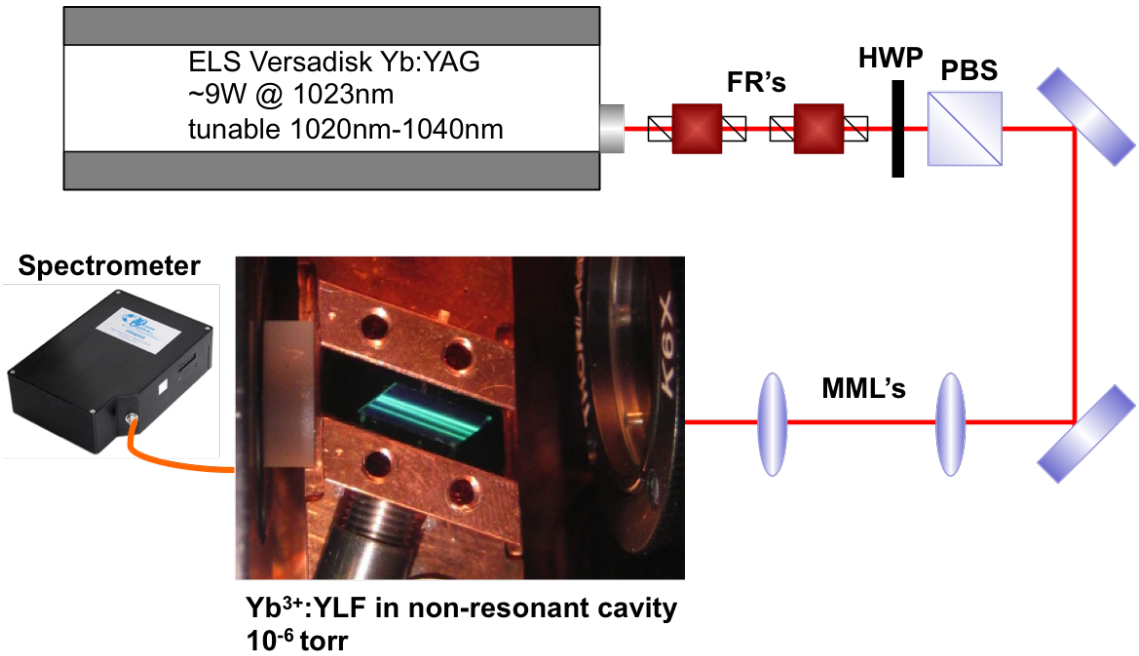


Figure 4.14: Experimental setup for the non-resonant cavity.

Fabry-Perot monitoring cavity can be removed. The laser is again tuned toward the E4-E5 transition where the maximum cooling is expected, resulting in 9 W of power at 1023 nm. Fig. 4.15 shows the results of the non-resonant temperature change as a function of time. At first glance it is obvious that the temperature fluctuations present in the resonant cavity have disappeared, no doubt due to stability. A maximum of 3.5 W absorbed power, with $\sim$ 8 passes, was achieved at 1023 nm which resulted in cooling to 155 K in a single stage with an estimated 90 mW of cooling power, surpassing the performance of standard multistage TEC's. This result was first result reaching cryogenic temperatures via optical refrigeration and was the coldest temperature achieved without the use of mechanical refrigerators or liquid cryogens. Unfortunately being restricted by tunability and pump power meant the MAT could not be reached for this crystal.

Even though it is possible to achieve perfect absorption with a resonant cavity,

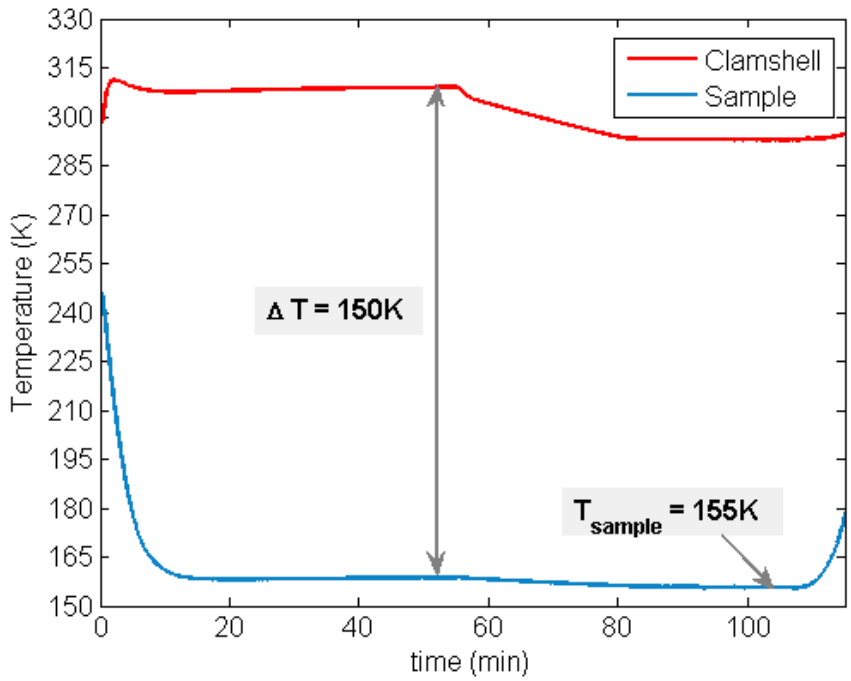


Figure 4.15: This graph shows the experimental results for the non-resonant cooling. Blue is the $Yb^{3+}$:YLF and red is the clamshell temperature as a function of time.

greater cooling is currently measured using the non-resonant cavity. A non-resonant cavity is more stable, being insensitive to sudden changes exhibited by the pump.

Finally is a discussion regarding the results obtained via the non-resonant cavity. A series of measurements were taken by varying the pump power at different wavelengths and plotting the temperature obtained with the absorbed power. Looking back at Fig. 3.23, MAT for 1023 nm is closer to 130 K, given enough absorbed power. Fig. 4.16 shows the amount of cooling observed for various amounts of absorbed power for both 1030 nm and 1023 nm, represented by circles, as well as the predicted values for 1030 nm, 1023 nm and 1020 nm from Ch. 3 assuming dominant radiative load scaling with the sample temperature. There is strong agreement between the measured and expected values, once again reaffirming the radiative load

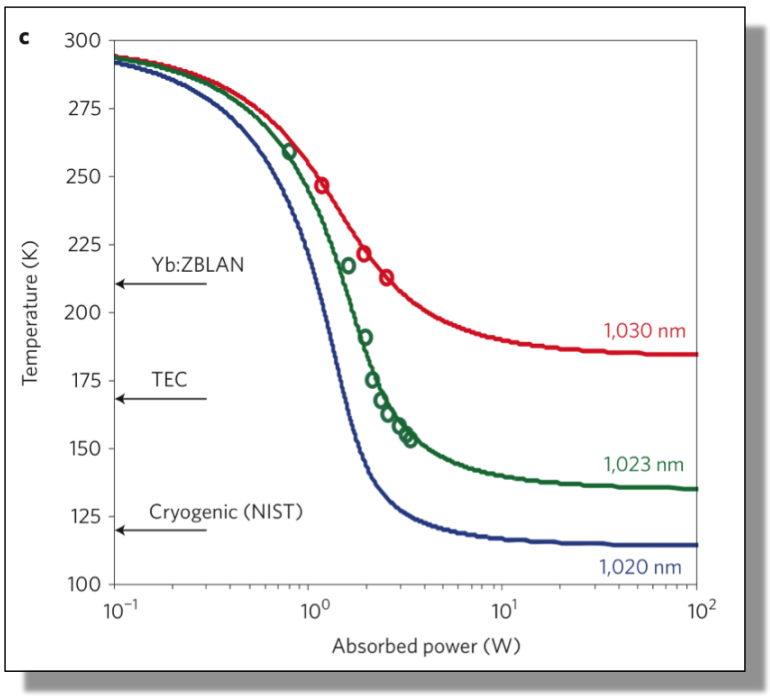


Figure 4.16: Plotted is cooling with absorbed power in colored lines for the given wavelengths, and the measured temperatures using circles. Very good agreement between theory and experimental results is apparent. The three arrows represent the previous record in $Yb^{3+}$ZBLAN, the lowest temperatures accessible by standard TEC's and the NIST defined cryogenic temperature [25].

is dominant. It is important to note the observed saturation of cooling verses the absorbed power as the MAT condition is approached. While currently limited by absorbed power, the fit shows saturation temperatures (e.g. 130 K at 1023 nm) corresponding to MAT values in Ch. 3. Also to note is the predicted saturation at 1020 nm corresponding to MAT of 110 K. This lends confidence that bulk cooling below the NIST defined cryogenic temperature of 123 K is possible with 10 W of absorbed power for the given thermal load management. It also highlights the need for a new pump source at 1020 nm.

### 4.3.5 Non-resonant cavity experimental results with IPG Photonics fiber laser

Knowing the optimal wavelength corresponds to the E4-E5 transition for the Ytterbium ion in $Yb^{3+}$:YLF, it was necessary to acquire a high power pump source at 1020 nm. IPG Photonics was contracted to develop a custom made Yb-doped fiber laser with specifications outlined in Appendix C, Table C.1. The newly developed laser produces >55 W with slight detuning to 1020.7±0.25 nm at high power.

Experiments were performed on three unique Brewster cut $Yb^{3+}$:YLF crystals, two 5% wt. $Yb^{3+}$:YLF crystals grown at the University of Pisa, Samples #1 and #3, and the Brewster cut 10% wt. $Yb^{3+}$:YLF crystal grown by AC Materials in Tarpon Springs, FL. The experimental setup is similar to the previous non-resonant cavity setup (Sec. 4.3.5) except for the pump source. The first 5% wt. $Yb^{3+}$:YLF sample

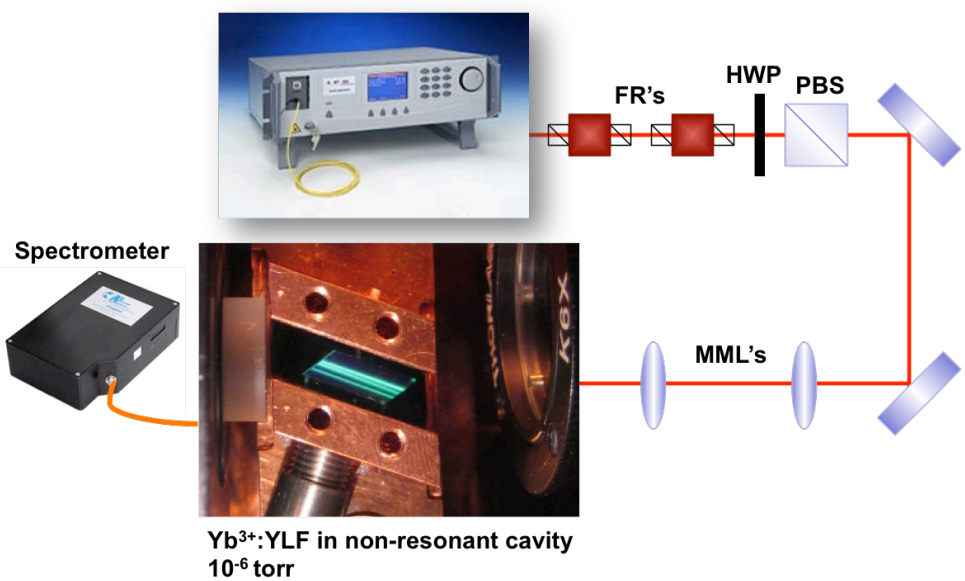


Figure 4.17: Non-resonant cavity setup using the IPG fiber laser.

(denoted sample A) corresponds to sample #1 from the University of Pisa, and is the

same as the previous ELS experiments with a background absorption of $4.0(\pm 0.2) \times 10^{-4}\text{cm}^{-1}$. Because of the relatively short length, L= 6mm, of the first crystal due to successive re-polishing to resurface chips created from years of handling, a second sample (sample B) corresponding to sample #3 from the University of Pisa, with length L= 12mm was used which has a background absorption of $4.4(\pm 0.2) \times 10^{-4}\text{cm}^{-1}$. With a slightly higher background absorption, MAT rises to 116K. Sample B has less surface problems and can therefore accommodate ∼12 passes compared to the 6 available for the first sample, increasing the absorbed power through an increase of 4× the effective length (NL). The third sample (sample C) corresponding to the 10% Brewster cut $Yb^{3+}$:YLF crystal from AC Materials, also with length L= 12 mm, has a background absorption of $2.0(\pm 0.2) \times 10^{-4}$ cm$^{-1}$. This sample not only accommodates 12 passes with a relatively long length, but also quadruples the absorption efficiency ratio in Eq. 3.15. It should be understood however that as the surface area of the crystal increases, so does the radiative heat load (Eq. 2.25). The specific results for each crystal are described under respective sample letters. As long as the ambient heat load is minimized while the absorbed power is maximized, temperatures approaching MAT should be realized.

**Sample A**

Sample characteristics are measured using the techniques of Ch. 3 resulting in $\eta_{eqe} = 99.5 \pm 0.1\%$ and $\alpha_b = 4(\pm 0.2) \times 10^{-4} cm^{-1}$ (Fig. 3.15). This leads to MAT of 110 K at 1020 nm which was experimentally verified locally with results presented in the following chapter, Ch. 5.3. The resulting power cooling experiment is shown in Fig. 4.18. After adjusting the power for optimal cooling, a temperature of ∼ 137 K was reached, 27 K above MAT for the measured characteristics. Power adjustments were necessary due to thermal blooming caused by the faraday isolators with ∼48 W being optimal in this case. In order to achieve lower temperatures, it is necessary to increase the cooling power for the given heat load. Because of the physical constraints

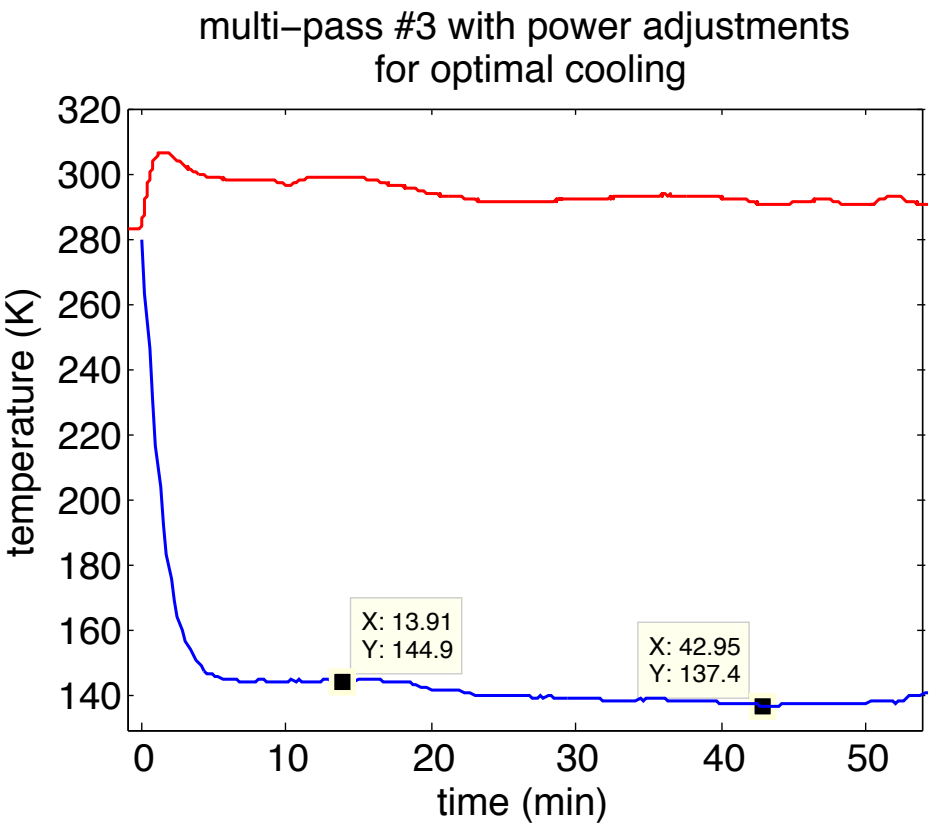


Figure 4.18: Sample A non-resonant cavity cooling results with the IPG laser. Fluctuations in both clamshell and crystal temperatures are due to incident power adjustments to find optimal cooling.

of this particular crystal, i.e. relatively short length (6 mm) and narrow cross section window allowing for only 6 passes, a second 5% wt. $Yb^{3+}$:YLF crystal was used.

**Sample B**

The second 5% wt. $Yb^{3+}$:YLF crystal has a higher background absorption which can be seen by the long wavelength zero crossing at 1060 nm in Fig. 4.19 (compared with Fig. 3.15). Sample A exhibited slight cooling at 1060 nm, while sample B shows neither heating or cooling, i.e. break even. The consequence of slightly higher background absorption is a MAT of 116 K. Accounting for a slight detuning at

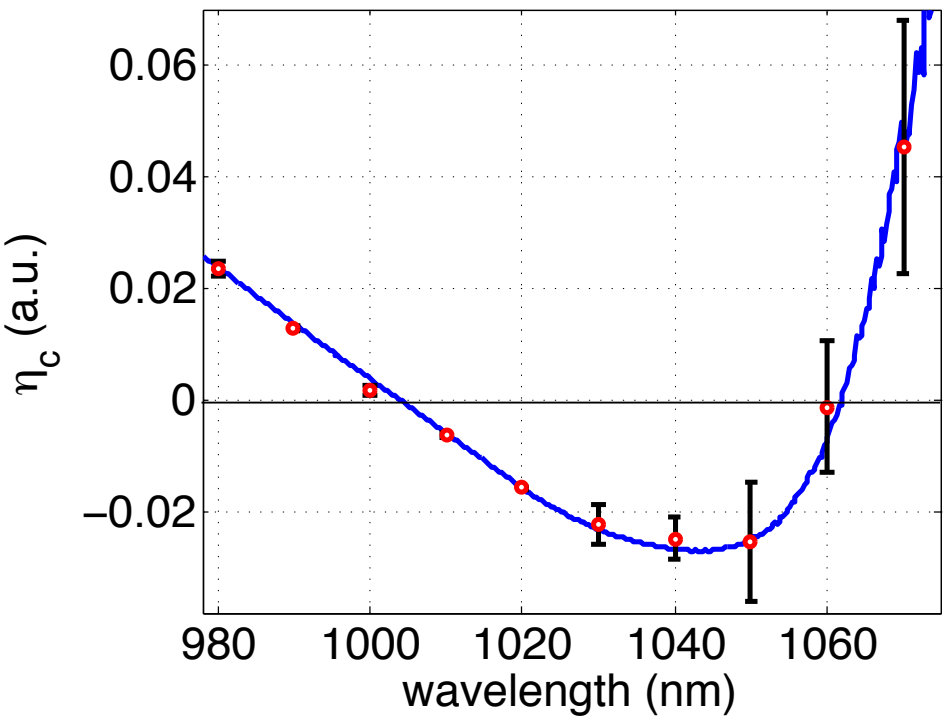


Figure 4.19: Experimental measurement (red circles with error bars) and fit (blue) where $\eta_{ext} = 99.5 \pm 0.1\%$ and $\alpha_b = 4.4 \pm 0.2 \times 10^{-4} cm^{-1}$.

high power to 1020.7±0.25 nm of the pump, MAT becomes ∼118 K. Since the NIST defined cryogenic temperature of 123 K is achievable for this crystal, two experiments were performed.

The first experiment utilizes 12 passes irradiated with ∼45 W of pump power, maintaining the clamshell near room temperature. The result is a final temperature of ∼123 K (Fig. 4.20) with ∼162 K temperature difference between the sample and the clamshell enclosure. With ∼18 W of absorbed power, the cooling power at 123.7 K and 1020 nm is estimated at 50 mW, which is consistent with previous cooling power estimations. Within the experimental uncertainty, this is the first demonstration where a solid has been optically cooled to NIST defined cryogenic temperatures. Importantly, this has been accomplished all solid-state, where the crystal received

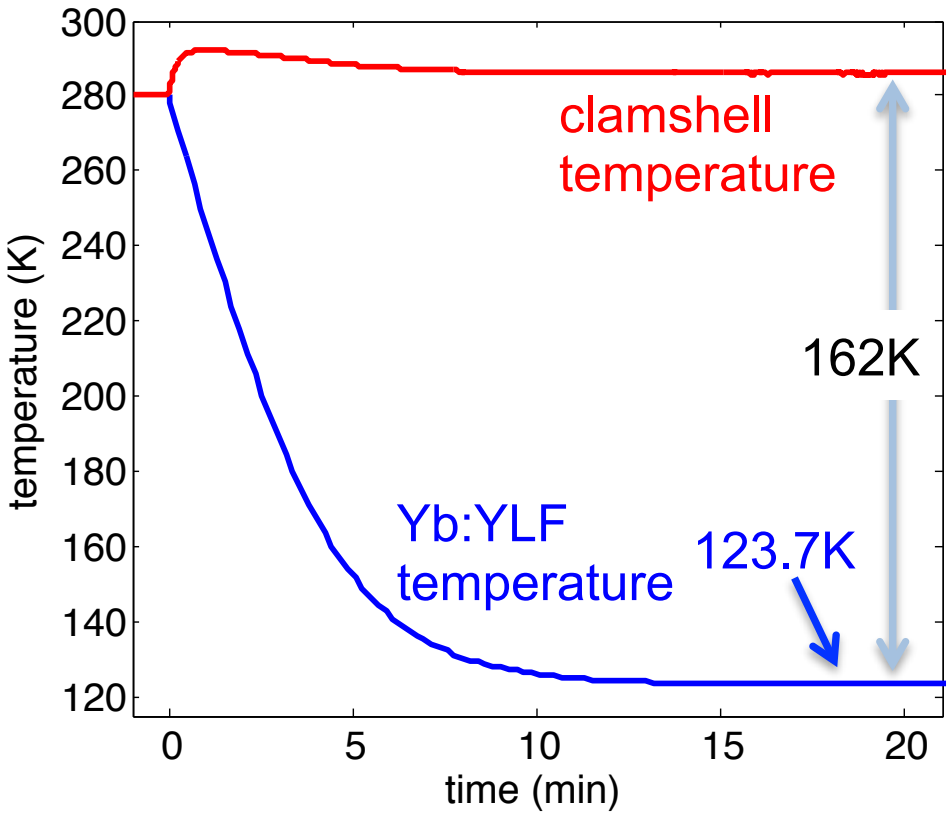


Figure 4.20: Sample B non-resonant cavity results.

no direct cooling through cryogenic liquids or mechanical refrigerators.

Because the MAT condition was not met, a power scaling study of the steady-state temperatures, like that in Sec. 4.3.4, was performed and fit assuming a dominant radiative load. Since sample B is twice as long, the surface area increases and with it the radiative heat load and the necessary increase in absorbed power. The condition of equilibrium (or steady-state) in the cooling dynamics is reached when the cooling power $P_{cool}$ becomes equal to the load power $P_{load}$ on the sample at a temperature $T_{eq}$. For the dominant radiative load, this condition is given by:

$$\eta_c(\lambda, T) P_{abs}(\lambda, T) = \kappa \left(T_c^4 - T_{eq}^4\right) \tag{4.14}$$

where $P_{abs}$ is the absorbed power, $\kappa$ is a proportionality constant given by the product

of a Stefan-Boltzmann constant and a geometry- and emissivity-dependent coefficient (see Eq. 4.4), and $T_c$ is the temperature of the clamshell. The data of Fig. 4.21 (black) is fit by a solid line, using Eq. 4.14 and $\eta_c$ values from the spectroscopic measurements described above. Very good agreement is found between the measurements and the data-assisted model. In particular, the expected asymptotic behavior of the measured temperature with increasing absorbed power, approaching the MAT value of 118 K, is clearly observed.

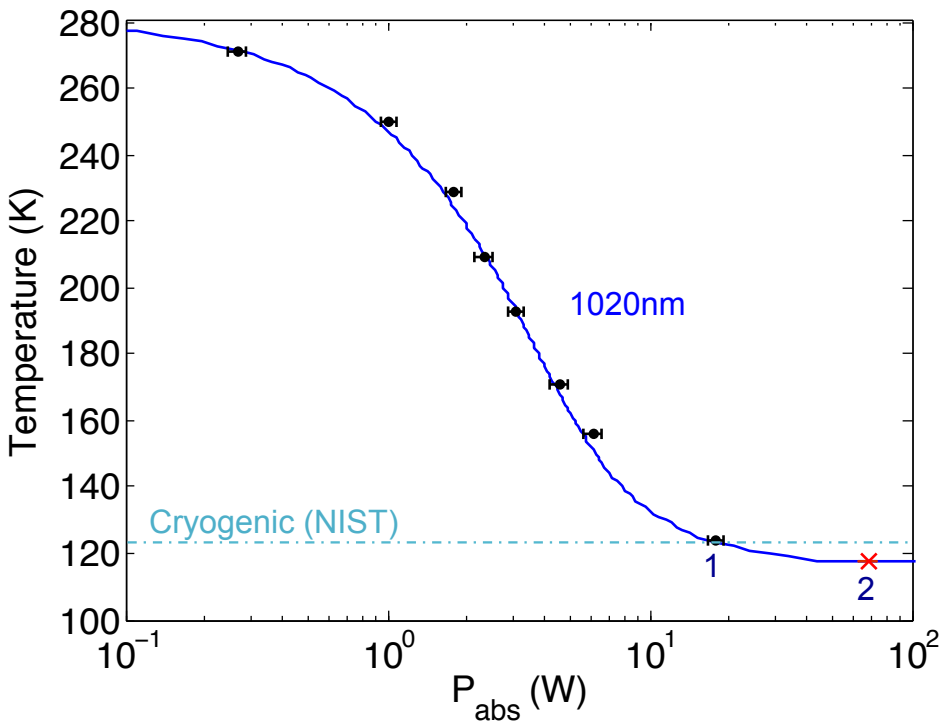


Figure 4.21: Steady state temperature scaling with the absorbed power (black), model prediction (blue line) and lowest temperature achieved by effective scaling of the absorbed power (red "x").

In a second experiment, to reach temperatures even closer to the MAT value, either a further increase in absorbed power $P_{abs}$, or, equivalently, a decrease in the parasitic load ($P_{load}$), is required (Eq. 4.14). For the proof of principle and using

the latter approach, we modified the water chiller feedthrough to accept liquid nitrogen, which was used to reduce the clamshell temperature $T_c$. It is important to understand that only the clamshell is cooled with $LN_2$, NOT the crystal, and it is only reduced to 208 K which is still far above the final temperature of the crystal. The result of reducing the clamshell temperature can be seen in Fig. 4.22 where the

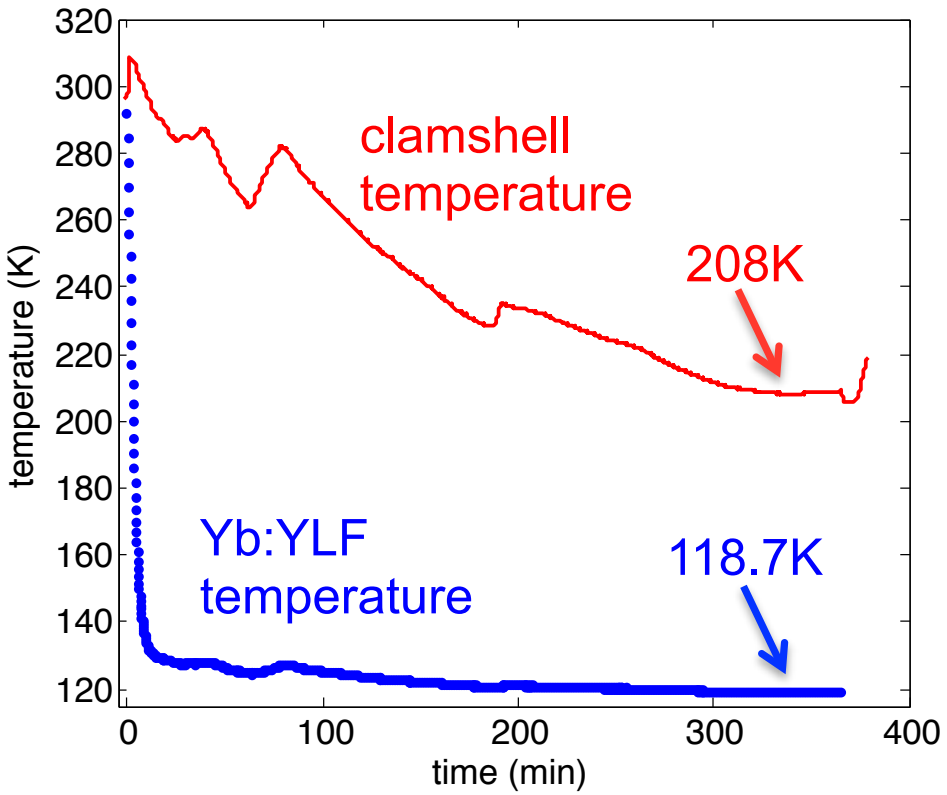


Figure 4.22: Sample B non-resonant cavity results with reduced ambient heat load.

crystal temperature reached a new steady state temperature of 118.7±1 K. Within the uncertainty of our measurements, MAT for this sample has been obtained. The new steady-state temperature can be projected onto the data set obtained with the old $T_c$ value of 285 K (Fig. 4.21). For that, we estimate a factor of ~3.8 reduction of the thermal load on the sample, when going from the old to the new value of the $T_c$. This factor is given by the corresponding ratio of the heat loads ($285^4$ - $123.7^4$)/($208^4$

- $123.7^4$), as per Eq. 4.14. This reduction of the heat load is equivalent to an effective increase of the absorbed power by the same factor, if the sample and clamshell temperatures were 123.7 K and 285 K, respectively. Thus, the final temperature of 118.7 K can also be reached with an effective increase of the absorbed power by a factor $\sim 3.4$, the value lowered from the initial 3.8 estimate by the reduction of the absorption coefficient at the corresponding temperatures. This allows us to project the point of cooling to 118.7 K onto Fig. 4.21, indicated by the "x", which is in a very good agreement with the model prediction. The estimated cooling power is 18 mW which is a direct consequence of approaching the MAT condition where the cooling efficiency approaches zero. As a comparison, ∼630 mW of cooling power is available at room temperature. This experiment verifies the MAT condition for an optically cooled sample and demonstrates the coldest temperature reached by a 5% wt. $Yb^{3+}$:YLF crystal.

**Sample C**

The final sample revealed in this chapter is a 10% wt. $Yb^{3+}$:YLF sample grown by AC Materials in Tarpon Springs, FL. This sample is part of a doping study as well as a trace element analysis study described in Ch. 6. The doping study analyzes samples grown under the same conditions and the same starting materials with the exception of increased Yb-doping with the goal of increasing the absorption efficiency, $\eta_{abs}$. Five samples were grown consisting of un-doped YLF, 1% wt. $Yb^{3+}$:YLF, 5% wt. $Yb^{3+}$:YLF, 7% wt. $Yb^{3+}$:YLF, and 10% wt. $Yb^{3+}$:YLF. Repeating the methods of Ch. 3, analysis of the cooling efficiency of each sample was performed and is shown in Fig. 4.23, where the 10% wt. $Yb^{3+}$:YLF crystal (blue) shows the best performance with $\eta_{ext} = 99.6(\pm 0.1)\%$ and $\alpha_b = 2.0(\pm 0.2) \times 10^{-4}$ cm$^{-1}$. The high energy zero crossing shift with increased doping is a direct consequence of reabsorption red shifting the mean luminescence. While the external quantum efficiency remains the same, reducing the reabsorption path length (i.e. reducing the crystal dimensions)

will improve cooling efficiency. Re-writing Eq. 3.15 here for convenience,

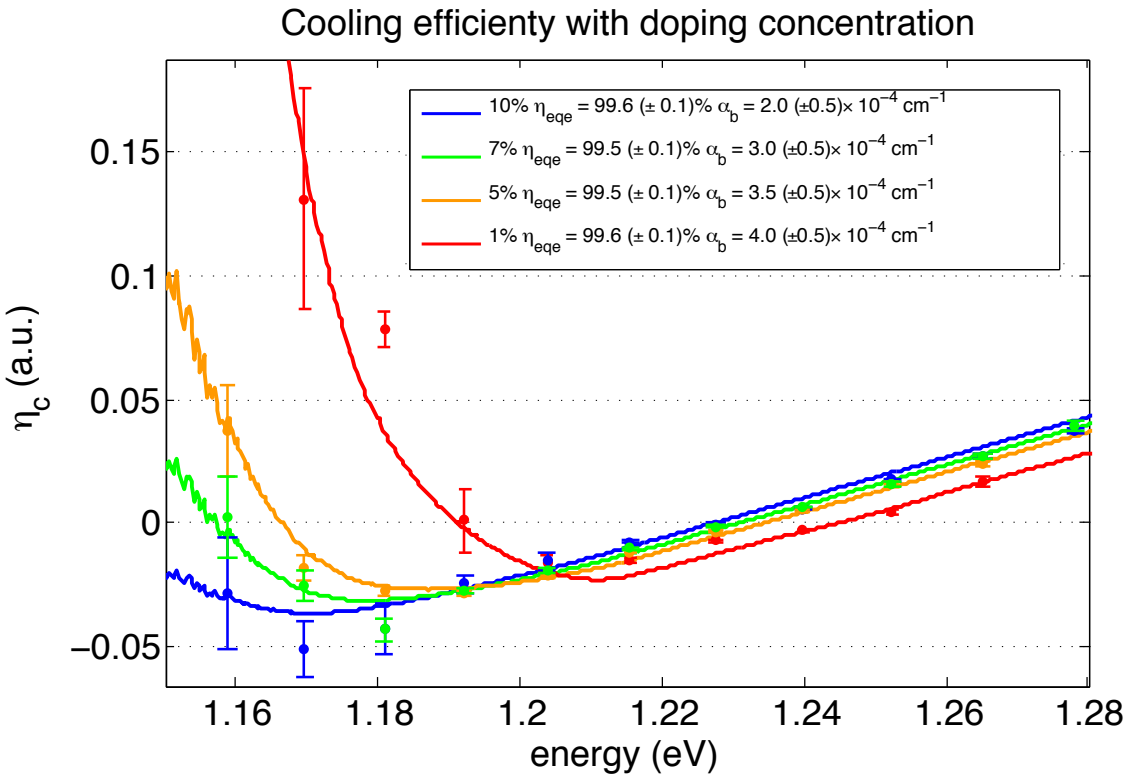


Figure 4.23: Measured values of the cooling efficiency with error bars fit by the theory for 1% (red), 5% (orange), 7% (green), and 10% (blue) samples grown by AC Materials.

$$\eta_{abs} = \frac{1}{1 + \alpha_b/\alpha_r(\lambda, T)}, \tag{4.15}$$

it can be quickly seen that the 10% wt. $Yb^{3+}$:YLF crystal increases the ratio in the absorption efficiency by 4× through a doubling of the resonant absorption and halving the background absorption as compared to the previous best performing 5% wt. $Yb^{3+}$:YLF crystal with $\alpha_b = 4.0(\pm 0.2) \times 10^{-4}$ $cm^{-1}$. With this information, a the map of the temperature and wavelength dependent cooling efficiency is generated and replotted here, providing the MAT characteristics for this sample with a global minimum (gMAT) of ∼93 K at 1020 nm. With this improvement, it is clear opti-

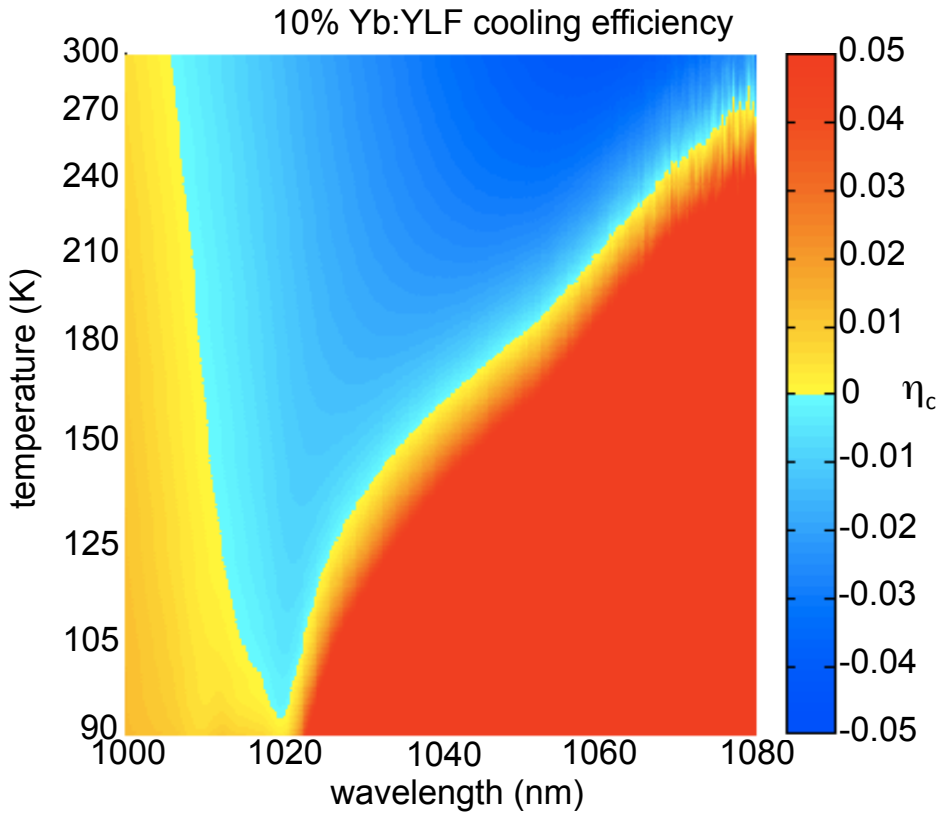


Figure 4.24: Temperature and wavelength dependent cooling efficiency for the 10% wt. $Yb^{3+}$:YLF. Blue regions denote cooling, while red regions denote heating. The line separating the region of cooling from heating is the spectroscopic minimum achievable temperature (sMAT) with a global minimum (gMAT) at ∼93 K.

cal refrigeration is moving toward the next major goal of achieving liquid nitrogen temperatures.

The cooling performance was tested for a Brewster cut 10% wt. $Yb^{3+}$:YLF crystal with dimensions ∼11.4 mm × 4 mm × 3 mm. Because of the significant increase in absorption, 90% of the incident laser power is absorbed within 2 passes at room temperature. It is possible with great effort to view 3-4 passes through the crystal with an IR viewer and drastic misalignment, however this poses an experimental problem when attempting to achieve 8 (or more) passes as will be discussed after the

10% wt. $Yb^{3+}$:YLF cooling results. Therefore the experimental setup was modified to provide a Ti:Sapphire guide laser, Fig. 4.25, that is tuned to a region of low absorption in the crystal and co-propagating with the IPG pump. It was ensured that the guide and the pump laser continued co-propagating >1 m beyond the vacuum chamber.

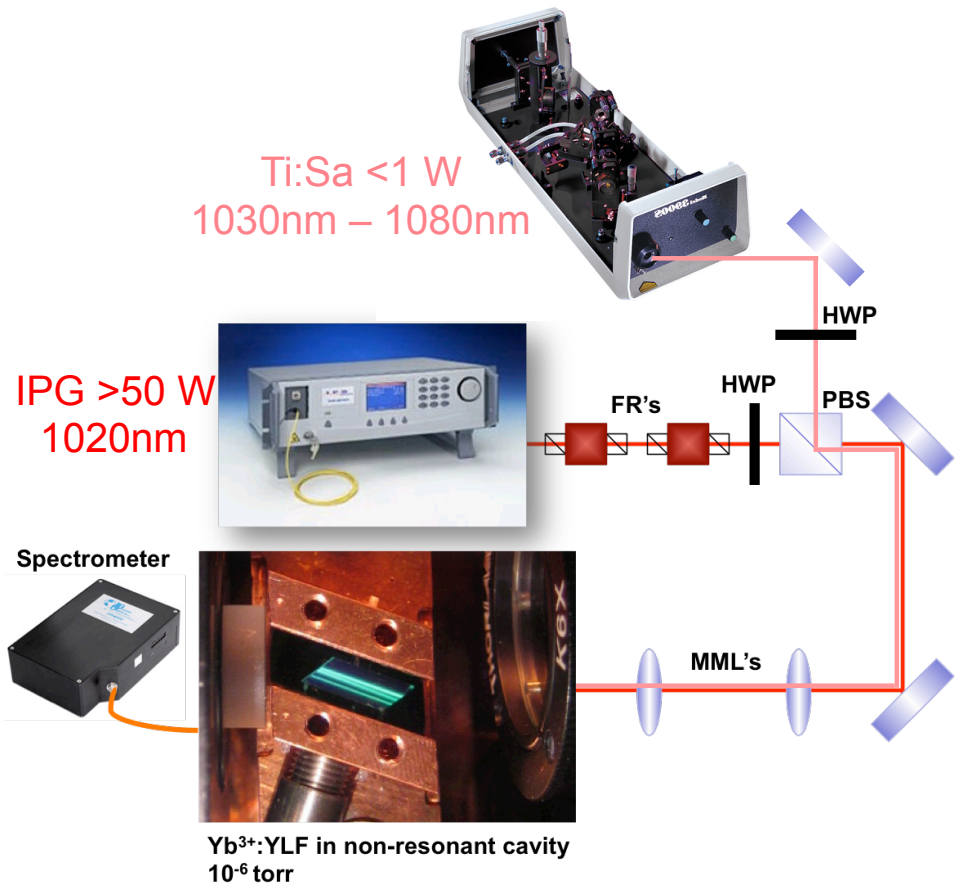


Figure 4.25: Experimental setup for the 10% wt. $Yb^{3+}$:YLF crystal accommodating for the alignment issues due to high absorption at room temperature with a Ti:Sapphire guide laser.

With 8 passes through the 10% wt. $Yb^{3+}$:YLF crystal and an incident pump power of 45 W, a minimum temperature of ~114 K was achieved while maintaining

the clamshell at 299 K as seen in Fig. 4.26. Clearly MAT has not been achieved for

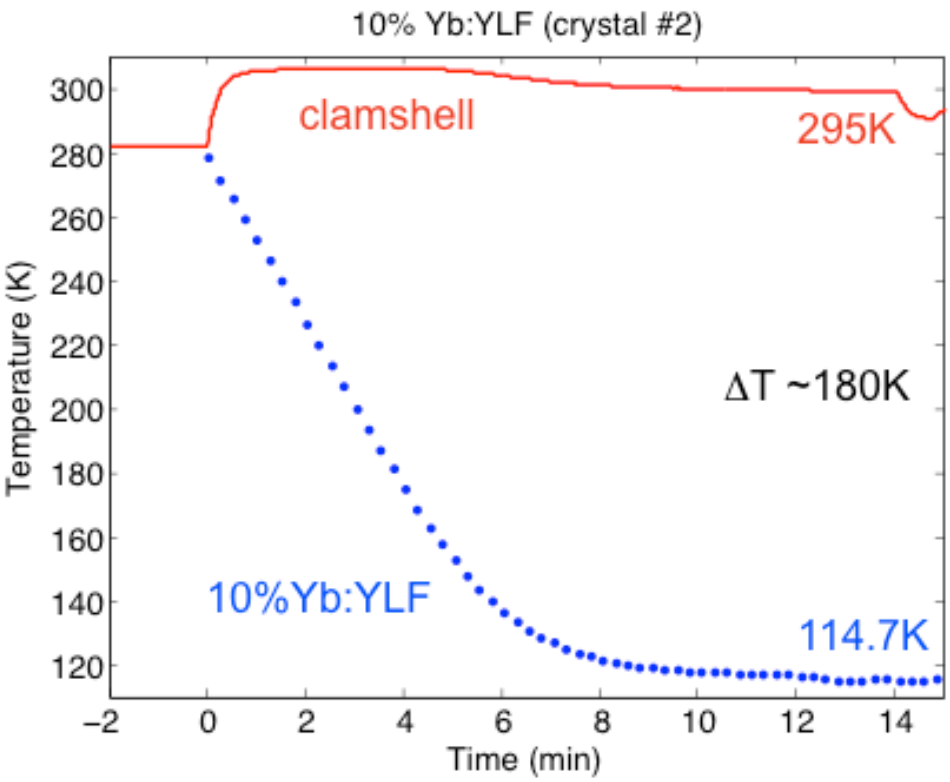


Figure 4.26: Cooling of the 10% wt. $Yb^{3+}$:YLF crystal with 45 W of incident power. Temperature reaches down to ∼114 K from room temperature while maintaining the clamshell at 299 K.

this crystal, yet. This is due to the significant increase in clamshell temperature. Because of the increased absorption afforded by the 10% doping, ∼25 W of pump light is absorbed generating intense fluorescence, heating the clamshell. By reducing the clamshell temperature through better that load management, the MAT condition can be achieved.

Earlier a problem was mentioned caused by the high absorption in the 10% $Yb^{3+}$:YLF crystal. While it is possible to achieve ∼10 passes, those passes beyond the fourth cannot be viewed at room temperature. At low temperatures, absorption

decreases significantly allowing for successive passes to achieve higher incident power. The problem this supplies is that it remains difficult to ensure the remaining pump power at low temperatures exits the non-resonant cavity as the absorption decreases. With ∼45 W incident at 300 K, essentially all of the pump can be absorbed, while at 114 K only about half is absorbed and therefore >20 W needs to exit the system. Failure to couple out all of the light can lead to greater radiative heat load generation when reflections are absorbed in the clamshell or optical mounts, preventing the crystal from reaching low temperatures.

Of greater concern is when reflections are absorbed in the Maxorb of the clamshell which lies <1 mm from the surface of the crystal. When the Maxorb layer absorbs reflected pump light, material is ejected from the Maxorb surface which quickly condenses on the surface of the crystal, creating a direct source of heating as fluorescence is absorbed and damaging the applied Maxorb for subsequent experiments. Under the worst conditions, the material can condense on the surface in the path of the incident pump. This only occurred once for a 10% wt. $Yb^{3+}$:YLF Brewster cut crystal with >50 W incident power and resulted in nearly immediate melting of the crystal, Fig. 4.27. More than half of the crystal was melted and had to be broken away

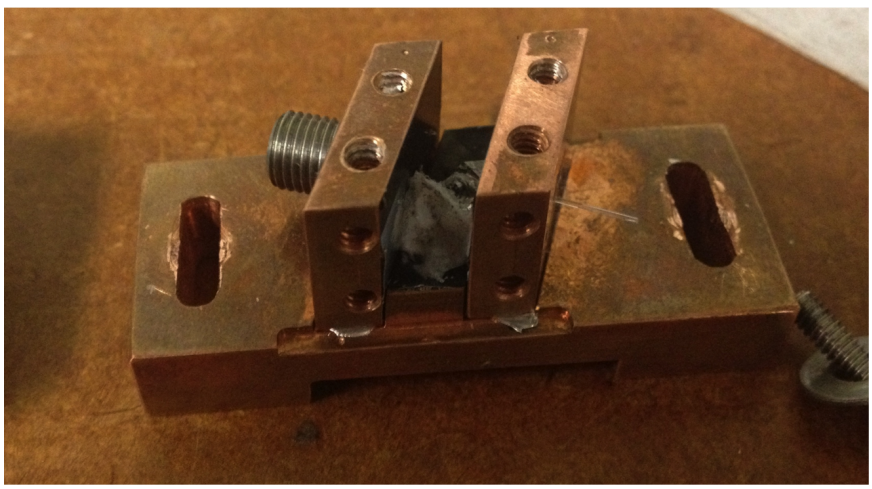

Figure 4.27: Melted 10% wt. $Yb^{3+}$:YLF crystal adhering to the clamshell walls.

from the clamshell walls where it had partially fused. After removing the melted material, it was evident that the black layer of Maxorb had been evaporated from the clamshell face opposite the Brewster face allowing for direct deposition in the path of the pump, thereby causing the full pump power to heat the crystal surface.

The experiments performed in this section have verified the MAT condition for the 5% wt. $Yb^{3+}$:YLF crystals and have shown the coldest temperatures to date by any solid state means, achieving ∼118 K for the 5% $Yb^{3+}$:YLF crystal and ∼114 K for the 10% wt. $Yb^{3+}$:YLF crystal. Further improvements in heat load management will result in temperatures below 100 K. With temperatures below 100 K within reach, it is useful to begin cooling a load to show the practical ability for optical refrigeration to be used in all solid-state cryo-cooling devices..

# Chapter 5

# Cooling a load via Optical Refrigeration

## 5.1 Introduction

The desired use of optical refrigeration is to remove heat from an applied load. Experiments were performed to show the feasibility of practical applications of cooling a load utilizing optical refrigeration while obtaining the coldest temperatures ever achieved using an all solid-state system. Furthermore, a novel local temperature measurement technique was developed to accurately measure the spectroscopic minimum achievable temperature (MAT($\lambda$)) of a 5% wt. $Yb^{3+}$:YLF crystal.

In the first series of experiments we exploit sample #1, a 5% wt. $Yb^{3+}$:YLF from the University of Pisa, in optical refrigeration pumped by the ELS tuned to 1023 nm with ∼9 W of available pump power to cool a load comprised of a GaAs semiconductor passivated by GaInP cladding in a double heterostructure geometry with high external quantum efficiency. The payload is chosen such that the mean luminescence wavelength of the Yb emission is above the band-edge absorption of

GaAs even at room temperature, therefore the payload is optically transparent to the high-power fluorescence and allows for direct contact with the crystal surface. By exploiting the well characterized temperature dependent GaAs band gap [51], the GaAs semiconductor serves two purposes. Firstly (Sec. 5.2) it provides the ability to cool a load while independently verifying the crystal temperature. Secondly (Sec. 5.3), the GaAs provides a local, highly sensitive thermometer to measure the spectroscopic minimum achievable temperature of the 5% wt. $Yb^{3+}$:YLF crystal.

The second series of experiments (Sec. 5.4) utilizes an optically isolating thermal link. A thermal link allows for any device which would otherwise absorb the high-power, heat inducing fluorescence to be optically isolated and cooled through all solid-state means. This required computer aided design and adhesion free bonding of an optically isolating sapphire crystal which was specially cut and polished. Several thermal link designs were analyzed in ZEMAX. Once a satisfactory design was chosen, a handmade thermal link was cut and polished with BK-7 and bonded with UV curable adhesive for verification of the optical isolating properties. After confirmation of the design had taken place, a high thermal conductivity thermal link was cut out of sapphire, diffusion bonded the link to a cooling crystal, and tested.

## 5.2 Cooling a GaAs load

### 5.2.1 Experimental setup to cool a GaAs load

This experiment consists of cooling a GaAs heterostructure disk, acting as a load, bonded to a 5% wt. $Yb^{3+}$:YLF crystal which makes thermal good contact with the crystal by means of a thin high conductivity adhesive layer. The GaAs heterostructure disk has a thickness of 2 $\mu$m with diameter of 0.8 mm corresponding to a weight of 5 micrograms. The temperature of the optical refrigerator and load is deduced by

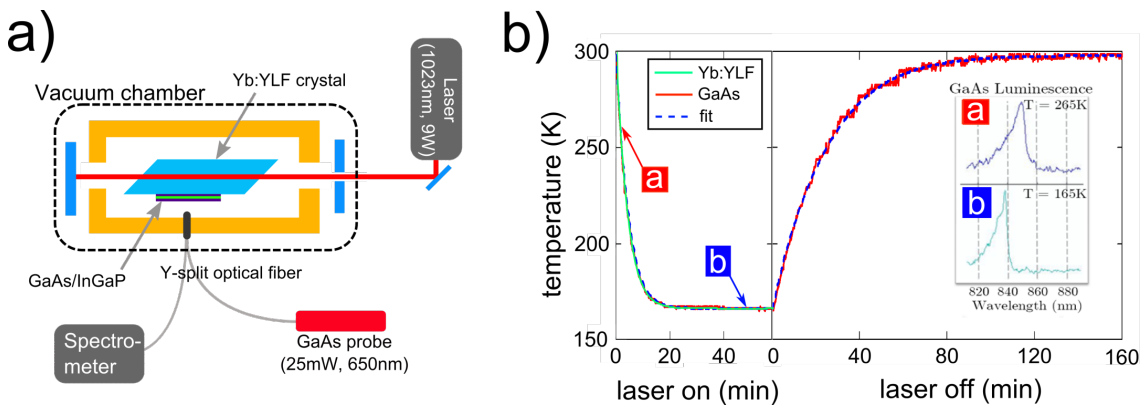


Figure 5.1: (a) Schematic of experimental setup; (b) Temperature of the crystal ($Yb^{3+}$:YLF) and GaAs load as a function of time. High power laser is incident at t = 0 min, following by turn-off at t ∼55min, when steady state was achieved, time is re-zeroed after the laser is turned off. Both $Yb^{3+}$:YLF and GaAs temperatures are deduced by non-contact techniques. The cooling and warming dynamics are fitted with single exponential curves. Inset shows GaAs/InGaP spectra at two corresponding points (a: T = 265K, b: T = 165K).

simultaneously monitoring the fluorescence spectrum of $Yb^{3+}$:YLF and GaAs band-edge emission and performing DLT on the independent spectral regions. Fig. 5.1 outlines the experimental setup, where high power 1023nm 9W Yb:YAG thin-disk laser (ELS) pumps the $Yb^{3+}$:YLF crystal in a non-resonant cavity geometry. Blackbody thermal load is minimized by housing the crystal (with its GaAs load) in the same tightly fit clamshell as Ch. 4.

A y-split optical fiber is fed-through the vacuum chamber in order to collect fluorescence of the $Yb^{3+}$:YLF crystal excited by the pump laser and GaAs luminescence, excited by the weak laser diode (≤5mW) that is coupled at one of the fiber ports on the ambient side. The second port is used to spectrally resolve both emission signals in a spectrometer in real time (Fig. 5.1a). The temperature of the 5% wt. $Yb^{3+}$:YLF is determined by differential luminescence thermometry (DLT) [43], where raw signal is obtained by integrating spectral difference of the two luminescence signals:

at known (reference) and unknown temperatures. The scalar integral value is converted to temperature by means of a separate calibration experiment performed in the optical cryostat with experimental accuracy of ±1 degree [25]. GaAs temperature is deduced from the well-known temperature dependence of the band-gap [51]. In this method temperature accuracy is limited by the wavelength resolution of the spectrometer and is less than 2 degrees at low temperatures.

Cooling of $Yb^{3+}$:YLF with GaAs load is shown in Fig. 5.1b. After nearly 30 minutes of laser irradiation, a steady-state temperature of 165 K is reached by both the cryocooler and the payload. The fact that both cooler and load are at nearly the same temperature proves that no substantial thermal gradient exists between them. The cool-down and warm-up (rise) times are fitted with single exponential curves via least-squares algorithm. As is shown below, these fits provide a straightforward way of estimating the cooling and parasitic load powers in the $Yb^{3+}$:YLF cryocooler.

It should be noted that an earlier attempt at cooling a thermal load using optical refrigeration in Yb-doped ZBLAN glass had resulted in a temperature drop of 12 degrees below ambient [50]. The achieved here temperature of 165 K is colder than the benchmark of standard thermoelectric coolers. Without the load, the bare YLF crystal has cooled to 155 K in a separate experiment [25], Ch. 4 utilizing the ELS laser. As discussed below, this small discrepancy is attributed to increased parasitic absorption due to the adhesive as well as GaAs double heterostructure itself. Cooling the GaAs load was not repeated with the IPG fiber laser, instead the thermal link was utilized (Sec. 5.4).

### 5.2.2 Analysis of the Temperature Dynamics

Under high vacuum ($\leq 10^{-4}$ torr) conditions, the dominant thermal load on the sample is assumed to be radiative or black-body (BB), and from the 6 fiber supports

that hold the sample in place within the chamber. Due to high thermal conductivity of the YLF crystal, the sample reaches a uniform temperature within a second or so. We, therefore, ignore the initial dynamics and consider temperature evolution of the whole sample at larger time scales determined by the aforementioned thermal loads (Ch. 2), rewritten from Eq. 2.23, as given by:

$$C(T)\frac{dT}{dt} = \eta_c P_{abs} + A_s\kappa_h(T_c - T) + \frac{N\kappa_L(T)A_L}{d_L}(T_c - T) + \frac{\varepsilon_s A_s \sigma}{1+\chi}(T_c^4 - T^4). \quad (5.1)$$

Here $C = \rho c_v V_s$ is the heat capacity of the cooling sample (YLF ) in terms of its density ($\rho$), specific heat ($c_v$(T)), and volume $V_s$. The first term in the right hand side of Eq. 5.1 is the driving term which is the total cooling power in terms of cooling efficiency and the absorbed laser power, both varying with wavelength and temperature. The second term accounts for the thermal conductivity through the N fiber support links each having area $A_L$, length $d_L$, and thermal conductivity $\kappa_L$. The last term on the right is the black-body radiation load with $\sigma$ denoting Stefan-Boltzmann constant (=5.67×10$^{-8}$ $\frac{W}{m^2K^4}$). This radiative load is lowered by using the low thermal emissivity coating on the chamber walls by a factor of $1+\chi$ where $\chi = (1-\epsilon_c)\frac{\epsilon_s A_s}{\epsilon_c A_c}$, with $\epsilon_j$ and $A_j (j = s, c)$ denoting the thermal emissivity and the area of the sample and chamber respectively.

Once the Debye temperature of the $Yb^{3+}$:YLF is fixed [52], the only free parameters describing the temperature dynamics are the warm-up time-constant,

$$\tau_L = \frac{Cd_L}{N\kappa_L A_L}, \quad (5.2)$$

and factor $\chi$. Due to non-trivial temperature dependent coefficients, we fit Eq. 5.1 numerically to obtain cooling (with the driving term) and warm-up (no driving term) dynamics. By fitting the temperature evolution in the warm-up regime, parasitic loads can be estimated without having to include the cooling power dynamics itself. This fit yields $\tau_L \approx 800$ min and $\chi = 2.1$, for $A_s \approx 1.5$ cm$^2$, $\epsilon_s \approx 0.8$, $\rho c_v(YLF) \approx 3\frac{J}{Kcm^3}$ (at 300 K) and $V_s = 0.3 \times 0.3 \times 1 \approx 0.1$ cm$^3$. The fact that $\tau_L$ is much longer

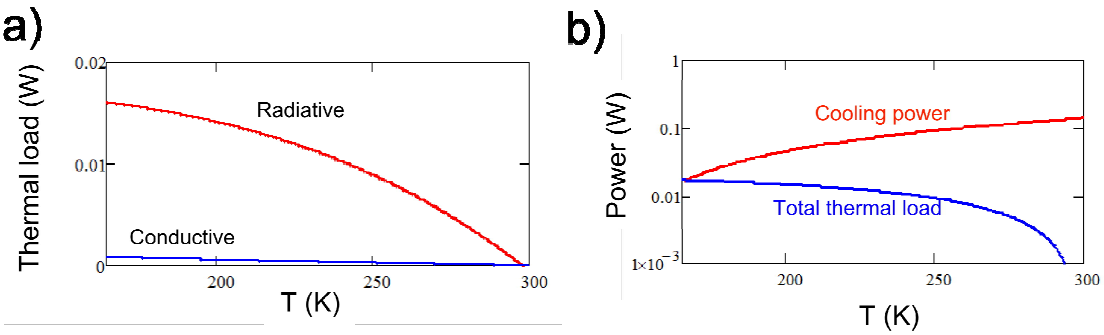


Figure 5.2: (a) Comparison of temperature-dependent radiative and conductive thermal loads, as obtained from fitting the warm-up dynamics seen in Fig. 5.1; (b) Comparison of cooling and total thermal load powers in the current $Yb^{3+}$:YLF cryocooler, as estimated from the fits of full dynamics (Fig. 5.1): at T = 300K, cooling power of 150mW is available, diminishing to a stready-state value of 20 mW at T = 165 K.

than the time scale of the experiment suggests the black-body is the dominant load on the sample (Fig. 5.2a), consistent with the earlier findings [25] and further supported by additional experiment where removal of the two (out of the six) support fibers did not change the final temperature achieved. The $\chi$ parameter is lower than previous estimates [14], suggesting the need to improve the low thermal emissivity coating characteristics.

The temperature dependence of the cooling power (driving term) is also determined directly from the fits. At room temperature a cooling power of 150 mW is available for the given pumping conditions. The cooling power diminishes as temperature is decreased, reaching a balance with the parasitic load (steady-state) at T = 165 K, with the cooling power of 20 mW (Fig. 5.2b). It should be noted that the temperature dependence of the cooling power can also be estimated from the known cooling efficiency (Eq. 2.17) and the absorbed power [25]. At ambient we obtain $P_{cool}$ = 140 mW, in good agreement with the fitting results. At low temperature however we obtain agreement with the temperature dynamics only if we increase

the background absorption by factor of 4 (Eq. 2.17). We attribute such increase due to the parasitic absorption in the material of the load as well as the adhesive used for attachment. Finally, we note that GaAs absorption spectrally overlaps with the upconverted emission due to other rare-earth species in the $Yb^{3+}$:YLF crystal, specifically $Er^{3+}$ and $Tm^{3+}$, which can also be responsible for the deduced increase in the background absorption.

In this experiment, we have cooled a GaAs semiconductor load by means of an optical refrigerator to a temperature of 165K, utilizing E4-E5 Stark manifold transition. This is the first demonstration of cooling a payload with an optical refrigerator that surpasses the performance of a standard thermoelectric cooler. Improved cooling performance can be achieved by optimizing the pump wavelength and increasing the incident pump power. However, even with a weak, tunable, pump such as a Ti:Sapphire laser, it is possible to map the spectroscopic MAT (MAT($\lambda$)) condition by using the strong temperature sensitivity of GaAs as a local thermometer to verify the need for a high power source at 1020 nm.

## 5.3 Spectroscopic MAT (MAT($\lambda$)) measurement

Verification of the MAT($\lambda$) condition ensures that the theory of optical refrigeration with its prediction of 110 K as the global MAT (gMAT) for the 5% wt. $Yb^{3+}$:YLF crystal in Ch. 3 is correct and justifies the need to purchase a high power laser source centered around 1020 nm for low temperature operation. Measurement of the MAT($\lambda$) condition directly would require a widely tunable source (1000 nm - 1080 nm) with high power (10-100 W) throughout the tunable range. Since this is an unreasonable request, a technique using the widely tunable, but lower power ($\sim$1 W) Ti:Sapphire laser must be employed. Previously discussed experiments utilized DLT to measure temperature changes through differences in acquired spectra at current

temperature relative to a reference. While this technique is highly sensitive, it is limited by the speed of the spectrometer readout time which is typically in the tens of milliseconds. Additionally, the sensitivity is degraded by detector noise. With its relatively slow detection speed, DLT is insufficient to measure the local temperature changes quickly enough to measure MAT($\lambda$).

In order to directly verify the cooling efficiency spectra (Fig. 3.22), or equivalently the cooling efficiency map (Fig. 3.23), and in particular MAT($\lambda$), a pump-probe experiment is used to measure local laser-induced temperature change as a function of global (bulk) temperature of the sample. The bulk temperature of the 5% wt $Yb^{3+}$:YLF is varied by means of a $LN_2$ cryostat through a carefully optimized thermal contact of the crystal with the aluminum extension of the cryostats cold-finger, Fig 5.9. When pumped with a tunable source at a cooling wavelength, the laser-irradiated spot initially cools before reversing as the heat from fluorescence absorption at the interface between the crystal and cold-finger diffuses back into the cooled region. Therefore after a short period of time ($\sim$1 sec) only heating is observed. In this arrangement, laser cooling occurs locally, both spatially and temporally. The spatial temperature variation has been addressed previously [53],[54]. The temporal dependence is due to the particular geometry of the experimental setup, where optimization of the thermal contact between the crystal and cold-finger is necessary. The duration of this local cooling becomes shorter for crystals with relatively high thermal conductivity such as YLF (4.3 - 6 W/mK) as compared with glasses ($\sim$1 W/mK). Because of the speed with which this occurs, DLT cannot be used for its relatively slow measurement time. Careful optimization of the thermal contact required the addition of a thin glass slide to increase the thermal resistivity slightly, widening the temporal window for accurate measurement. Increasing thermal resistance further would prevent global cooling of the crystal to low temperatures.

Before describing the new pump-probe experiment used in this work, it is useful

to mention a previously utilized [8, 55, 56, 57] pump-probe arrangement to detect local temperature (i.e. temperature resolved both specially and temporally in the region interrogated by the probe beam). This method measures changes in temperature through an induced refractive index change known as photo-thermal deflection spectroscopy (PTDS). Unfortunately, techniques relying on a refractive index ($n(\lambda)$) measurement (e.g. PTDS) need to separate the thermally induced change to the refractive index ($\delta T$) from the accompanying change caused by pump-induced population changes in both ground and excited states ($\delta N$) [58]. The total change is

$$\delta n = \frac{\partial n}{\partial N}\delta N + \frac{\partial n}{\partial T}\delta T, \tag{5.3}$$

where in principle, this separation cannot be achieved by wavelength selection of the probe alone, since pump-induced absorption change leads to a refractive index change at all wavelengths as per Kramers-Kronig relations. It is possible to circumvent this problem, unfortunately with the introduction of a new issue. Because the population excitation remains local while the temperature change diffuses outward, a lateral displacement of the pump and probe beams separates the contributions from thermal and population effects. Unfortunately, this requires optimal focusing geometries for both pump and probe beams, and their optimal lateral displacement, which are also generally temperature dependent through thermal diffusivity of a medium, e.g. YLF [52]. Finally, since the phase (deflection) accumulated by a probe is proportional to the thickness of the sample, sensitivity of the PTD signal is maximized for long pump-probe overlap geometries, which imposes challenges for focusing geometries as well as imposes demands on sample surface orientations. These complicate the measurements and can even lead to erroneous results, especially at low temperatures. Therefore, a new technique was devised which takes advantage of the previously cooled GaAs load as a sensitive local thermometer.

### 5.3.1 Description of two-band differential spectral metrology (2B-DSM)

Due to the limitations of both differential luminescence thermometry (DLT) and photo-thermal deflection spectrometry (PTDS), we developed new technique using a dual-band spectral differencing via a balanced amplified photodetector (BAPD, for e.g. a bi-cell photodetector) directly in the spectral domain [45]. Due to the large electronic bandwidth and high common-mode-rejection of these detectors, a fast and shot-noise-limited performance can be obtained relatively easily, correcting for the speed and noise issues with DLT. Fluorescence spectrum, as in our case for either semiconductors or rare-earth doped solids, can be sampled directly by means of a monochromator [45], color filters [59], or any other spectrally selective components. Color filters are more suitable for resolving a temperature-induced spectral linewidth change of a fixed transition frequency, for instance directly in rare-earth doped solids. The monochromator offers a continuously-tunable choice for the temperature-dependent transition frequencies, and is therefore suited to measuring changes in the band-gap of a semiconductor (e.g. GaAs). We have termed this technique 2-band differential spectral metrology (2B-DSM).

The work presented in this section utilizes the temperature-dependent band-gap shift of a GaAs/GaInP double heterostructure (GaAs DHS) attached to a 5% wt. $Yb^{3+}$:YLF crystal as a probe, and therefore will focus on utilizing the monochromator. The GaAs disk is probed with a weak (∼15 mW) laser at 650 nm to induce luminescence. The luminescence is collected where a portion of the spectrum, $S(\lambda)$, is interrogated at the exit slit of a monochromator by the BAPD, such that the resulting signal (V) is [45]:

$$V(\lambda_0, T_0) \propto S(\lambda_0 + \Delta\lambda, T_0) - S(\lambda_0 - \Delta\lambda, T_0) \propto \left( \frac{\delta S}{\delta \lambda}\bigg|_{\lambda_0, T_0} \right) \tag{5.4}$$

where $T_0$ is the GaAs temperature, $\lambda_0$ is the center wavelength of the spectral region

within the exit slit of width $2\Delta\lambda$. The spectral derivative approximation assumes that $2\Delta\lambda$ is still narrower than any spectral feature of the luminescence lineshape $S(\lambda)$. Fig. 5.3 gives an example spectrum ($S(\lambda)$) with initial wavelength selection

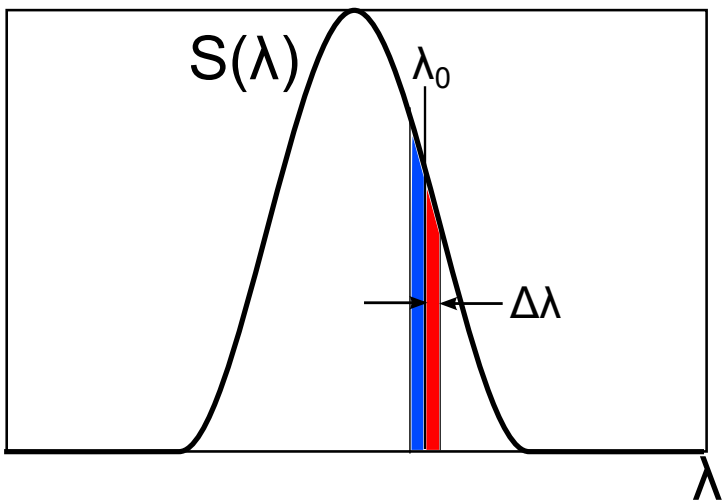


Figure 5.3: An example spectrum ($S(\lambda)$) with initial wavelength selection $\lambda_0$ where the $2\Delta\lambda$ assumption is valid. Note the current selection of $\lambda_0$ results in an unbalanced detection where the shorter wavelength retrieves more signal. Tuning the monochromator balances the detector for background free detection.

$\lambda_0$ where the $2\Delta\lambda$ assumption is valid. It should be noted the selection of $\lambda_0$ in the figure results in an unbalanced detection where the shorter wavelength retrieves more signal. Tuning the monochromator balances the detector for background free detection.

For small temperature change ($\Delta T$) about the initial $T_0$, the V signal (up to the first order) is then given by:

$$V(\Delta T, \lambda_0) \propto \left( \frac{\delta S}{\delta \lambda}\bigg|_{\lambda_0, T_0} \right) + \frac{\delta}{\delta T} \left( \frac{\delta S}{\delta \lambda}\bigg|_{\lambda_0} \right) \Bigg|_{T_0} \Delta T + O[(\Delta T)^2] \tag{5.5}$$

With appropriate choice of $\lambda_0$ by tuning the monochromator to balance the fluorescence, the temperature-independent offset [first term on the right hand side of

Eq. 5.5] can be nullified, such that the signal V (in both magnitude and sign) is background-free and linearly proportional to the temperature change $\Delta$T. Fig 5.4 gives a temperature induced shift (temperature increases for this example) in the

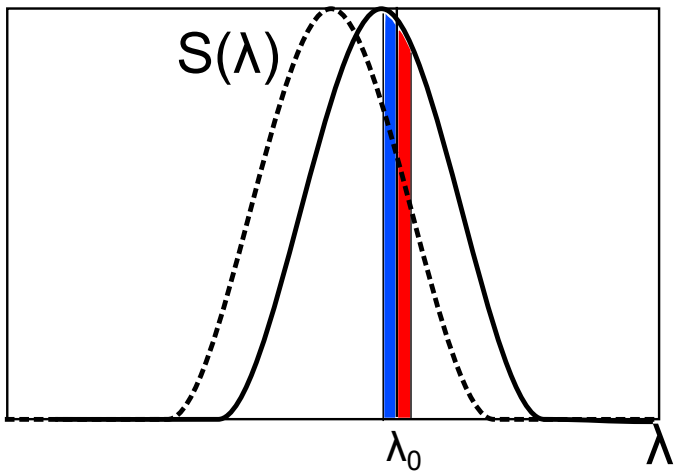


Figure 5.4: An increase in temperature results in an overall spectral shift toward longer wavelengths. The difference in relative magnitudes of $S(\lambda_0 + \Delta\lambda)$ (red) and $S(\lambda_0 - \Delta\lambda)$ (blue) can be seen from $T_0$ (dashed line) to $T_1$ (solid line). The difference is calibrated to an overall temperature change.

spectrum (S($\lambda$)) resulting in a change in detection between the $S(\lambda_0 + \Delta\lambda)$ (red) and $S(\lambda_0 - \Delta\lambda)$ (blue) regions at initial (dashed line) and final (solid line) temperatures. It should be understood that even if the derivative approximation in above expressions cannot be made, spectral shift of the luminescence as measured by the differential V signal can still be calibrated to be proportional to the temperature change.

To verify the measurement technique, a stand-alone experiment on GaAs/InGaP double heterostructure is performed which demonstrates the sensitivity of 2B-DSM. The sample consisted of a GaAs/GaInP double heterostructure of total thickness $\sim 2\mu$m, with high external quantum efficiency ( 95%) used for laser cooling experiments. Pump luminescence does not contribute significantly to the detected signal

due to the counter-propagating geometry, in which case the pump-induced fluorescence is absorbed in the sample, when monitored in transmission. In the current proof-of-principle implementation of the experiment, scanning is automated only along one of the directions, while the scan in the orthogonal direction is performed manually by translating a focusing lens by calibrated distances.

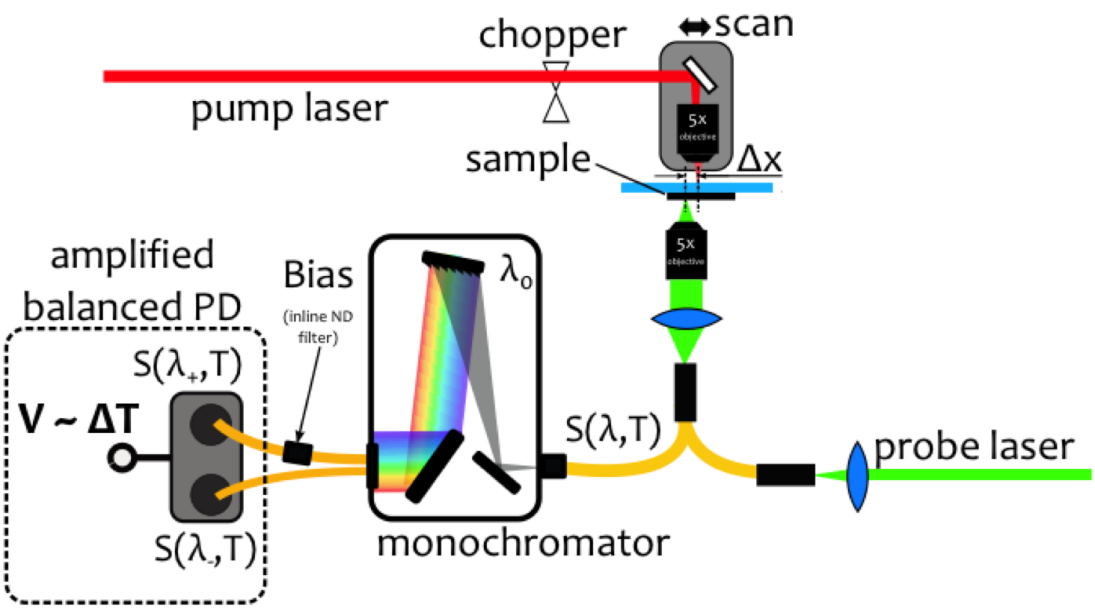


Figure 5.5: Schematic of the pump-probe setup, BAPD balanced amplified photodiode, signal (V) is proportional to the change of temperature ($\Delta$T).

Probe-induced luminescence is collected by a 600 $\mu$m diameter optical fiber and routed into the entrance slit of a scanning MC. Closely spaced and properly oriented cores of two optical fibers at the exit slit of the MC pick up the respective components of the spectrally-dispersed luminescence signal and couple them into the input ports of the BAPD (New Focus Model 2307). By modulating the pump ($\sim$10 Hz), a time-varying differential signal is induced, which is pre-amplified and then averaged on an oscilloscope [Fig. 5.6(c)]. Along with measurement of the differential signals, a spectrometer (Ocean Optics HR4000 with 10$\mu$m slits) is used to measure luminescence

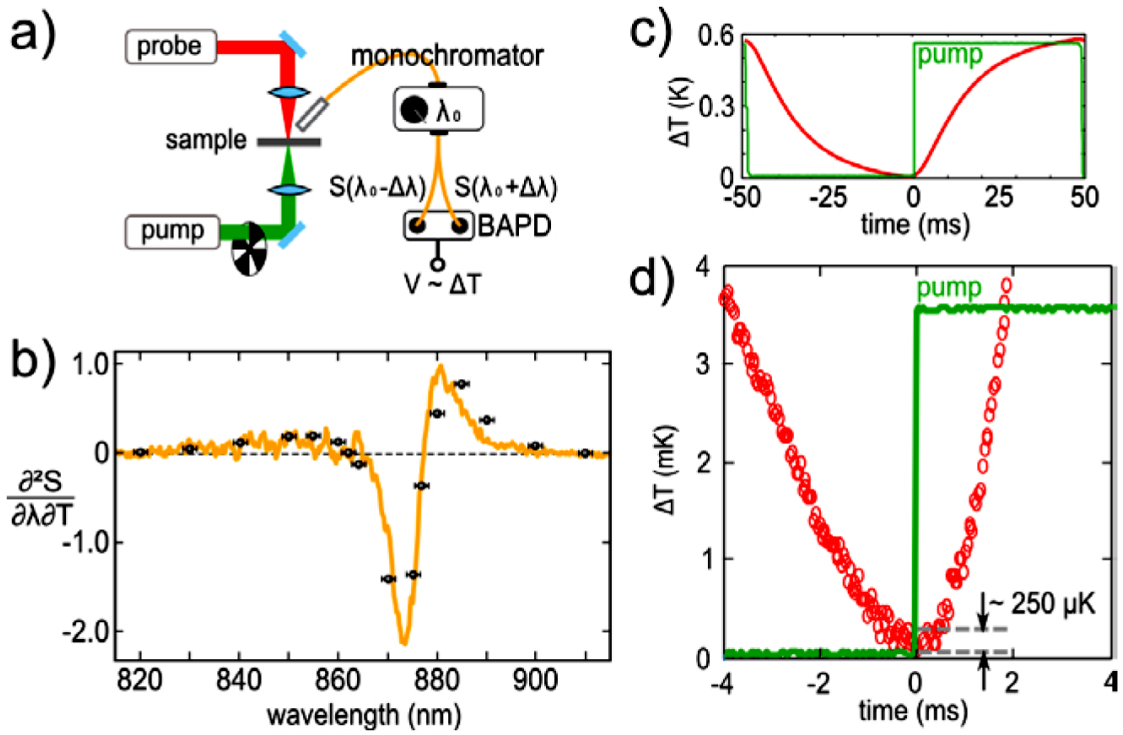


Figure 5.6: (a) Schematic of the pump-probe setup, BAPD balanced amplified photodiode, signal (V) is proportional to the change of temperature ($\Delta$T); (b) Normalized calculated and box-car averaged thermo-spectral derivative (orange line) of a GaAs DHS evaluated at $\lambda_0$ and $T_0$ = 300K is plotted versus $\lambda_0$ together with the normalized magnitude of a measured differential modulated signal (V) (black circles); (c) Modulated pump (green) and temperature (red), as obtained from the probe signal when GaAs semiconductor is excited by 50 mW of 532nm pump and monitored at $\lambda_0$ ~870 nm; (d) Magnification of the panel (c) around t = 0 point; resolution of ~250 $\mu$K is demonstrated after 10,000 waveform averages on an oscilloscope.

spectra of GaAs DHS with and without modulated pump. These additional measurements allowed us to calibrate pump-induced heating of the sample through a Varshni relation [51], as well as allowed for a comparison of the differential signals with that of the predicted behavior in Eq. 5.5. Fig. 5.6(b) shows room-temperature calculated spectrum of $\delta^2 S/\delta\lambda\delta T|_{\lambda_0,T_0}$, performed on a box-car averaged spectra S($\lambda$), with a box size corresponding to $\Delta\lambda$ of 5 nm of the MC. The maximum signal deviation

occurs for h$\nu_0$ $E_g$, the band-gap energy of the GaAs DHS ($\lambda_0 = c/\nu_0 \sim$870 nm). The magnitude of the time-dependent component of the differential signals is plotted on the same axes for various grating positions ($\lambda_0$). A very good agreement is observed, verifying Eq. 5.5 and in particular the linear dependence of the differential signal (V) on the small $\Delta$T, induced by the pump beam. An uncertainty in abscissa coordinate of the 2B-DSM signal is mainly due to the backlash of the screw-controlled grating position of our compact mini-monochromator (Optometrics). Any small systematic differences between calculated and measured values of the derivative spectra are attributed to spectral response differences of the spectrometer CCD and each of the balanced detectors, together with possible neglected higher order contribution terms in Eq. 5.5.

To identify the temperature resolution of the technique, we average 10,000 time-resolved oscilloscope traces of the probe signal monitored at $\lambda_0$ = 870 nm, and converted to temperature by means of a Varshni formula [51]. For a 50 mW pump laser, heating of the heat-sunk GaAs DHS by 0.6 degrees was deduced, Fig. 5.6(c). A close-up view at the early-time probe signal reveals temperature resolution of $\sim$250 $\mu$K over on a sub-millisecond time scale, Fig. 5.6(d). This performance allows for a sensitive determination of the MAT($\lambda$) spectrum.

Finally a two-dimensional scan utilizing 2B-DSM is performed. Calibration of the maximum temperature deviation is verified both by the thermal camera and a thermocouple reader. The thermal profile resulting from a centrally-focused pump is shown in Fig. 5.7. A temperature deviation as high as 14 degrees (312 K absolute) has been detected at the peak of the pump-probe overlap. These results were time-averaged on a time scale of 2.5 ms (lock-in detection with 400 Hz reference).

Next, we analyze steady-state thermal profiles. A solution to the heat diffusion

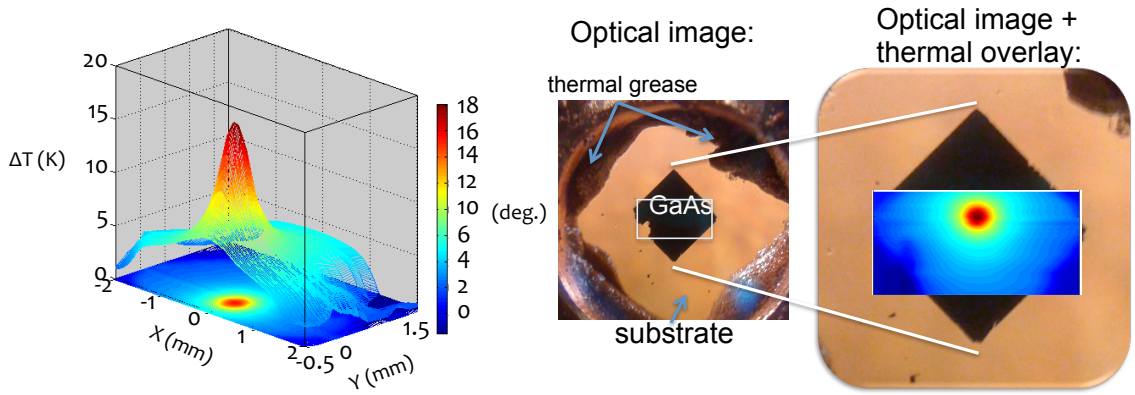


Figure 5.7: (left) Measured temperature profile of GaAs sample; (middle) visible image of the sample and mount, with a scan box outlined schematically in white; (right) superposition of optical and thermal images. Sample edges and edge irregularity (on the left of the sample) are clearly reproduced in the thermal image.

equation

$$\frac{\partial T(r,t)}{\partial t} = \frac{1}{c_p \rho}[G(r,t) + \kappa \nabla^2 T(r,t)] \tag{5.6}$$

describing a sample with $c_p$ specific heat of mass density $\rho$ and thermal conductivity $\kappa$ being excited by a generation term $G(r,t)$, is:1214

$$\Delta T(r,t) = \frac{\alpha I_0}{4\pi\kappa}\left[E_i\left(\frac{-2r^2}{w^2}\right) - E_i\left(\frac{-2r^2}{w^2}\frac{1}{1+2t/\tau_c}\right)\right] \tag{5.7}$$

where $\tau_c = w^2/4D = \rho c_p w^2/4\kappa$. This solution assumes Dirichlet boundary conditions ($\Delta T(r,0) = 0$ for $r < \infty$ and $\Delta T\ (\infty,t) = 0$ for $t > 0$) and generation term $G(r,t) = u(t) \times \alpha I_0 \exp(-2r^2/w^2)$, where $\alpha$ is pump linear absorption coefficient, $I_0$ is pump peak irradiance, $w$ is the pump beam size and $u(t)$ is a Heaviside step function. Exponential integrals are given by $E_i(x) = \int_z^\infty dt \exp(t)/t$.

Utilizing known constants for GaAs, we use Eq. 5.7 to compare predicted thermal profiles with the measured ones. Fig. 5.8 (left) depicts the measured profile (red) made for $r = 0$, i.e. through the center of the excitation with the fit (black). Very good agreement between the prediction and measurement is obtained for small $r$

close to the laser spot, but deviation is also evident in the wings for $r > 0.5$ mm. This is due to the influence of the boundaries, as experimental conditions do not satisfy $\Delta T(\infty, 0) = 0$ requirement. This is due to heat build-up on time scales much longer than pump on-off switch times. Overall agreement between prediction and theory facilitates precisely determining thermal properties of unknown structures, for instance nanoscale devices. This would be possible by modifying the current imaging scheme to accommodate near-field or confocal microscopic geometries.

Finally, we point out overall high spatial and thermal resolution of the system. Fig. 5.8 (right) shows two linear temperature profiles made at $\Delta T(r = 0)$

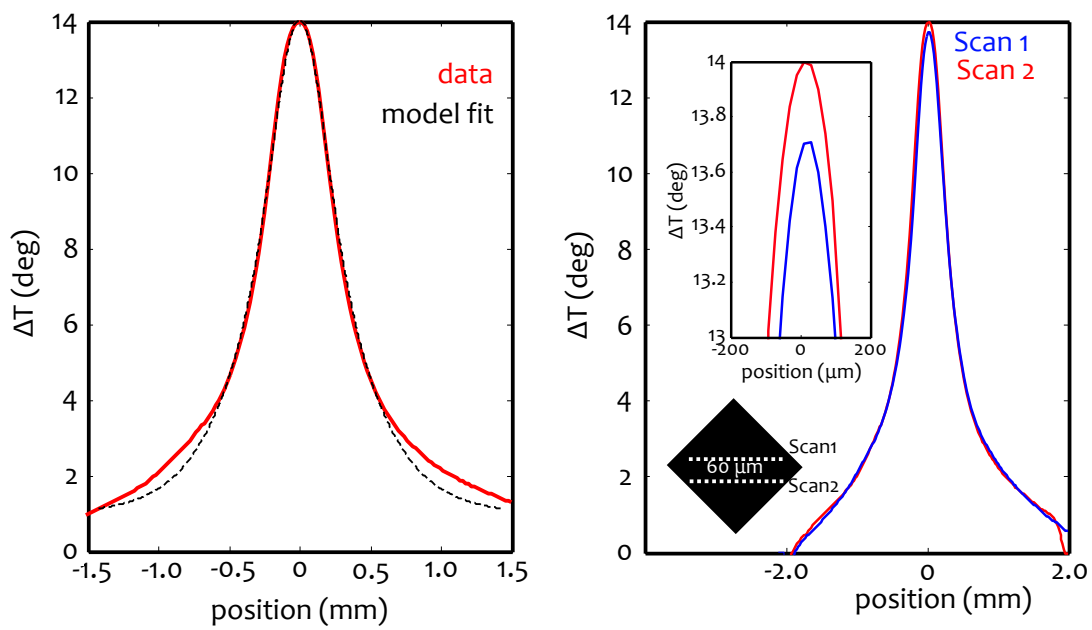


Figure 5.8: (left) Measured temperature profile and a corresponding model fit; (right) Two profiles laterally displaced by 60 $\mu$m, demonstrating high temperature (and correspondingly spatial) resolutions.

and $\Delta T(r = 60\mu\text{m})$. Inset shows that lateral displacement of 60 $\mu$m is clearly resolved and corresponds to 0.3 degree thermal change. Using previously established resolution of 0.25 mK spatial displacements of 50 nm can thus be detected. Current

spatial features of the thermal image are diffusion limited to 30-50 $\mu$m. Equivalently, results of Fig. 5.8 imply that thermal-resolution-limited near-field images with spatial frequencies of 20 $\mu$m can be obtained in the future.

### 5.3.2 Measuring spectroscopic MAT (MAT($\lambda$)) using 2B-DSM

A closeup of the experimental setup for measuring the spectroscopic MAT of the 5% wt. $Yb^{3+}$:YLF crystal from Ch. 3 is shown in Fig. 5.9. The crystal is mounted

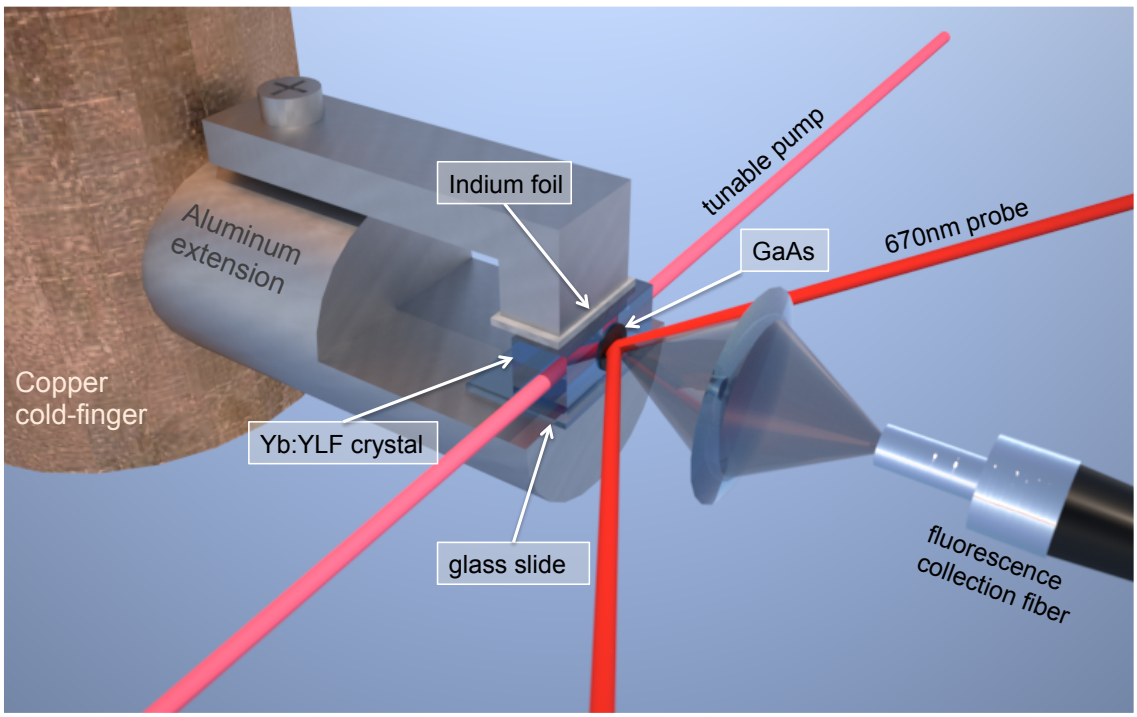


Figure 5.9: Thermal link setup with a copper cold finger with aluminum extension. The crystal is sandwiched between indium foil and a glass slide for optimal thermal characteristics. The crystal is pumped with a tunable Ti:Sapphire and the GaAs is probed with a weak 670nm probe. The fluorescence is focused with a lens into the collecting fiber.

inside a liquid nitrogen cryostat on an aluminum extension to a copper cold finger, which uses a thermal impedance displacer together with a built-in heating element to allow for a potential set temperature in the range of 80 - 350 K. The careful thermal optimization mentioned earlier can be seen in the form of a 150 $\mu$m glass (BK-7) slide beneath the crystal. Attached to the crystal by a low viscosity high thermal conductivity adhesive is a thin disk GaAs heterostructure, the same heterostructure as described in the introduction (Sec. 5.1), which acts as a high-sensitivity local thermometer. The previous cooling experiment in Sec. 5.2 verified the accurate correlation between the crystal and GaAs heterostructure temperatures.

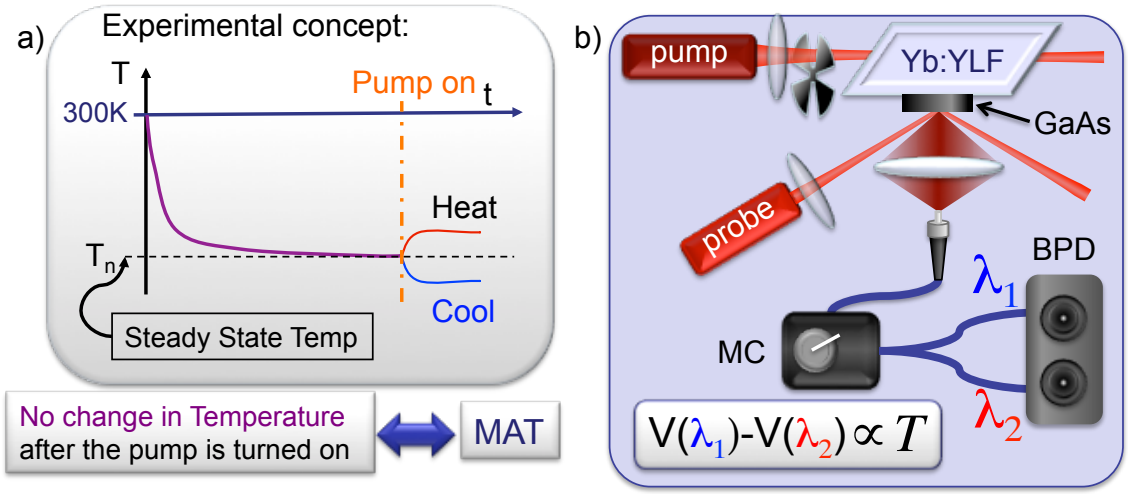


Figure 5.10: Thermal link setup with a copper cold finger with aluminum extension. The crystal is sandwiched between indium foil and a glass slide for optimal thermal characteristics. The crystal is pumped with a tunable Ti:Sapphire and the GaAs is probed with a weak 670nm probe. The fluorescence is focused with a lens into the collecting fiber.

Fig. 5.10 shows the full experimental setup for the spectroscopic MAT measurement. A tunable Ti:Sapphire laser, capable of producing ~1 W of power over the full range of 940 nm - 1080nm, excites $Yb^{3+}$:YLF sample held at variable starting temperatures ($T_0$) (Fig. 5.10 a)). By focusing the pump closely behind the GaAs DHS disk to minimize the thermal time of the laser cooling signal, the pump induced

local cooling can be measured as a temperature dependent spectral shift in GaAs due to its temperature dependent band gap [51]. Luminescence of the GaAs is excited by a CW probe beam (650 nm, 20 mW) and collimated by a lens (N.A. = 0.42) outside the cryostat viewport. Another lens (N.A. = 0.22) is used to refocus the luminescence signal into a NA-matched optical fiber (600 $\mu$m core), which in turn is coupled into an entrance port of a mini-monochromator for 2B-DSM detection. Fast measurement of the GaAs DHS temperature is capable of separating the initial local temperature due to the laser cooling process ($T_0$ - $\Delta T$) from the background heat at the later times.

Fig. 5.11 shows time traces of the 2B-DSM signal for 1020 nm. There is a clear

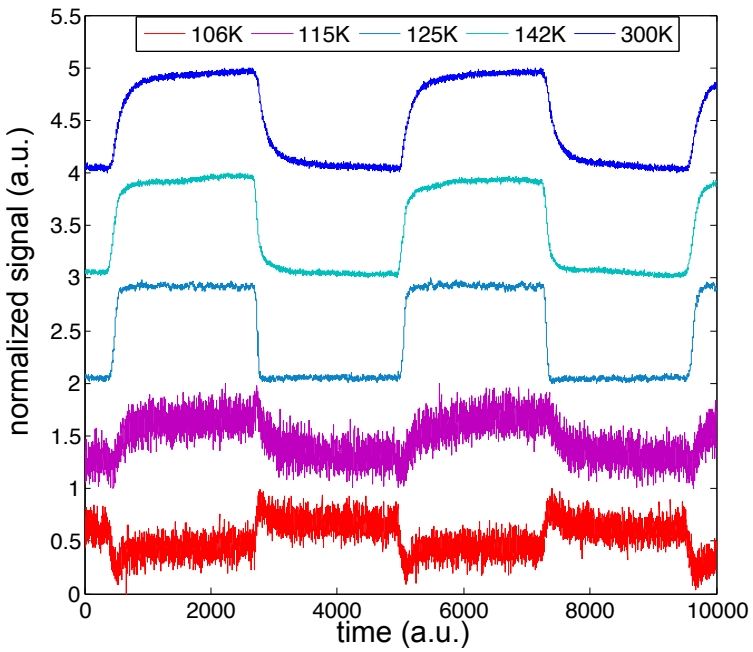


Figure 5.11: Temperature measurements of the 2B-DSM measurement at 1020nm. A clear phase shift occurs between 115 K and 106 K. All signals are normalized and separated for visual ease. Both x-axis and y-axis are arbitrary.

phase shift between crystal temperature at 115 K and 106 K, placing MAT for this wavelength at ~110 K. Sharpness of signal rise and fall times are due to improved

thermal conductivity in YLF at lower temperatures as well as spectral narrowing of GaAs luminescence improving the sensitivity of 2B-DSM. An alternative to varying the sample temperature for a given wavelength is to vary the pump wavelength at a given temperature. Both methods were employed.

Fig. 5.12 a) shows time traces of the 2B-DSM signals from $Yb^{3+}$:YLF/GaAs at

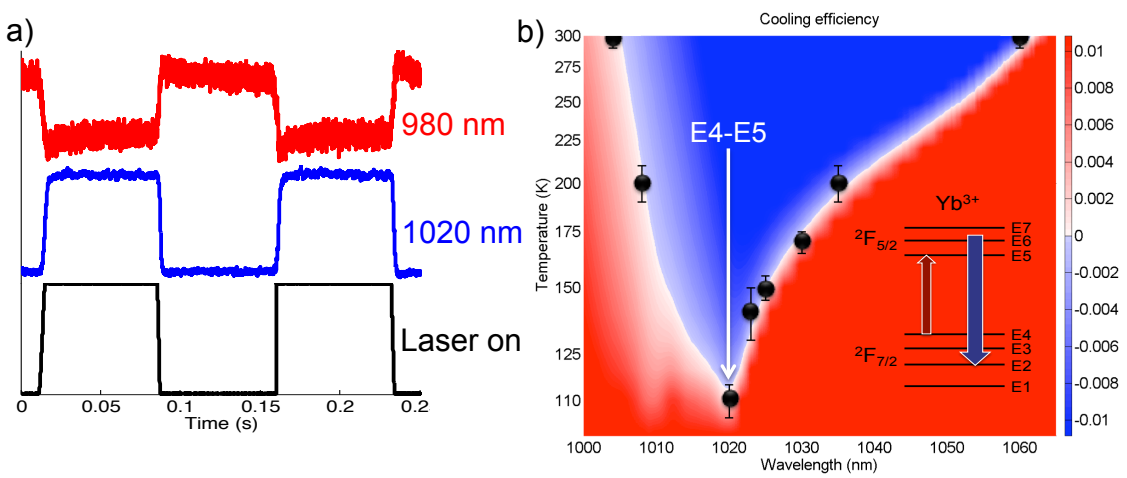


Figure 5.12: a) Experimental concept where the sample held at an initial temperature, $T_n$. When the pump is turned on, heating, cooling or no change will be measured. No change corresponds to the MAT condition. b) Full experimental setup for 2B-DSM measurement.

room temperature. When pump is tuned below (980 nm) and above (1020 nm) the mean luminescence wavelength (∼1000 nm), clear phase-shift of the time traces is evident. For a given excitation wavelength, the transition temperature between local cooling and heating determines the minimum achievable temperature (MAT) for that excitation condition. For each excitation wavelength, the sample temperature ($T_0$ ) is varied via the cryostat, until transition from cooling to heating is observed, corresponding to a sign change of the measured $\Delta T$ [Fig. 5.12(a)]. These transition temperatures are then plotted in Fig. 5.12(b), superimposed on top of a contour plot of the cooling efficiency spectra, as calculated from Eq. (1) and also represented in

Fig. 1. The red color corresponds to heating regions, while the blue area is consistent with cooling. The line separating these regions defines the MAT($\lambda$).

Here the MAT condition predicted from the model is in a very good quantitative agreement with the measurements [Fig. 5.12(b)], verifying both the narrowing of cooling window at lower temperatures and its convergence to the wavelength of 1020 nm, corresponding to the E4-E5 Stark manifold transition [25]. In particular, a measured MAT(1020 nm) = 110±5 K is in excellent agreement with the model, within the current experimental uncertainty, as determined by the experimenters choice of the temperature step in $T_0$. This temperature is below the NIST-defined cryogenic temperature of 123 K and corresponds to the lowest temperature obtained by means of optical refrigeration.

The present results are not plagued by the ambiguities which plague photothermal deflection. In particular we have demonstrated quantitative agreement between the empirical modeling, local measurements and the earlier reported bulk cooling of $Yb^{3+}$:YLF to 155 K at 1023 nm [25]. Demonstrated success of the cooling efficiency model also allows us to more confidently estimate MAT of a typical Yb:ZBLAN (fluorozirconate glass host) to be 180 K. This value is warmer than MAT of $Yb^{3+}$:YLF due to large inhomogeneous broadening of the Stark-manifold levels in glass host, together with smaller allowable $Yb^{3+}$ doping concentration (than in YLF) and comparable background absorption values [14]. Furthermore, previous bulk cooling measurements in Yb:ZBLAN to 208 K at 1026 nm [14] are also consistent with the estimates from the current cooling efficiency model.

Finally, it is noted that this verification of the model also supports the built-in assumptions, namely wavelength- and temperature-independence of the background absorption coefficient. This, in turn, suggests transition metal impurities as the likely source of the parasitic background absorption in YLF, in similarity to the glass hosts [41]. Identifying these impurities directly is a formidable task, as their estimated con-

centrations are well below part per million levels. The obvious incentive however is that temperatures below 100 K and even approaching 77 K are possible upon an order-of-magnitude improvement of the present crystal purity. Ch. 6 addresses the impurity concentrations and identifies a source consistent with background absorption measurements.

## 5.4 Optical refrigeration cooling using a thermal link

The purpose of a thermal link is to provide optically isolating thermal contact between a cooling crystal and a heat load. By employing a thermal link, the heat load can be any device which need to be cooled. A photodetector could be one such device since the detection sensitivity increases when the temperature is lowered. In the previous section, the GaAs load was transparent to the high power $Yb^{3+}$:YLF fluorescence. Other useful devices do not have this property, therefore the load generally cannot be directly mounted to the cooling crystal due to the high power fluorescence that is generated by the optical refrigeration process. For instance, with 24 W of absorbed power in the crystal, ∼24 W of fluorescence is generated (given a high $\eta_{ext}$ tipically 99.5%) with roughly one sixth exiting each face. Therefore ∼4 W of optical power would be incident on a directly mounted device resulting in a significant increase in the heat load. Adding a thermal link provides a path through which fluorescence can escape without being absorbed while maintaining good thermal contact with the applied load to be cooled.

Initial designs for using a thermal link via optical refrigeration were performed previously [60] and provide a good basis for modeling and creating thermal link applications utilizing $Yb^{3+}$:YLF. Changes have been made regarding the choice in

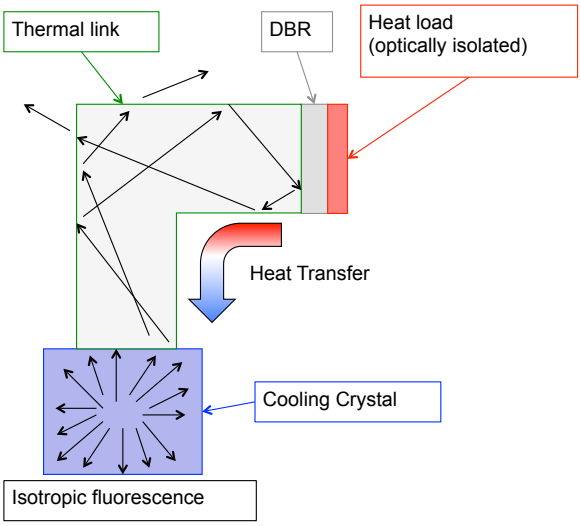


Figure 5.13: Thermal link setup.

mirrors and materials. Previously dielectric mirrors were chosen due to the high fluorescence rejection they provide. Even though dielectric mirrors have very good reflective properties aiding in optical rejection from the applied load, they have poor thermal conductivity which would place a thermal barrier between the cooling crystal and the load. Therefore both semiconductor distributed Bragg reflectors and direct bonding without mirrors are modeled, both of which have significantly improved thermal properties. As a practical application, thermal links were designed, cut and polished to be bonded directly without mirror interfaces.

The basic design for a thermal link attached to a cooling crystal can be seen in Fig. 5.13. The cooling crystal (blue outline) can be attached to a thermal link (green outline) directly by Van Der Waals bonding, as shown, or with an adhesive layer. Direct bonding (adhesive free) ensures no parasitic heating due to adhesive absorption of the fluorescence, but is more costly and difficult due to the polishing constants on the bonded surfaces. Fluorescence generated by the cooling crystal escapes through the thermal link before contacting the heat load. Pictured in Fig. 5.13 is a distributed

Bragg reflector (DBR) layer (grey outline) between the thermal link and a heat load (red outline) which reflects any remaining fluorescence, but becomes a thermal barrier. Therefore optical modeling was performed with and without the DBR layer followed by experimental measurements performed without the DBR mirror barrier.

The first set of designs consider using distributed Bragg reflectors made of $\lambda/2$ stacks of alternating Gallium-Arsenide/Aluminum-Arsenide (GaAs/AlAs). Such mirrors have narrower bandwidth compared with conventional dialectic mirrors (i.e. $Si/SiO_2$), but high incidence angle rejection provided by a high index of refraction. This results in nearly equivalent optical rejection of the isotropic spectral fluorescence of $Yb^{3+}$:YLF when integrating over the solid angle of incidence. Fig. 5.14 shows a direct comparison between semiconductor DBR mirrors Fig. 5.14(a) and dielectric mirrors Fig. 5.14(c). In the case of $Yb^{3+}$:YLF fluorescence which spans ∼940 nm - 1040 nm, the dielectric mirror has slightly higher reflectivity at normal incidence Fig. 5.14(d) compared with the DBR Fig. 5.14(b), however the DBR maintains higher reflectivity at large angles. Integrating over the solid angle of incidence, since fluorescence is isotropic, both mirrors achieve ∼87% total reflection.

More important than the optical rejection of each mirror however is the thermal conductivity. Consider a standard quarter-wave stack of alternating index materials, specifically Gallium Arsenide (GaAs) / Aluminum Arsenide (AlAs) used to create the DBR and $Si/SiO_2$ for a traditional dielectric mirror, Fig. 5.15 [1]. In order to calculate the effective thermal conductivity of such a stack, both the radial ($\kappa_r$),

$$\kappa_r = \frac{\kappa_1 d_1 + \kappa_2 d_2}{d_1 + d_2}, \tag{5.8}$$

and longitudinal ($\kappa_z$),

$$\kappa_r = \frac{\kappa_1 \kappa_2 (d_1 + d_2)}{\kappa_1 d_1 + \kappa_2 d_2}, \tag{5.9}$$

[1] In reality, a DBR and dielectric mirror are the same other than the materials used. Both are alternating quarter wave stacks of different index materials. I will use the term DBR when referring semiconductor DBRs such as GaAs/AlAs mirrors.

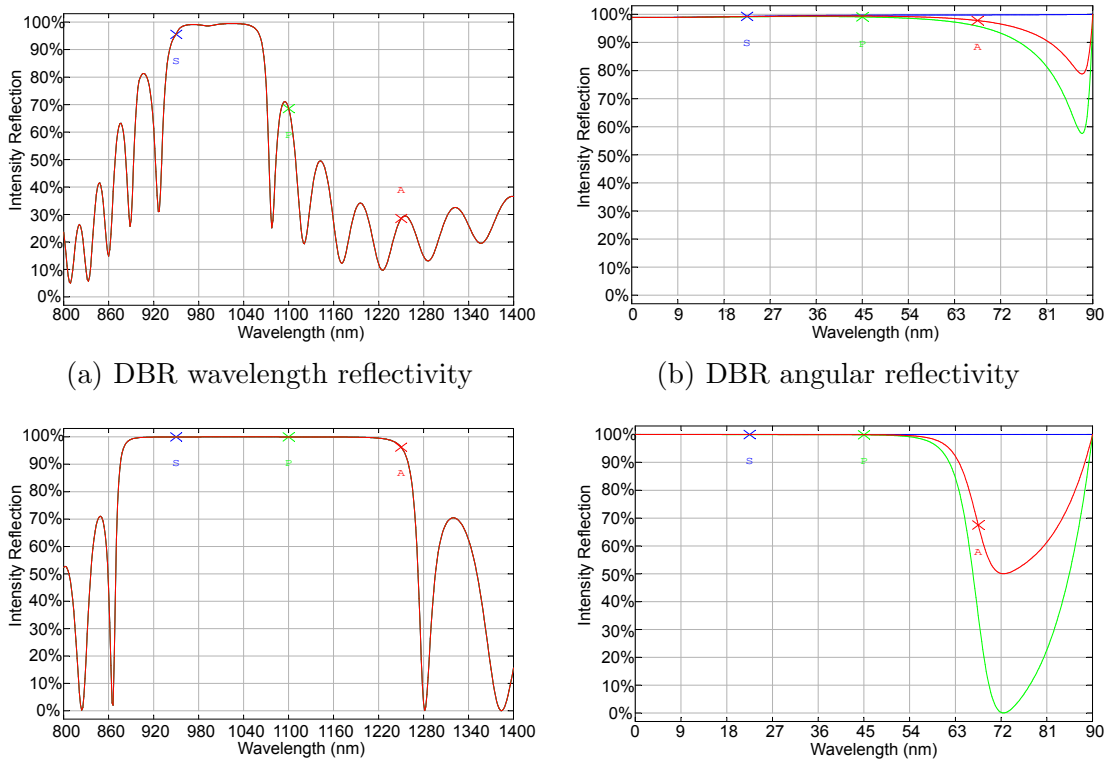


(a) DBR wavelength reflectivity

(b) DBR angular reflectivity

(c) Dielectric wavelength reflectivity

(d) Dielectric angular reflectivity

Figure 5.14: Wavelength and angular polarization dependent reflectivity's of a GaAs/AlAs DBR (a,b) and a $Si/SiO_2$ dielectric mirror (c,d). Blue is s-polarized reflectivity, green is p-polarized reflectivity and red is the average. The total reflectivity considering the solid angle of incidence rays of the DBR and the dielectric are 86.8% and 87% respectively.

thermal conductivities must be considered. Since the thickness of each stack is determined by a given wavelength, $d_i = \lambda_i/4n_i$, these equations can be reduced to

$$\kappa_r = \frac{\kappa_1 n_2 + \kappa_2 n_1}{n_1 + n_2}, \tag{5.10}$$

and

$$\kappa_r = \frac{\kappa_1 \kappa_2 (n_1 + n_2)}{\kappa_1 n_1 + \kappa_2 n_2}, \tag{5.11}$$

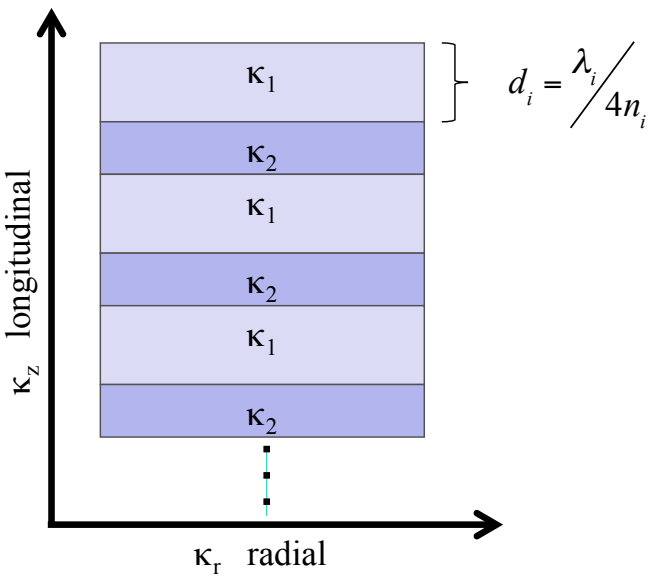


Figure 5.15: A standard quarter-wave stack of alternating index materials. Specifically compared in this work are Gallium Arsenide (GaAs) / Aluminum Arsenide (AlAs) used to create the DBR and $Si/SiO_2$ for a dielectric mirror.

The average is then given by

$$\kappa_{ave} = \sqrt{\kappa_r \kappa_z} = \sqrt{\frac{\kappa_1 n_2 + \kappa_2 n_1}{\kappa_1 n_1 + \kappa_2 n_2} \kappa_1 \kappa_2} \tag{5.12}$$

Comparing the average thermal conductivity of the $Si/SiO_2$ stacked dielectric mirror to the GaAs/AlAs DBR mirror given in Table 5.1, there is a $40\times$ improvement in thermal conductivity by choosing the GaAs/AlAs DBR. Since the optical rejection is equivalent, choosing a DBR mirror for this application is desired.

Thermal link modeling was performed using Zemax. Zemax is an optical analysis program used to design and analyze optical systems. It can perform standard sequential ray tracing through optical elements, non-sequential ray tracing for analysis of stray light, and physical optics beam propagation. A typical use for Zemax is the design of optical systems such as camera lenses and analysis of illumination systems for buildings or other lighting applications. It can model the propagation of

| Thermal conductivity | | | | | |
|---|---|---|---|---|---|
| Mirror Composition | $\kappa_1(\frac{W}{cmK})$ | $\kappa_2(\frac{W}{cmK})$ | $\kappa_r(\frac{W}{cmK})$ | $\kappa_z(\frac{W}{cmK})$ | $\kappa_{ave}(\frac{W}{cmK})$ |
| $Si/SiO_2$ | 0.026 | 0.012 | 0.016 | 0.014 | 0.015** |
| Si/MgO | 0.026 | 0.53 | 0.368 | 0.073 | 0.164 |
| $Si/Al_2O_3$ | 0.026 | 0.36 | 0.251 | 0.069 | 0.132 |
| GaAs/AlAs | 0.44 | 0.91 | 0.693 | 0.609 | 0.65** |
| $Al_{.15}Ga_{.85}As_{.56}Sb_{.44}$/ $AlAs_{.56}Sb_{.44}$ | 0.062 | 0.057 | 0.059 | 0.059 | 0.059 |
| $In_{.68}Ga_{.32}As_{.69}P_{.31}$/InP | 0.045 | 0.68 | 0.376 | 0.088 | 0.182 |

Table 5.1: Thermal conductivities of various alternating index material mirrors.

rays through optical elements such as lenses (including aspheres and gradient index lenses), mirrors, and diffractive optical elements and includes the effects of optical coatings on the surfaces of components. Coatings can be individually designed or selected from various manufacturers, as well as a library of stock lenses, material properties, and components. Absorption and fluorescence properties can be modeled by editing material properties. The physical optics propagation feature can be used for problems where diffraction is important, including the propagation of laser beams, holography, and the coupling of light into single-mode optical fibers. Included is a suite of optimization tools that can be used to optimize a lens design by automatically adjusting parameters to maximize performance and reduce aberrations, along with an extensive tolerancing capability.

A computer aided design (CAD) model was built in ZEMAX to analyze the optical throughput of thermal links of various shapes (Fig. 5.16). First, a cube of $Yb^{3+}$:YLF was modeled starting from stock YLF material and modified with absorption/fluorescence behavior to mimic a 5% wt. $Yb^{3+}$:YLF crystal (Fig. 5.16a-g). This is done by creating a probability that a ray traveling through the YLF block will be converted (i.e. scattered) into another wavelength emitted at a random trajectory. The probabilities are chosen to mimic the absorption per unit length at

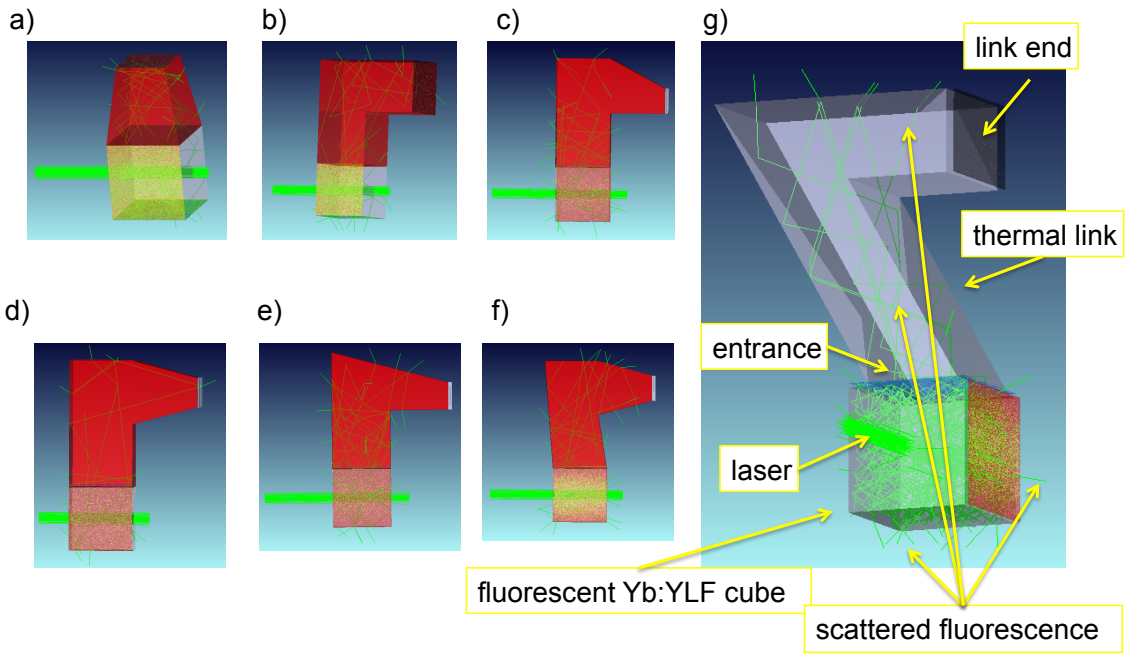


Figure 5.16: Zemax modeling of several thermal links. Green collimated line is the incident laser at 1020 nm while the scattered green lines are fluorescence. In each image, the cube dimensions, absorption, laser intensity, fluorescence intensity and bonding arrangements are the same. a) Simple taper. b) 90° link. c-f) Various iterations of a 90° tapered link. g) Seven link.

1020nm (the pump wavelength of interest) and the relative emission probabilities given by the measured fluorescence. Only 25 points are available to model the full fluorescence spectrum, so wavelengths were chosen to roughly model the full spectrum in 25 pieces. Here it is assumed that non-radiative recombination is negligible, so each photon, if it is absorbed, is converted into another photon. Detectors are used to count all of the photons exiting each face.

Once the YLF crystal model was created to mimic fluorescent $Yb^{3+}$:YLF, several thermal links made of YLF (stock material) were created and attached to one of the YLF cube surfaces (Fig. 5.16 a)-g)). The green collimated line is the incident laser at 1020 nm while the scattered green lines are fluorescence. In each image,

the cube dimensions, absorption, laser intensity, fluorescence intensity and bonding arrangements are the same. YLF was chosen for the link as a worst case scenario to admit all fluorescent light incident on that surface into the link. Another material would have some reflection due to a change in index of refraction. The model assumes perfect contact between materials without adhesive, similar to a Van Der Waals bonding. The bonded surface is considered the "entrance" surface (Fig. 5.16g) into the thermal link. The link "end" (Fig. 5.16g) is where a device would be attached and optically isolated.

Fluorescence rejection models were performed with and without a mirror attached to the link end. In Zemax, any layer can be modified to include a mirror coating as a user defined material or from stock. Since the stock mirror coating parameters are confidential, mirrors were user defined with index properties for $Si/SiO_2$ mirrors and GaAs/AlAs DBR mirrors around the mean fluorescence wavelength of 1 $\mu$m. If two layers are present, i.e. at an interface, the second layer through which the ray would pass defines the coating. To model the mirror before the heat load (Fig. 5.13(grey)), a thin cap was placed (made of YLF) to provide a surface where the mirror is defined and an index matched volume in which to place a detector. This extra volume (which can be seen for instance in Fig. 5.16e as the white line at the link end) where the detector is placed is crucial since a perfect surface modeled in Zemax generates total internal reflection at the link end, especially Fig. 5.16b, artificially preventing any light from escaping. In reality, surface roughness scatters light, reducing total internal reflections, and any device attached would absorb the otherwise reflected light. For the simple taper and 90° link, the detector was moved inside the link volume. To remove the mirror, the surface is simply redefined as having no coating and the extra thin volume at the link end is left in place.

An additional parameter varied in Zemax is the Lambertian scattering from the surfaces of the thermal link. In optics, Lambert's cosine law says that the radiant

intensity or luminous intensity observed from an ideal diffusely reflecting surface is directly proportional to the cosine of the angle $\theta$ between the observer's line of sight and the surface normal. An ideal diffusely reflecting surface is a flat, unpolished surface similar, i.e. frosted glass, and has the same radiance when viewed from any angle. Fig. 5.17 shows unpolished $Yb^{3+}$:YLF as an example of a Lambertian surface.

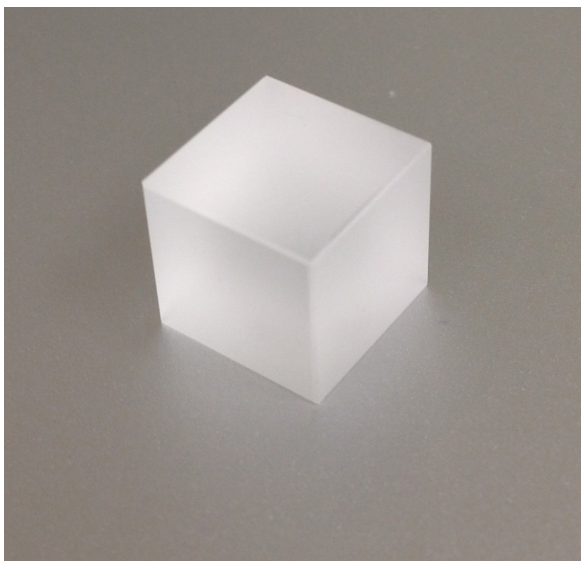

Figure 5.17: Unpolished YLF as an example of a Lambertian surface.

In Zemax, the amount of scattering can be varied from 0%, a perfectly polished surface, to 100%, ideal Lambertian scattering. The effect of applying Lambertian scattering is to change the angle by which light is guided out of the thermal link. Total internal reflection from a well polished surface would lead to most of the light being trapped by the vertical surfaces. The addition of Lambertian scattering allows a higher probability for light to escape from all surfaces. As an example, by placing a detector above the thermal link, more light is guided out of the top with 0% Lambertian scattering than with 30% (see Fig. 5.18). While this condition is advantageous for some link geometries, the total internal reflections can lead to higher incidence on the thermal link end detector. For instance, the 90° link guides light to the link

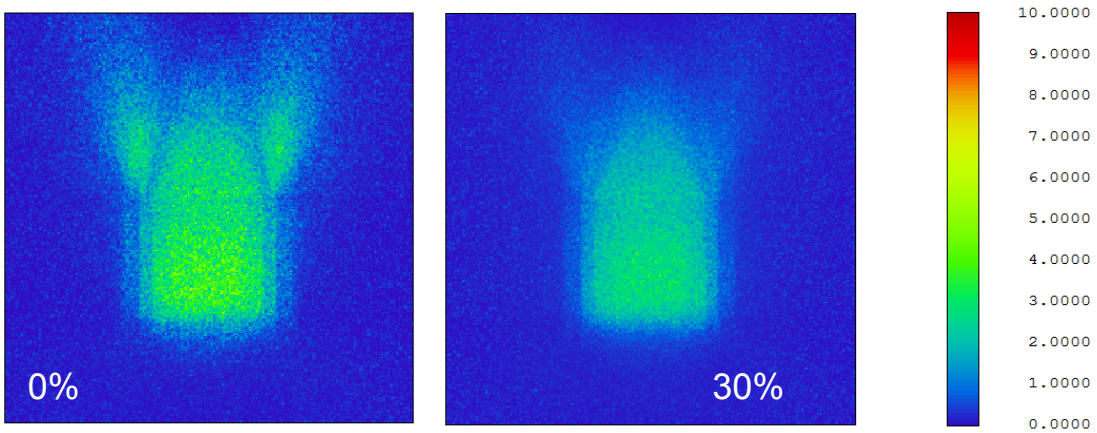


Figure 5.18: Comparison of optical output above a tapered thermal link with 0% relative to 30% Lambertian surfaces. While more light can be seen exiting the top of the 0% which seems advantageous, this effect also leads to higher incidence on the end detector.

end through total internal reflections under the 0% Lambertian scattering condition, optically rejecting only 18%, which eventually leads to increased heat load. The same link with 100% Lambertian scattering rejects 94%. Therefore, Lambertian scattering is varied from 0% to 100% in steps of 10% for each thermal link design to optimize optical rejection.

Detectors are placed to measure the fraction of photons incident on the thermal link end compared with the number entering the thermal link. The detector at the thermal link end absorbs all photons to prevent double counting. The number of photons entering the thermal link are counted by a detector just beyond the entrance face inside the link. Calculations are run twice. On the first run, the entrance face detector absorbs all incident photons to count the number of photons entering the link. On the second calculation, the first detector is ignored and transmits photons which are measured and absorbed at the link end. The ratio of the two gives the % optical rejection for each link geometry. The Optical rejection as a function of

increased Lambertian scattering for the various tapered link designs are plotted in Fig. 5.19. Additionally, Fig. 5.20 shows the comparison between simple link designs

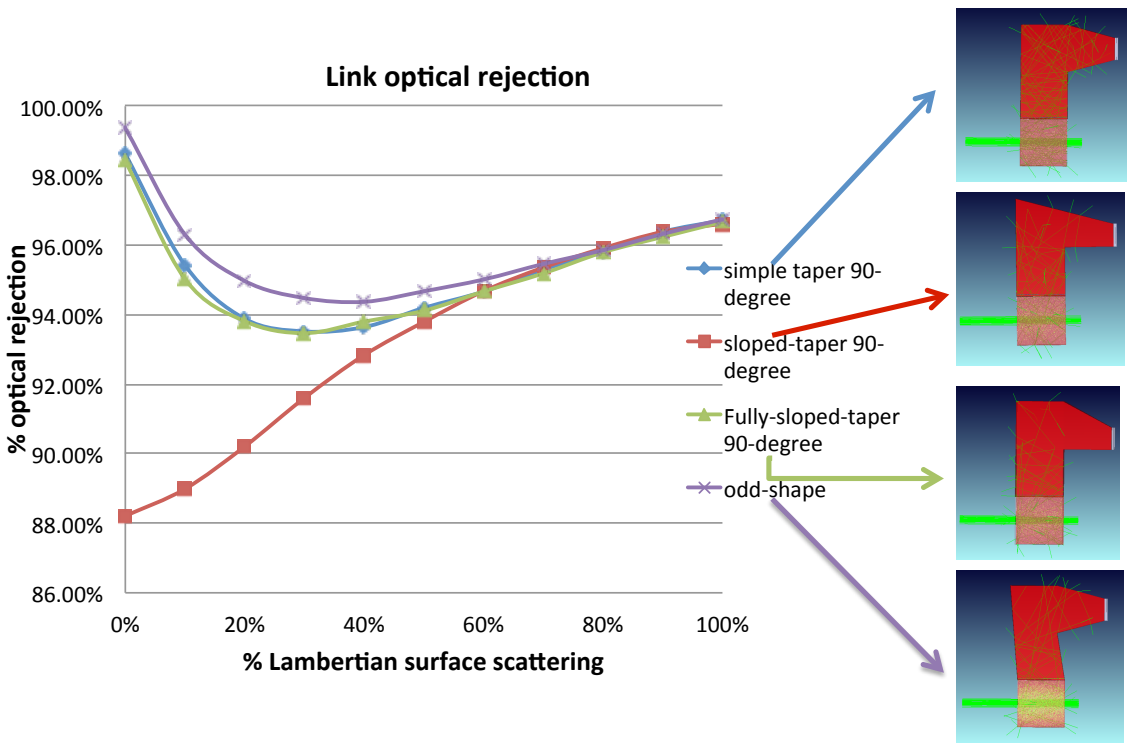


Figure 5.19: Analysis of the tapered link designs. No coatings or mirrors are used. The link throughput detector is placed inside an index matched material where a sensor would reside. In each image it is the white cap at the end of the cold finger. The fluorescent cube, the thermal link, and the cap are all modeled as YLF.

(i.e. simple taper and 90°) with the more complicated tapered designs. Clearly there is an advantage to using a tapered link deign over one that is simpler. However, with the increased Lambertian scattering for the 90° design (Fig. 5.20 (red)), adequate optical rejection can be achieved. If we estimate the additional optical rejection from a high reflectivity metal coating such as gold at the link end, we can get an estimate of the effective increase in parasitic heating. Gold would be deposited in order to bond a device to the link end, so this is a valid assumption. Gold reflects

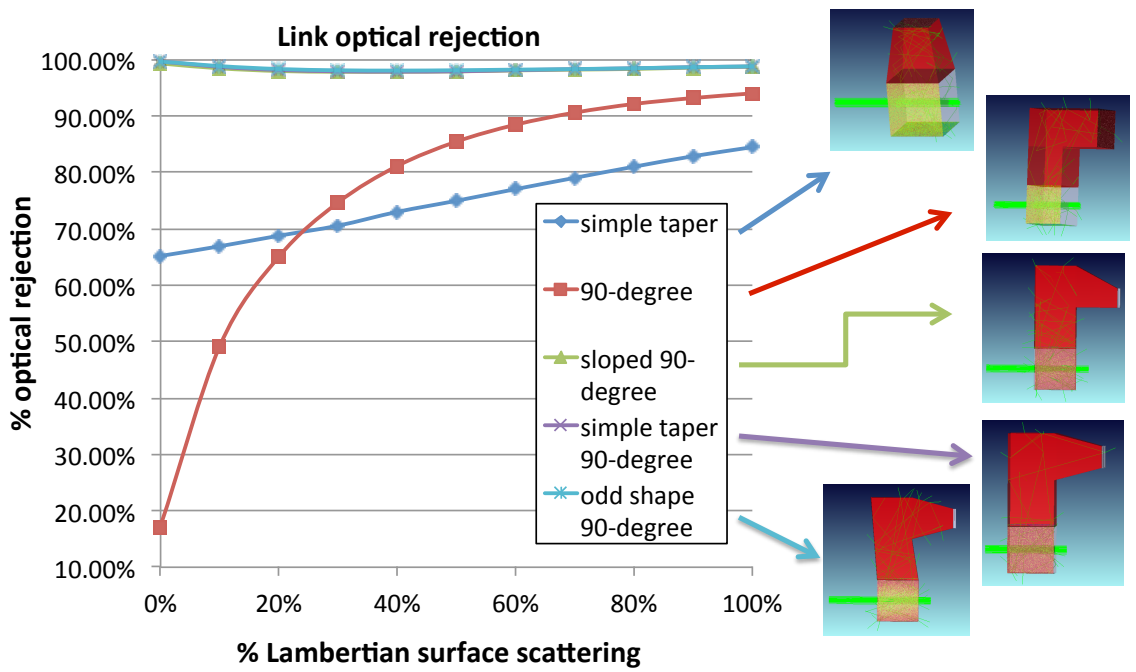


Figure 5.20: Analysis of simple link designs compared with the tapered link designs. No coatings or mirrors are used. The link throughput detector is placed inside an index matched material where a sensor would reside. In each image it is the white cap at the end of the cold finger. The fluorescent cube, the thermal link, and the cap are all modeled as YLF.

>98% of the total fluorescence which spans ~850nm - 1100nm. Therefore considering the simple 90° link at high lambertian scattering (> 70%), the total percentage of photons incident on the device would be ~0.16% of those entering the thermal link. Estimations on the equivalent impact on background absorption show that ~ 1% absorbed light increases $\alpha_b$ by $1.3 \times 10^{-4}\text{cm}^{-1}$. Therefore, with the deposited metal on a simple 90° link, the background absorption increases by $\sim 2.1 \times 10^{-5}\text{cm}^{-1}$, only fractionally increasing MAT for the crystal/link combination. Another estimation is in terms of power. With ~24 W of absorbed power, ~4 W enters the thermal link. If 0.16% is absorbed causing heat, the heat load increases by 6.4 mW.

By adding a DBR mirror at the thermal link end increases optical rejection by removing another 85% of the incident light from the heat load. Figs. 5.21 and 5.22

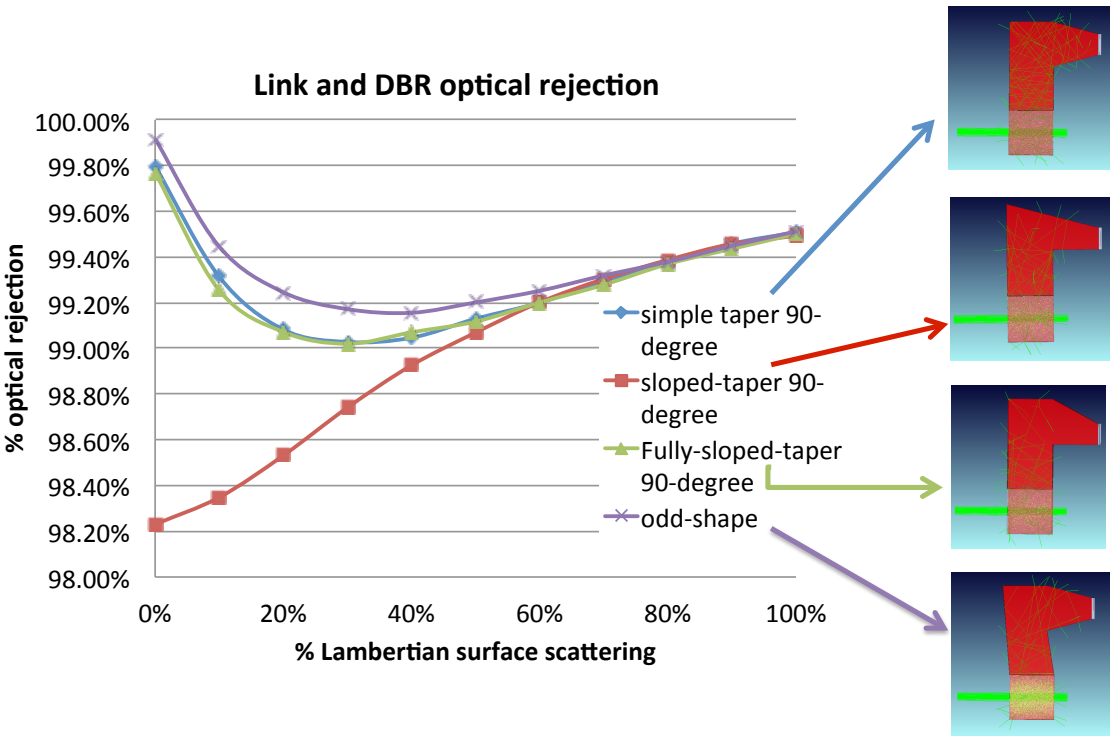


Figure 5.21: Analysis of the tapered link designs with the addition of a DBR mirror at the link end.

give the Zemax results. Notice the similarity between the optical rejection behavior with an increase in magnitude for the same link designs in Figs. 5.19 and 5.20. While the optical rejection with the DBR is excellent, the thermal properties will suffer by introducing another discontinuity. Implementation of a thermal link will take place without the DBR to improve the thermal conductivity.

With estimations completed in Zemax, it is necessary to verify the optical rejection results experimentally, followed by the thermal properties. Two links were fabricated and measured with different bonding techniques. Both of the links are

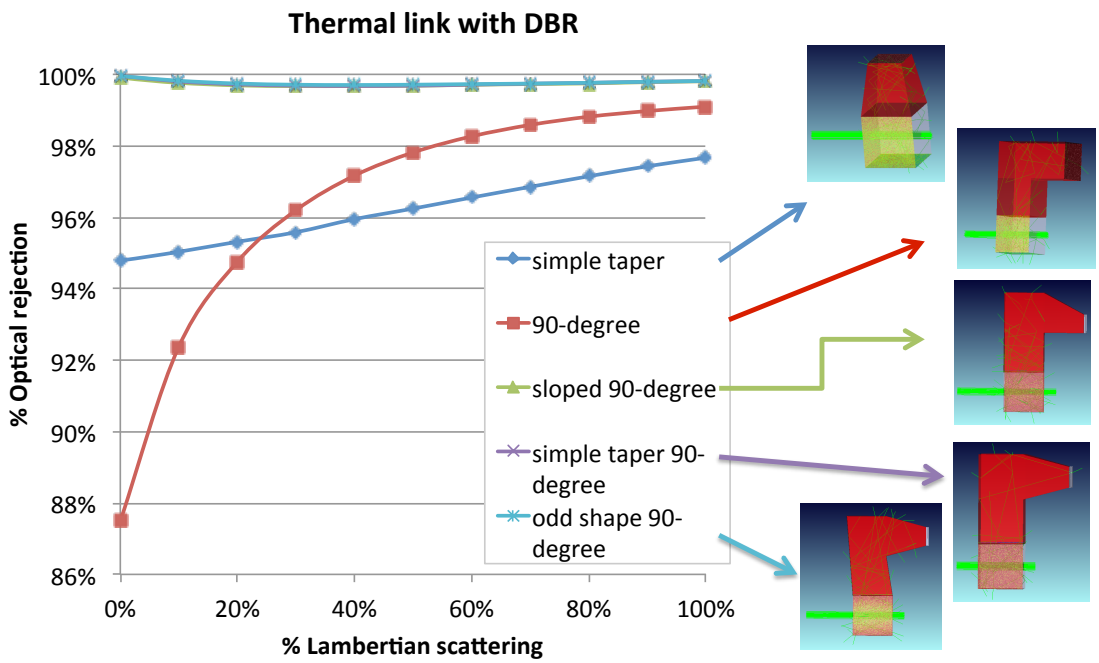


Figure 5.22: Analysis of simple link designs compared with the tapered link designs with the addition of a DBR mirror at the link end.

the simple 90° design. The first link, Fig. 5.23 (a), is a crude verification of optical rejection using fused silica which was cut and polished by the author of this dissertation, bonded with NORLAND UV curable optical adhesive #68. Fused silica is nearly index matched to YLF, n = 1.45 and n = 1.448 respectively, and should therefore provide a good verification of the optical rejection. However, with a low thermal conductivity ($\kappa = 1.38\ \frac{W}{m \cdot K}$ compared to YLF $\kappa = 4 - 6\frac{W}{m \cdot K}$), along with being adhesively bonded, it is not suited to provide cooling to a heat load. Optical fluorescence measurements were taken with a silicon photo-diode comparing fluorescence from the link end and the side of the crystal. A black shroud was used to isolate each measured face from spurious fluorescence, and index matching fluid was used to ensure all photons incident on the measured face are counted (i.e. not trapped due to total internal reflections). According to Zemax, 92% – 94% of the

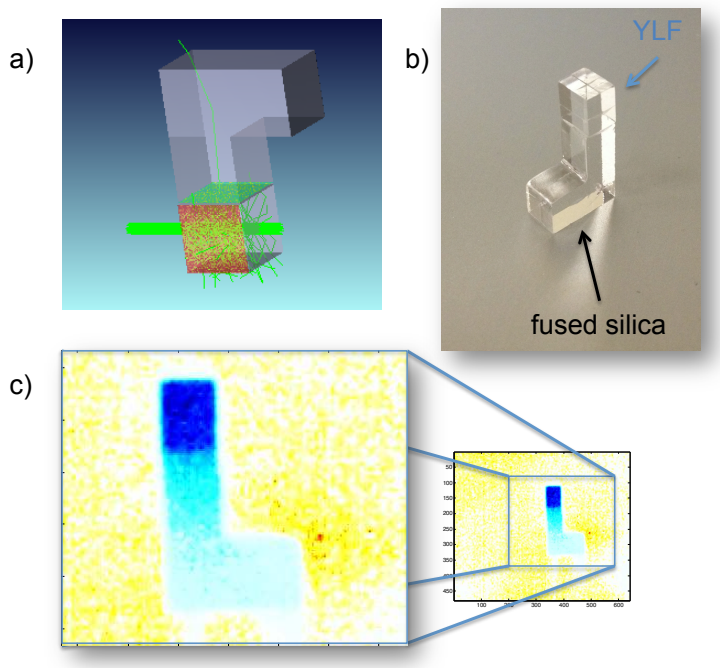


Figure 5.23: a) Zemax modeling of the 90° link. The bold green line is the incident laser with scattered green lines as fluorescence. b) Fused silica 90° link UV adhesively bonded to a 5% wt. $Yb^{3+}$:YLF crystal. c) Thermal image of the cooling crystal bonded to the fused silica link. Blue represents cooling with red heating.

light should be rejected from the link alone, depending on the estimated Lambertian scattering. The measured rejection from the fused silica thermal link is 92.2(±0.5)% verifying the estimations in Zemax.

The second thermal link made of sapphire is shown in Fig. 5.24 , which has a high thermal conductivity of $32 - 35$ W/cm$^2$. This link is Van Der Waals bonded to a 10% $Yb^{3+}$:YLF crystal with low background absorption (10% sample #1 from AC Materials, Tab. B.1.). Without adhesive, thermal contact should be optimized and no parasitic heating should be seen. The company used for the bonding is Onyx Optics, Inc. in Dublin, Ca, where they have a patented technique for adhesive-free bonding. Because their method is proprietary, this author could not independently

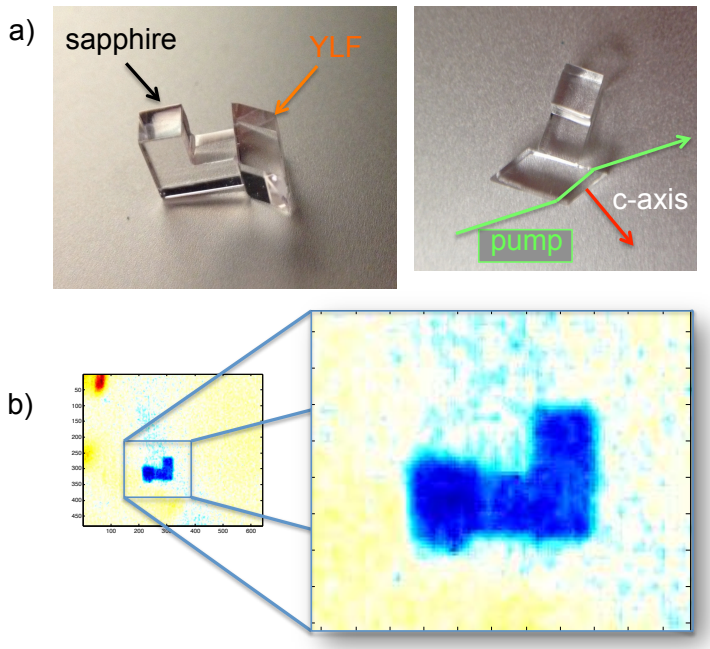


Figure 5.24: a) Sapphire 90° link Van Der Waals bonded to a 10% wt. $Yb^{3+}$:YLF crystal. c) Thermal image of the cooling crystal bonded to the fused sapphire link. Blue represents cooling with red heating.

replicate the bonding, although attempts were made. Unfortunately for this case, the bonding was incorrectly implemented to facilitate optimal absorbed power. Fig. 5.24 a) shows the link attached to the crystal. Pictured in Fig. 5.24 a) (left), the thermal link should have been attached to the top of the $Yb^{3+}$:YLF crystal instead of the left side (as oriented). This would accommodate several passes through the crystal. Instead, only ∼4 passes can fit through the edge of the crystal where the pump orientation is shown in Fig. 5.24 a) (right) relative to the crystal axis for pumping E‖c. Because the $Yb^{3+}$:YLF crystal with link is still usable, experiments were performed to characterize the performance. With promising results, a second link will be bonded to another, larger, 10% $Yb^{3+}$:YLF crystal. Optical rejection measurements were performed in the same manner as the previous, fused silica link, where spurious

fluorescence was shrouded from the detector to only measure photons incident to the measured surface. Because only one type of index matching fluid was available, there is a slight mismatch between the fluid and the sapphire which has an index of refraction n= $1.755(at 1000nm)$. Measurements showed slightly higher optical rejection with $92.8(\pm 0.5)\%$ which is still within the estimate computed in Zemax.

Further analysis of the thermal properties is performed to characterized the thermal conductivity of both fused silica and sapphire, as well as the adhesive interface between the cooling crystal and the thermal link at ambient temperature and pressure. Knowing the thermal properties of fused silica beforehand, it was clear this material would not be used to implement cooling a device. However, it is useful to measure the thermal discontinuity between the crystal and the link in order to determine the simplest and most cost effective method of bonding. If simple UV curable adhesive bonding is adequate, costlier bonding methods, such as Van Der Waals bonding, can be avoided.

Fig. 5.23 c) shows the thermal image of the fused silica sample with the thermal link. Clearly there is a discontinuity at the interface between the crystal and thermal link demonstrating the inadequate thermal conductivity of the interface. It is likely other adhesives will cause the same discontinuity and should therefore be avoided. Additionally, there is a significant gradient through the thermal link from the cooling crystal to the link end highlighting the poor thermal properties of fused silica. Alternatively, Fig. 5.24 c) shows the thermal image of the sapphire link where the discontinuity has been removed. Only a slight difference at the interface can be perceived, however, this is caused be a reflection from the mount, and is not a true temperature. This was verified when the reflection could be moved to other parts of the thermal link based on the orientation, revealing the true temperature. Not all reflections could be removed, therefore this particular reflection was chosen to highlight the temperature at the link end where a load would be placed.

To get a better idea of the difference between the fused silica and sapphire links, a temperature profile was measured from the thermal images, Fig. 5.25. The areas

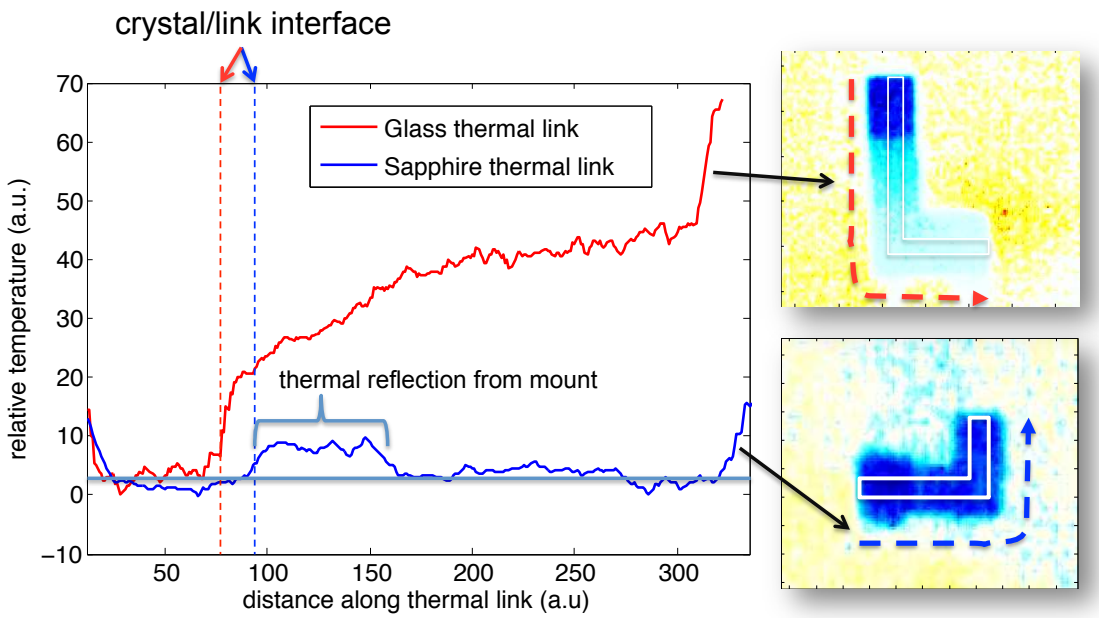


Figure 5.25: Thermal link profile measurements (left) for fused silica (red) and sapphire (blue) corresponding to the white inset boxes in the images (right) along the direction of the respective arrows. A thermal reflection from the mount can be seen in the sapphire profile. The sapphire link profile shows excellent thermal conductivity to the link end where a load would be applied.

inside the inset white box for each image were averaged perpendicular to the link direction given by the arrows. The crystal/link interface is highlighted for the glass and sapphire links in red and blue respectively. The bump in the blue profile measurement is the reflection mentioned previously. Other reflections on the thermal link were removed.

Within error, both links show equivalent optical rejection confirmed by Zemax modeling for a 90° link shape of ∼92.5%. The high thermal conductivity sapphire link ($32-35$ W/cm$^2$), utilizing-adhesive free bonding, clearly outperforms the fused silica

link, as expected, with the additional feature of excellent thermal contact between the 10% $Yb^{3+}$:YLF crystal and sapphire. This means the final application of an applied load will receive significant heat removal. Since the final application is to cool a load to low temperatures, it is necessary to complete a LITMoS test to characterize the cooling efficiency and determine MAT. Only the sapphire link is analyzed. Since the Van Der Waals bond strength between sapphire and YLF is unknown, two LITMoS tests are performed: one before thorough cleaning, and one after. Cleaning will be necessary to ensure the best cooling performance. Oils and other deposits cause parasitic heating on the surface of the crystal, effecting the background absorption measurement. However, since cleaning requires the use of solvents which may effect the bond or may separate the pieces entirely, a LITMoS test was performed before and after cleaning. Fig. 5.26 shows the LITMoS test before (red) and after (blue) cleaning the sample (Cleaning did not damage the interface or separate the pieces). The LITMoS test of the original sample (10% $Yb^{3+}$:YLF sample #1 from AC Materials) resulted in $\alpha_b = 2.0 \times 10^{-4}\text{cm}^{-1}$ and $\eta_{ext} = 99.6\%$ and gMAT of 93 K. Before cleaning, impurity deposits induces parasitic heating on the surfaces, increasing the background absorption value substantially to $\alpha_b = 1.4 \times 10^{-3}\text{cm}^{-1}$ and $\eta_{ext} = 99.5\%$, where gMAT would be 135 K. Since cleaning was safe, a second LITMoS test showed near recovery of the original measurements, $\alpha_b = 2.4 \times 10^{-4}\text{cm}^{-1}$ and $\eta_{ext} = 99.5\%$. This means gMAT for the sapphire link bonded to a 10% $Yb^{3+}$:YLF is 100 K.

Results from heat load experiments show great promise towards advancing optical refrigeration into the realm of application. Since both thermal conductivity and optical rejection have been achieved in thermal links, an applied load is sure to be implemented along with the necessary heat load management.

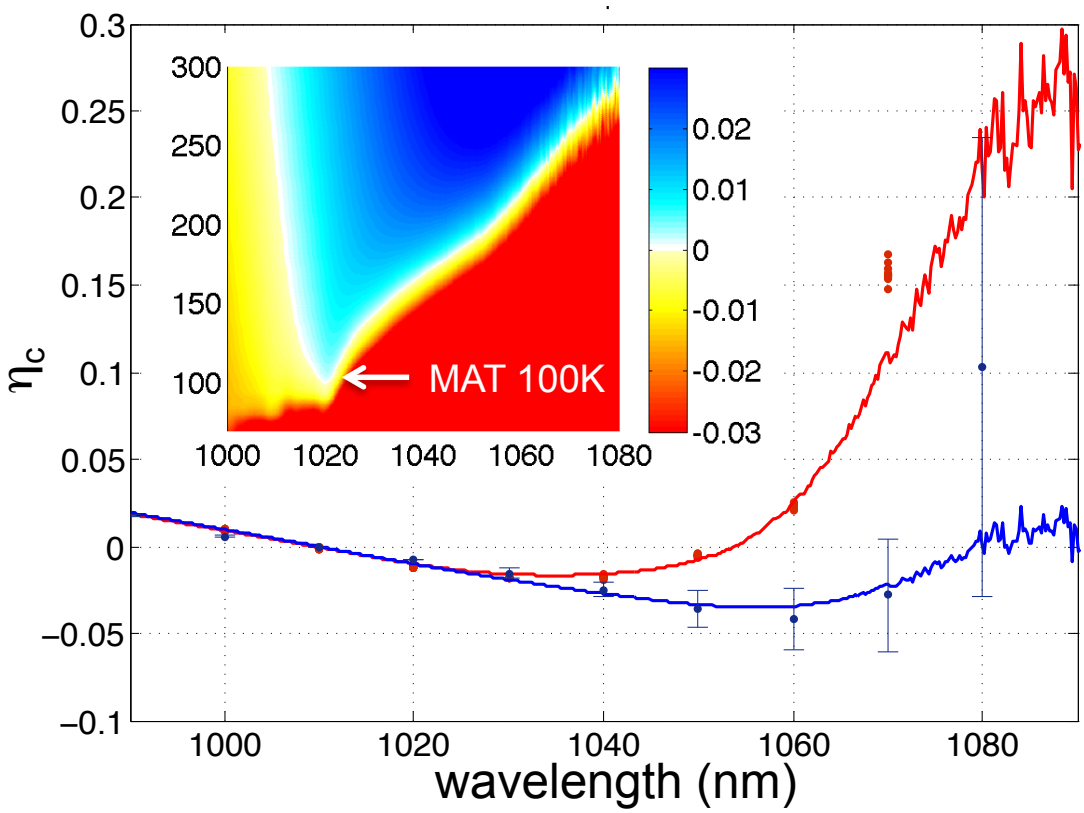


Figure 5.26: LITMoS test for the sapphire thermal link attached to the 10% $Yb^{3+}$:YLF sample #1 from AC Materials. Before cleaning, parasitic heating caused long wavelength heating that was not previously present resulting in $\alpha_b = 1.4 \times 10^{-3}\text{cm}^{-1}$ and $\eta_{ext} = 99.5\%$. After cleaning, the original results were nearly recovered, $\alpha_b = 2.4 \times 10^{-4}\text{cm}^{-1}$ and $\eta_{ext} = 99.5\%$. (For reference, Previous background absorption measurements show $\alpha_b = 2.0 \times 10^{-4}\text{cm}^{-1}$ and $\eta_{ext} = 99.6\%$). Inset is the cooling efficiency contour map for the measured values after cleaning.

# Chapter 6

# Trace Element Analysis

## 6.1 Introduction

Understanding the full composition of the cooling crystals, especially impurities, is necessary to push optical refrigeration to new record low temperatures with an immediate goal of liquid nitrogen ($LN_2$) at 77K. It is necessary, not only to determine the impurity concentrations, but also the absorption cross section and overlap with $Yb^{3+}$. The step taken in this dissertation is to determine impurities via trace element analysis relative to background absorption measurements to find the most likely cause of parasitic heating.

## 6.2 Trace element methodology

The Department of Earth and Planetary Sciences at the University of New Mexico has a class 100 cleanroom. Capabilities useful for the measurement and preparation of Yb:YLF samples include:

- A water deionization system with continuously circulated 18MΩ $H_2O$
- Ultra pure acids for dissolution
- Painstakingly leached teflon vials for sample preparation
- Two inductively coupled mass spectrometers (MC-ICP and Q-ICP)

The doubly distilled acids used for dissolution are useful for detecting 65 elements in the parts per trillion (ppt) range and contain $< 10$ parts per trillion (ppt) for 50 elements without exceeding 500 ppt for the total element impurities. The teflon vials have each been thoroughly cleaned and leached by boiling in ultra-pure nitric acid for two sessions 8 hours each and again in 18MΩ de-ionized water for 8 hours. The Thermo Neptune multi-collector inductively coupled plasma mass spectrometer (MC-ICPMS) is a double-focusing high-resolution mass spectrometer. It has 9 Faraday one SEM and 5 channeltron detectors. The Faraday cups can be coupled to software switchable amplifiers with $10^{10}$, $10^{11}$ and $10^{12}$ ohm resistors. The instrument is coupled to an Aridus II nebulizer. It is capable of measuring isotope ratios of most elements in the periodic table. The second mass spectrometer (Q-ICP) is a Thermo X-series quadrupole mass spectrometer for major and trace element analysis.

In order to determine the trace elements in Yb:YLF, it was first necessary to create a method of dissolution since no method of dissolution for Yb:YLF could be found in literature. Fluoride glasses and crystals can be extremely difficult to dissolve, and previous work by Wendy Patterson [61] required dissolving the constituents of Yb:ZBLAN for analysis prior to synthesis since Yb:ZBLAN itself cannot be dissolved. For the case of YLF crystals, both the $Yb^{3+}$:YLF sample and constituents, LiF, $YbF_3$ (99.99%), $YbF_3$ (99.999%), $YF_3$ (99.999%), and $YF_3$ (99.9999%) were prepared and dissolved. Dissolution of solids uses extremely hazardous, highly concentrated acids, and therefore strict safety precautions must be followed.

Dissolution begins with the Yb:YLF sample prepared by thoroughly cleaning in an ultrasonic bath with acetone to remove most organic surface impurities. Then, inside of the class 100 cleanroom, the method for sample preparation is as follows:

1. The crystal is cleaned with ultra-pure 18MΩ resistance de-ionized water as a general surface preparation
2. One surface is removed by scraping with a tungsten carbide bit to remove any remaining surface impurities and expose the internal crystal from where the sample is taken.[1]
3. The dissolution sample is scraped from the exposed internal crystal, taking care to avoid any surface that has not been previously removed. This scraping also serves to finely crush the sample, a necessary step for dissolution.
4. Once $\sim$ 10mg of material (carefully weighed) is generated, it is placed into a previously leached and weighed teflon vial.
5. The sample is ready for dissolution

The constituents require a different preparation technique, primarily because they are provided in a crushed crystalline form, but also because during growth, any impurities on the crushed crystalline surface will be introduced into the melt, making it necessary to test both the surface and interior. The given form of crushed crystals take enormous effort to be dissolved other than LiF. Therefore, a mortar and pestle was provided by the EPS department inside of the clean room to create a fine powder of each constituent, and dissolved sample of both original and powdered samples were measured. The method of preparing the powdered constituent samples inside of the class 100 clean room is as follows;

[1]It was found that a carbide **tipped** tool contaminates the sample with iron, so the bit should be made up of entirely tungsten carbide which did not cause contamination.

1. Thoroughly clean **all** of the mortar and pestle surfaces with 18 MΩ deionized water as well as the working area.

2. Pour 5-10 crystal pieces of one constituent into the mortar and carefully crush with the pestle into a very fine powder. Initial crystal size is ∼1-2 $mm^3$, and final powder form is similar to powdered sugar.

3. In a previously prepared teflon beaker, pour 10-15 mg of sample and tightly replace lid.

4. Repeat steps 1–3 for each constituent.

To experimentally find a dissolution method, a 5% wt. Yb:YLF crystal which did not exhibit cooling was used serving two purposes: 1) a crystal which exhibits no cooling is likely to have high, easily detectable, impurity levels and 2) since the crystal showed no cooling, the precious cooling samples remain undamaged. Initially, several acids were tried with limited success including various combinations of boric acid ($B(OH)_3$), sulfuric acid ($H_2SO_4$), hydrofluoric acid (HF), hydrochloric acid (HCl), and nitric acid ($HNO_3$) both with and without heat. During this experimental phase, a very slight amount of crystal was noticed to dissolve after boiling using a form of aqua regia[2], a mixture of nitric and hydrochloric acids. Boric acid and sulfuric acid both seemed to have very little effect on dissolving YLF, while hydrofluoric acid caused a precipitation of the dissolution, and should therefore be avoided. The systematic dissolution method for Yb:YLF used for this work is as follows:

1. The previously prepared powdered sample inside a leached teflon vial is combined with ∼60 drops of 15N $HNO_3$ and 60 drops of 6N HCL

2. Tightly replace the lid and put on hot plate which is hot enough to boil the solution, but doesn't melt the teflon beaker

[2]Aqua regia literally means "royal water", so named for its ability to dissolve a king's golden crown.

3. Boil for at least 4 hours to drive off the fluorine atoms. If the lid leaks, more acid may need to be added to prevent the sample from drying before it is dissolved. If the sample dries prematurely, a crystalline precipitate is formed which is very difficult to dissolve and it was found easiest to begin again with a fresh powdered crystal.

4. Remove the lid and verify dissolution of the powder allowing time for any small particles to settle.

5. If dissolved, boil off remaining liquid and move to step 7.

6. If not dissolved, boil of most of the liquid, leaving about 1 drop to avoid the crystalline precipitate, and restart from step 1 with 25 drops of each acid. The constituents $YF_3$ and $YbF_3$ required repeating steps 1–4 several times ($\sim$ 10 times) with $\sim$ 50 drops of each acid.

7. After remaining liquid has boiled off, either a small drop of easily dissolvable solid or no visible solid should remain. Add a solution of 3% $HNO_3$ with 10 ppb indium for a dilution of 1:1000, e.g. for 15mg of original powder, dilute with 15ml of solution. This solution gives a reference count for indium and also serves as the blank in the mass spectrometer.

The Thermo X-series quadrupole mass spectrometer (Q-ICP) was used to find a baseline of impurity elements.

## 6.3 Trace element measurement

Based on optical refrigeration theory, a correlation should be found between a background absorption measurement and the impurity concentrations as measured by

performing trace element analysis. A series of crystals were purchased from AC Materials in Tarpon Springs, FL consisting of 0%, 1%, 5%, 7% and 10% wt. Yb:YLF. Such a series has potential to indicate whether impurities are introduced by the starting materials for either the dopant, Yb, or the host, YLF. If background absorption measurements increase with an increase in doping, a method of purification of the doping material is needed. If however, the background absorption remains constant or decreases, the host material should be purified.

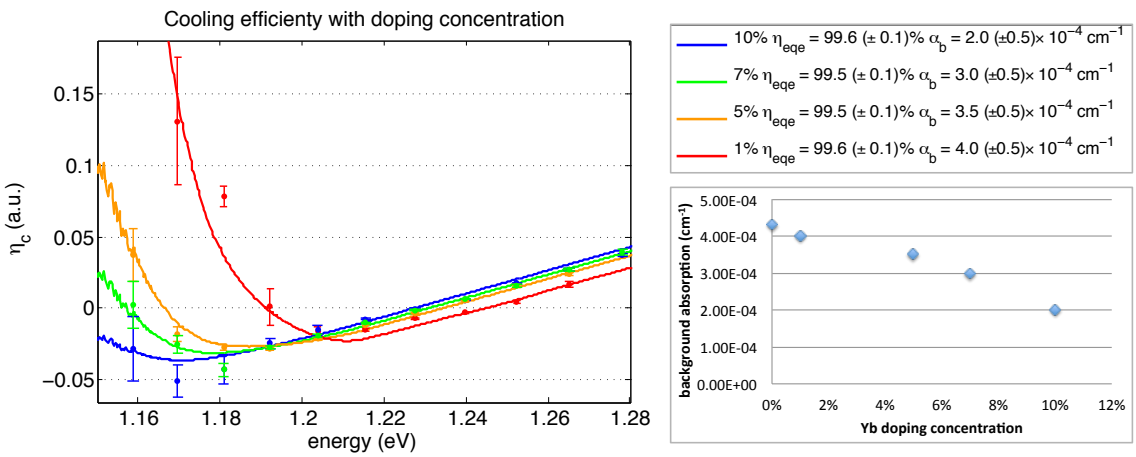


Figure 6.1: Measured values of the cooling efficiency with error bars fit by the theory for 1% (red), 5% (orange), 7% (green), and 10% (blue) samples grown by AC Materials.

Fig. 6.1 is a measurement of the cooling efficiency of the 1% (red), 5% (orange), 7% (green), and 10% (blue) samples as a function of energy with color coded fits giving values for $\eta_{eqe}$ and $\alpha_b$ seen in the legend. The right hand (high energy) zero crossing shift towards lower energy with increased doping is due to the change in reabsorption which red shifts the mean fluorescence. This shift would appear to reduce the external quantum efficiency ($\eta_{eqe}$), however, because the mean fluorescence energy also reduces with doping, $\eta_{eqe}$ remains nearly constant. The background absorption for the un-doped sample was determined by the relative heating compared

with the 1% wt. Yb:YLF sample at 1080nm where absorption in $Yb^{3+}$ is zero. The correlation of the doping concentration with the fit background absorption as seen in Fig. 6.2 shows a good correlation that with increased doping, there is decreased background absorption. This is consistent with the argument that the starting material

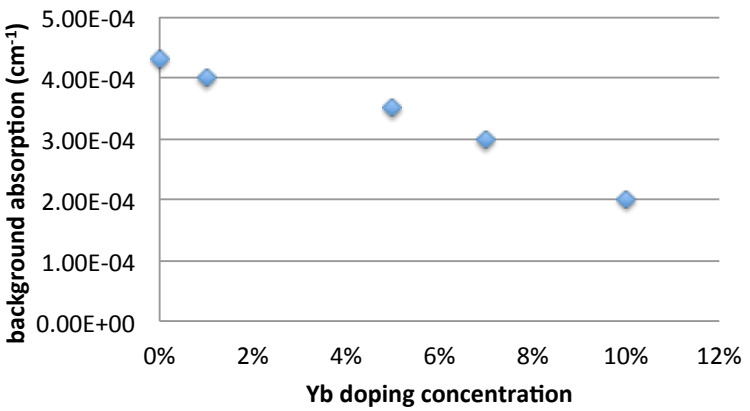


Figure 6.2: Background absorption vs. doping concentration

for the host contains the heating impurities.

Trace element analysis was performed on the five AC Materials samples (0%, 1%, 5%, 7% and 10% wt. Yb:YLF) and one sample (5% wt. Yb:YLF) grown at the University of Pisa, Italy which did not exhibit cooling, properties of each tabulated in Table 6.1 for reference. It is important to note that while this sample did not cool, several other samples from Pisa did cool, including all of the 5% wt. Yb:YLF record results previously mentioned, exhibiting the variation during growths. Following the same methodology as in Sec. 6.2 for preparation of each sample, solutions were created and analyzed in the X-series Q-ICP mass spectrometer. Without a priori knowledge of which impurities cause heating, it is necessary to search through as many elements for which calibration samples exist. By looking into the transition metals seen in Fig. 6.3, a single element (Fe) stands out, and has a strong correlation to the background absorption measurement, Fig.6.4. This correlation points to iron

| Yb:YLF crystal values | | | |
|---|---|---|---|
| Grown | % wt. doping | $\eta_{eqe}$ | $\alpha_b$ |
| AC Materials | 10% | 99.6(±0.1)% | $2.0(\pm0.5) \times 10^{-4}\text{cm}^{-1}$ |
| | 7% | 99.5(±0.1)% | $3.0(\pm0.5) \times 10^{-4}\text{cm}^{-1}$ |
| | 5% | 99.5(±0.1)% | $3.5(\pm0.5) \times 10^{-4}\text{cm}^{-1}$ |
| | 1% | 99.5(±0.1)% | $4.0(\pm0.5) \times 10^{-4}\text{cm}^{-1}$ |
| | 0% | N/A | $4.3(\pm0.5) \times 10^{-4}\text{cm}^{-1}$ |
| Pisa | 5% | 97(±0.5)% | $6.5(\pm0.5) \times 10^{-3}\text{cm}^{-1}$ |

Table 6.1: Cooling efficiency values for elemental analysis crystals

as the source of background absorption in Yb:YLF. The next step is to understand the origination of the iron impurity, either as impurities in the starting materials or a part of the growth process.

Analysis of the five separate constituents, LiF, $YbF_3$ (99.99%), $YbF_3$ (99.999%), $YF_3$ (99.999%), and $YF_3$ (99.9999%) was completed after being prepared and dis-

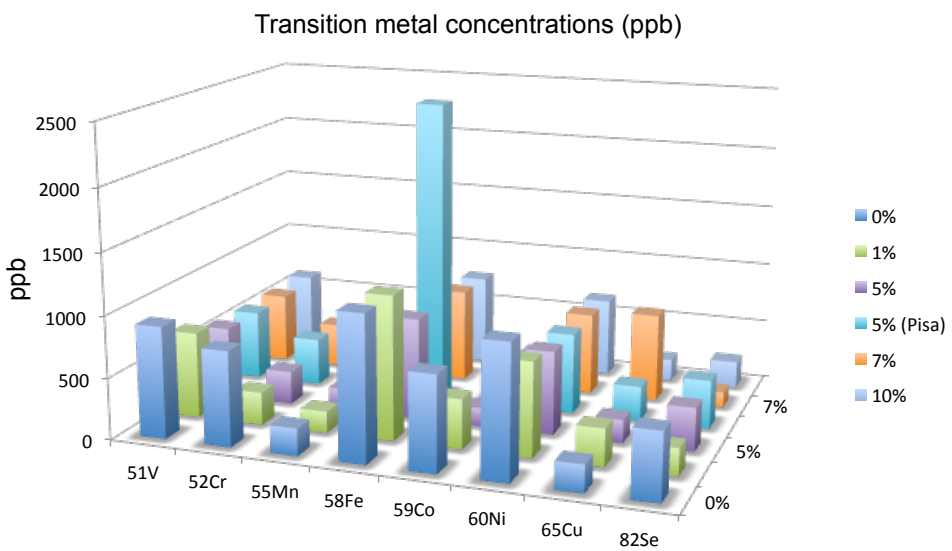


Figure 6.3: Transition metal concentrations in ppb for various doping concentrations of Yb:YLF.

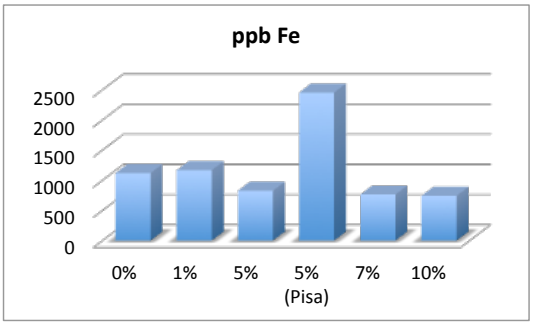


(a) Iron concentration vs. doping

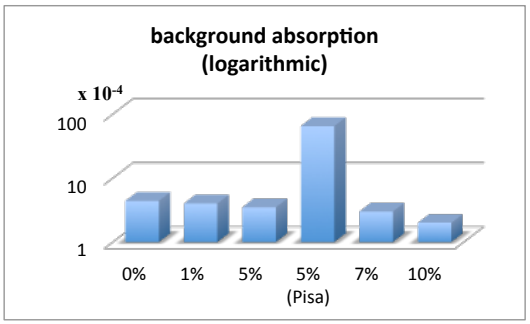


(b) background absorption vs. doping

Figure 6.4: Iron concentration compared with background absorption for various doping concentrations in Yb:YLF.

solved under two conditions. First, the original (un-crushed) sample was dissolved over the period of two weeks with consistent boiling and evaporation of ultra-pure acids to drive off the fluorine and create a dissolvable salt. Second, the original crystal was crushed with a clean mortar and pestle to accelerate the dissolution process and was dissolved over the period of one week. The mortar and pestle have the potential to introduce impurities and cross contaminate successively powdered samples. Extreme care was taken to avoid contamination.

Because increased Fe was consistent with increased background absorption, it is useful to see which constituent contains the most Fe so that it can be processed prior to crystal growth. LiF shows the highest concentration of Fe, as is consistent with increased doping resulting in lower background absorption since $YbF_3$ is the lowest.

It is now possible to make a few estimations on the improvement in background absorption that can be expected if Fe is removed. Fitting the Fe concentration as a function of background absorption shows a logarithmic relationship, Fig. 6.6. From this relationship, it can be assumed that the impurities in the constituents add when mixed together for crystal growth. Therefore, the starting material in YLF add up to 1200 ppb corresponding to a background absorption $\alpha_b = 4.5 \times 10^{-4}\text{cm}^{-1}$. $YF_3$

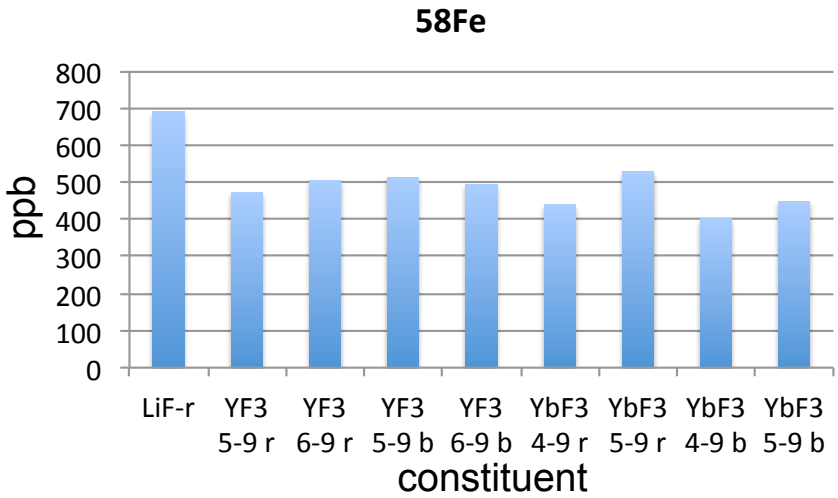


Figure 6.5: Fe concentration for the various tested constituents. Two runs for each were completed coresponding to r & b. 5-9 corresponds to 99.999%, 6-9 corresponds to 99.9999%.

and $YbF_3$ have already gone through a purification process, however LiF can still be purified. If the Fe concentration in LiF can be reduced the effect on background

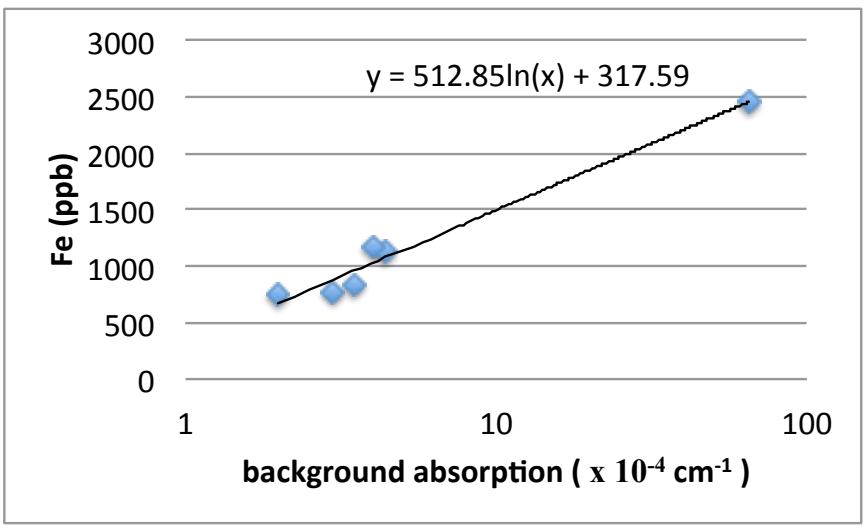


Figure 6.6: Fe concentration vs. logarithmic background absorption.

absorption and hence MAT can be seen in Fig. 6.7 Assuming a 15% wt. $Yb^{3+}$:YLF

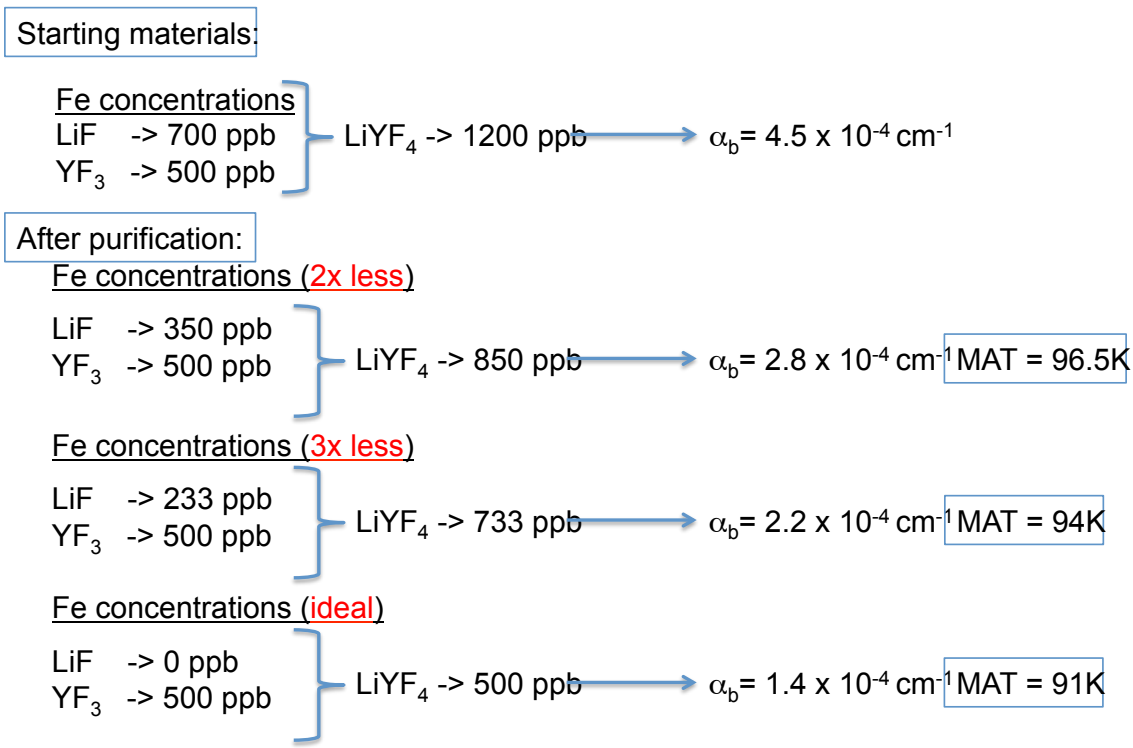


Figure 6.7: Reducing Fe concentration in LiF.

crystal.

When $YbF_3$ substitutionally replaces $YF_3$ there is a further reduction in Fe impurities. By increasing the doping concentration of Yb to 5% or greater, there is a reduction in Fe by ∼380 ppb according to the fit in Fig. 6.6. Therefore, with Fe concentrations at 133 ppb, the background absorption reduces to $\alpha_b = 6.84 \times 10^{-5}\text{cm}^{-1}$, pushing MAT to 80 K.

# Chapter 7

# Conclusions

## 7.1 Conclusions

In this dissertation, I have presented the advancements in optical refrigeration which reached the coldest temperature to date, 114 K, for any solid-state refrigeration by using a 10% doped $Yb^{3+}$:YLF crystal with clear potential to cool to 93 K. This work achieved record cooling by taking advantage of the E4-E5 Stark-manifold resonance of the $Yb^{3+}$ ion, preserved when utilizing a crystal host which leads to increased absorption and improved cooling. A crystal host has qualities advantageous for the creation of an all solid-state optical cryocooler such as low phonon energy, high doping concentrations, high thermal conductivity, non-hygroscopic, and good mechanical hardness.

The cooling mechanism was discussed and is simply characterized by the ideal cooling efficiency, Eq. 2.1. Two more terms were added to complete the true cooling efficiency, $\eta_{ext}$ and $\eta_{abs}$ to account for parasitic background absorption and non-resonant reabsorption. Modeling the performance of the 5% and 10% $Yb^{3+}$:YLF crystals show the possibility of cooling to 110 K and 93 K respectively, far below the

NIST defined cryogenic temperature, 123K, when pumping at 1020nm corresponding to the E4-E5 transition in the $Yb^{3+}$ manifold. Cooling experiments achieved the minimum achievable temperature for a 5% $Yb^{3+}$:YLF crystal at 118 k and showed cooling in the 10% $Yb^{3+}$:YLF crystal to 114 K.

In order to achieve the current record cooling, several challenges were overcome. Firstly, high purity crystals were grown by the Czochralski technique at the University of Pisa, Italy [23] [24], and at AC Materials, Inc. with low parasitic background absorption. Crystals have carefully polished surfaces to remove any inclusions which may create heating, and were cut at Brewster angle to increase the pump transmission. Next, in order to see the greatest drop in temperature, external heat loads were minimized. This was accomplished by designing and machining a clamshell, closely surrounding the crystal and lined with a solar-selective (i.e. low emissivity) coating, Maxorb, to reduce the radiative load by a factor of 6. The clamshell also provided a way to safely support the crystal on small glass fibers to minimize the conductive load. The entire structure was placed inside a vacuum chamber and pumped down to $10^{-6}$ torr to remove the convective load.

With the heat load minimized, two methods to increase the absorbed power through photon trapping were used. Placing the sample in a resonant cavity allows for high absorption ($89\pm3\%$) of the incident pump power, but requires pump stability and control over one of the mirrors to continuously optimize the cavity. Also, the input coupler reflectivity must be impedance matched. Using a non-resonant cavity removed the stability requirements and impedance matching, but also reduced absorption. The non-resonant cavity gave the best cooling performance with maximally-possible 30W of absorbed power at 1020nm, reaching 114 K in a single stage from room temperature, a temperature drop of 185 K, with $\sim$190mW of heat lift.

This result is the coldest temperature reached without the use of mechanical

refrigerators or liquid cryogens, however it is not the coldest temperature this crystal is expected to reach. With optimized heat load management, a temperature of $\sim 93$ K is predicted. Improvements in crystal purity show promise towards reaching the next goal of $LN_2$ temperature of 77 K. The background absorption impurity iron (Fe) was identified and estimates of the cooling improvements afforded by its removal were undertaken, showing cooling to 80 K is within reach.

With cryogenic cooling in place, implementation of a device has begun. Optical isolation from a heat load is paramount for applications due to the significant fluorescence power of the crystals. Several thermal links were designed and analyzed in Zemax to optimize the optical rejection. Two simple 90° thermal links were implemented and verify the Zemax calculations with ∼93% optical isolation. One of the links, intentionally designed for high thermal conductivity using sapphire, shows excellent properties for cooling an applied load. By Van Der Waals bonding a link to the cooling crystal, no thermal barrier exists between the cooling crystal and the link end.

# Chapter 8

# Future Work

Several directions for future work exist. The important immediate steps are: (1) bonding a device directly to the thermal link and show useful operation, (2) implement a full design of an all solid-state optical cryocooler accounting for possible pumping schemes and reducing the physical size of a device, and (3) removing impurities from the starting materials for improved cooling toward 77 K. Beyond the immediate goals, it is important to consider the overall wall-plug efficiency of a device. Currently fluorescent photons are absorbed and the energy is extracted in the form of heat. By exchanging the heat removal for electrical power generation, it is possible to recycle the photon energy and reduce the overall power consumption of a final device. Section 8.5 of the book Optical Refrigeration book [24] discusses the coefficient of performance as cooling approaches Carnot efficiency by recycling photons.

(1) The first step involves modifying the heat load chamber to accept the thermal link, attaching a device and cooling to low temperatures, demonstrating a direct cooling application. The ability to cool to cryogenic temperatures allows for a variety of devices. There is a temperature overlap ( 150K) with high temperature quantum dot

infrared photo-detector (QDIP), quantum dot-in-a-well (DWELL) developed at the center for high technology materials (CHTM, Albuquerque) and high temperature superconducting quantum-interference devices (SQUIDS).

(2) Following the direct cooling verification of a device, it is necessary to design a compact package. Considerations for the design of a compact all solid-state optical cryocooler include:

- a compact design;
- increasing absorbed power through resonant, non-resonant or intra-cavity cooling;
- maintain a high vacuum to reduce convective load;
- clamshell with low emissivity coating to reduce radiative load;
- thermally isolating support for the crystal;
- integration of a sensor with a cold-finger thermally linking the crystal and sensor;
- view-port window for sensor access;
- integration of a pump fiber laser and fluorescence collection fiber into a single umbilical cord;
- and external mode-matching for the fiber-coupled pump laser.

The most promising advancement for miniaturization is the development of a new optically pumped semiconductor laser (OPSL) pump source. Proof of demonstration has been accomplished for intra-cavity cooling of Yb:YLF inside a vertical external cavity surface emitting laser (VECSEL) [62, 63, 64]. Moving intra-cavity cooling from

proof of concept to cryogenic temperatures will help miniaturize a device. Further improvements are aided by collaboration with Jeff Cederberg at Sandia National Labs (SNL), a highly accomplished MOCVD grower. OPSL's can be designed for a desired wavelength and can provide very high intra-cavity power, leading to high absorbed power in the $Yb^{3+}$:YLF crystal. Fig. 8.1 gives a diagram of this cavity containing

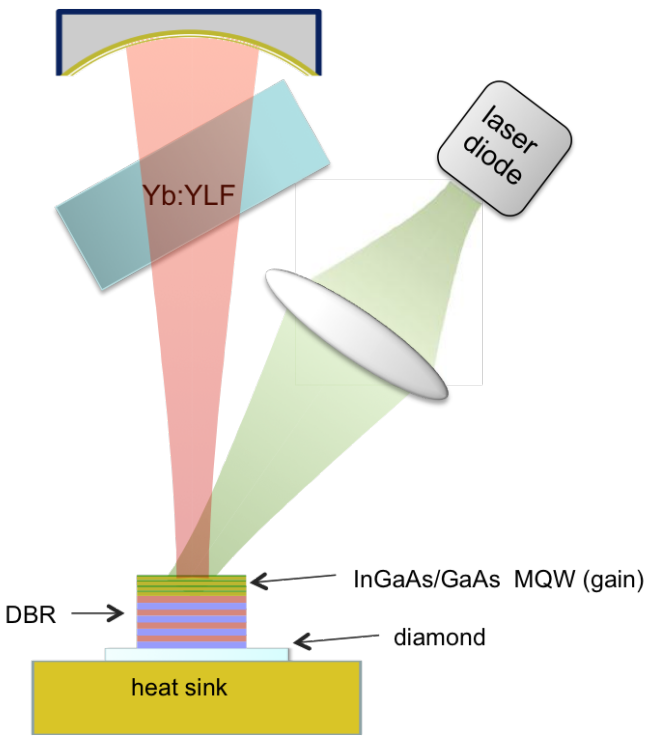


Figure 8.1: Intra-cavity design utilizing an optically pumped semiconductor laser (OPSL), more specifically a MQW-DBR (multiple quantum well, distributed Bragg reflector). The diamond is an efficient heat spreader with high thermal diffusivity. The crystal is integrated directly into the laser cavity for cooling.

the Yb:YLF crystal to be cooled. The OPSL can then be directly integrated into a new chamber design (Fig. 8.2). This design has each component integrated such that sensor cooling via the cold-finger is accomplished by simply providing power to the diode laser.

(3) The final area of improvement involves increasing absorption along with re-

duction of impurities that cause parachutic heating. A crystalline host has already shown resonant absorption enhancement over amorphous glass hosts, but the second advantage, stoichiometrically allowed high doping concentrations, has yet to be examined in detail. Thus far, increasing to 10% wt. Yb:YLF has only shown cooling improvement. Moving forward to improve cooling, the next step is to find the optimal doping concentration. By repeating measurements for 15%, 20%, and 25% (or higher) wt. $Yb^{3+}$:YLF, increased cooling is anticipated until quenching occurs. Quenching is the process of Coulomb energy transfer from an excited $Yb^{3+}$ ion to a train of neighboring ions, eventually resulting in a non-radiative transition caused by energy transfer to an impurity. Quenching is minimized when the separation of ions is increased. Higher doping increases cooling efficiency through increased resonant absorption, but has a detrimental effect when it increases quenching by forcing the spatial separation to decrease. Finding the optimal doping concentration maximizes

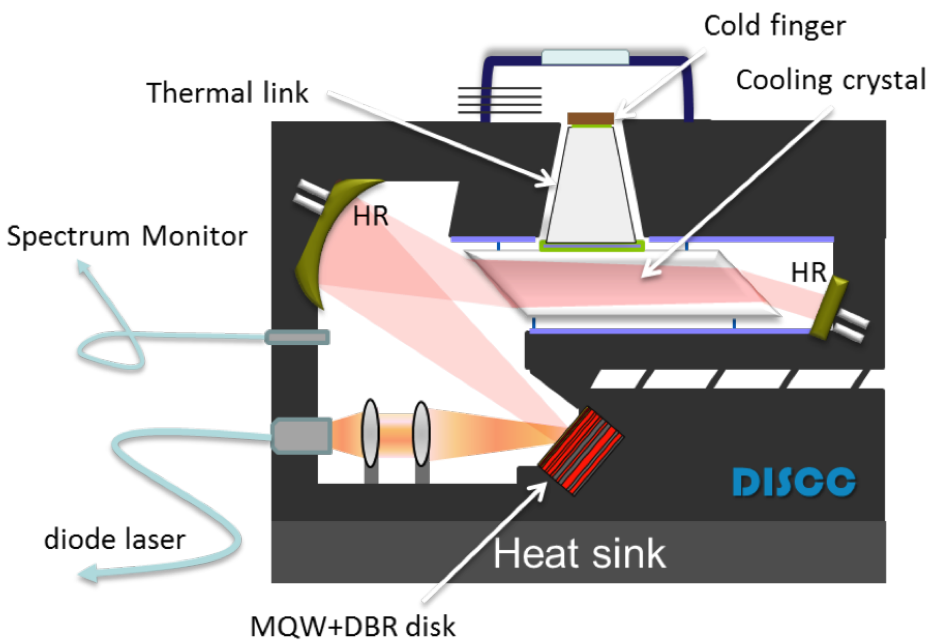


Figure 8.2: An example of an integrated all solid-state optical cryocooler, where the intra-cavity design utilizing the same MQW-DBR as Fig. 8.1 is implemented.

cooling.

Reducing impurities has begun by identifying Fe as a source of background absorption, however others undoubtedly exist. Direct measurement of impurities through mass spectrometry is an important step, however, not all impurities will reduce cooling efficiency, so it is necessary to find those with absorption cross-section that overlaps with the emission of Yb in YLF and the magnitude of absorption. Since absorption varies by host, it will require intentional doping of impurities into YLF, measuring absorption spectra, and classifying those that reduce cooling efficiency. The final step is to locate the source of the impurities and reduce them. This entirely depends on which impurities are found and is therefore difficult to speculate, but the first step is looking at the starting materials, the purification of which can be performed through a collaboration with Markus Hehlen at Los Alamos National Labs (LANL).

# Appendices

# Appendix A

# Differential luminescence thermometry (DLT)

Differential luminescence thermometry (DLT) was used as a sensitive, non-contact measurement of temperature, because thermal (bolometric) cameras become ineffective at T < 250K. Temperature-dependent emission spectra S($\lambda$,T) were obtained in real time and referenced to a corresponding spectrum at a starting temperature $T_0$. The normalized differential spectrum is defined as,

$$\Delta S(\lambda, T, T_0) = \frac{S(\lambda, T)}{\int S(\lambda, T) d\lambda} - \frac{S(\lambda, T_0)}{\int S(\lambda, T_0) d\lambda} \tag{A.1}$$

Normalization to an integrated area or spectral peak was performed to eliminate the effects of input power fluctuations. The saturation of pump absorption could be ignored, as we estimate it to be at least an order of magnitude below saturation intensity. Measured differential spectra for $Yb^{3+}$:YLF are shown in Fig. A.1 for $T_0$ = 300 K. As temperature decreases, the overall spectrum to redshifts, therefore the sign of the temperature change ($\Delta T = T - T_0$) is inferred from the spectral shape. The scalar DLT signal is the absolute area of the differential spectrum:

$$S_{DLT}(T, T_0) = \int_{\lambda_1}^{\lambda_2} d\lambda |\Delta S(\lambda, T, T_0)|, \tag{A.2}$$

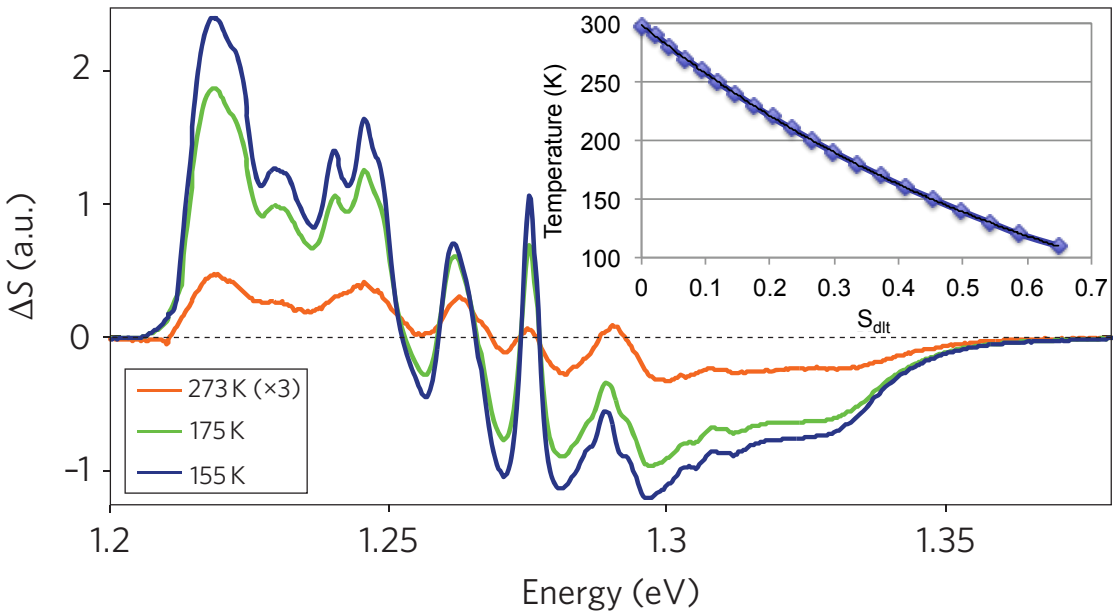


Figure A.1: Measured DLT spectra for the record cooling result. In the upper right is the calibration generated in a separate, carefully controlled, experiment from room temperature to 110K.

where the limits of integration bracket the spectral emission of the $Yb^{3+}$:YLF, eliminating possible contributions from spurious laser line scatter. This signal was converted to an absolute temperature through a separate calibration process. The values of $S_{DLT}(T, T_0)$ are fit with the calibration curve,

$$T = 42.133 \times S_{DLT}^4 - 144.19 \times S_{DLT}^3 + 311.92 \times S_{DLT}^2 - 444.8 \times S_{DLT} + 298.78. \quad \text{(A.3)}$$

The sample was mounted in an optical cryostat where unpolarized fluorescence spectra were recorded as a function of temperature. The geometry closely mimics the laser cooling set-up to mitigate the effect of fluorescence reabsorption. Sample fluorescence was collected through a multimode 600-mm core diameter fibre that was used for both calibration and cooling experiments. The resultant calibration curve, together with a polynomial fit, is shown in the inset of Fig. A.1.

DLT is intrinsically a local probe of temperature. In our experiments, however, we detected the bulk (spatially uniform) temperature of the sample due to (i) a multi-pass pumping geometry that illuminates nearly the entire sample volume and (ii) high thermal conductivity in the YLF crystal, which diminishes any remaining thermal gradients resulting from non-uniform pumping within less than a second (which is more than an order of magnitude shorter than the thermal response time of the experiment [14]). Temperature homogeneity was further veried by imaging the entire sample with a thermal camera at a small temperature drop ($\sim$10°).

# Appendix B

# Yb:YLF properties

Table B.1: Yb:YLF properties.

| Yb:YLF properties | |
|---|---|
| Crystal structure | Tetragonal |
| Point group | I41/a |
| Lattice parameters | a = 5.164 Å, c = 10.741 Å |
| Thermal expansion | $4\times10^{-6}$ / C |
| Thermal conductivity | 4.36 W/mK |
| Density | 3.95 g/cm$^3$ |
| Mohs' hardness | 5 |
| Melting temperature | 825 °C |
| Transmission range | 0.2-5 $\mu$m |
| Refractive indices ($\lambda$ =1.06 $\mu$m) | $n_o$ = 1.448, n$-e$ = 1.470 |
| $dn_o/dT$ | -2.0$\times10^{-6}$ / K |
| $dn_e/dT$ | -4.1$\times10^{-6}$ / K |
| Fluorescence lifetime | 2.1 ms |
| Emission cross section | 7.5x10$^{-21}$ cm$^2$ @1017nm, E//c |
| Emission bandwidth | 60 nm |
| Absorption cross section | 10.6x10$^{-21}$ cm$^2$ @959 nm, E//c |

# Appendix C

# IPG Photonics fiber laser properties

| IPG Photonics YLR-50-1020-LP custom fiber laser<br>Serial # PL1007983 | | |
|---|---|---|
| | **Specification** | **Test Results** |
| **Optical Characteristics** | | |
| Nominal Output Power (W) | >30 | >50 |
| Stable Output Power Range (W) | 3 – 30 | 3 – 50 |
| Operational Wavelength in Vacuum (nm) | 1019 – 1021 | 1020.1 |
| Bandwidth (nm) | 0.5 | <0.5 |
| Output Polarization State | Linear | Linear |
| Polarization Extinction Ratio (dB) | >17 | >17 |
| Operation Mode | CW | CW |
| Power Instability (Over 4 hours) | <3 | <3 |
| Short-Term Power Instability (%) | <2 | <2 |
| In Frequency Range (1kHz – 20MHz) | | |
| Optical Output Residual Pump Power (dB) | <-50 | <-50 |
| **Optical Output** | | |
| Output Fiber Type | PM SM Panda | PM SM Panda |
| Output Fiber Length (m) | 2 | 2 |
| Output Termination | Collimator | Collimator |
| Beam Quality ($M^2$) | < 1.1 | <1.1 |
| **Electrical Characteristics** | | |
| Supply Voltage for Laser Driver (VAC) | 100 – 240 | 100 – 240 |
| nominal Level (%) | – | 96 |
| Maximum Level (%) | – | 100 |

Table C.1: IPG fiber laser specifications

# References


[1] Steven Chu, Claude Cohen-Tannoudji, and William D. Phillips. The nobel prize in physics. `http://www.nobelprize.org/nobel_prizes/physics/laureates/1997/`. Accessed: 02/19/2013.

[2] G Mills, J Fleming, Z. Wei, and J. Turner-Valle. Optical cryocooling and the effect of dielectric mirror leakage. Presented at Earth Science Technology Conference, Pasadena, California, June 2002.

[3] M. Behringer, M. Philippens, W. Teich, A. Schmitt, S. Morgott, J. Heerlein, G. Herrmann, J. Luft, G. Seibold, J. Biesenbach, T. Brand, and M. Marchiano. More brilliance from high-power laser diodes. In M. Fallahi & J. V. Moloney, editor, *Society of Photo-Optical Instrumentation Engineers (SPIE) Conference Series*, volume 4993 of *Society of Photo-Optical Instrumentation Engineers (SPIE) Conference Series*, pages 68–76, June 2003.

[4] G. G. Stokes. On the Change of Refrangibility of Light. *Royal Society of London Philosophical Transactions Series I*, 142:463–562, 1852.

[5] P. Pringsheim. Zwei bemerkungen über den unterschied von lumineszenz und temperaturstrahlung. *Zeitschrift für Physik*, (57):739–746, 1929.

[6] L. Landau. On the thermodynamics of photoluminescence. *J. Phys. (Moscow)*, (10):503–506, 1946.

[7] A. Kastler. Quelques suggestions concernant la production optique et la dtection optique d'une ingalit de population des niveaux de quantification spatiale des atomes: Application  l'exprience de stern et gerlach et  la rsonance magntique. *J. Phys. Radium*, 11:255–265, 1950.

[8] R. I. Epstein, M. I. Buchwald, B. C. Edwards, T. R. Gosnell, and C. E. Mungan. Observation of laser-induced fluorescent cooling of a solid. *Nature*, 377:500–503, oct 1995.

[9] Stefano Bigotta, Daniela Parisi, Lucia Bonelli, Alessandra Toncelli, Mauro Tonelli, and Alberto Di Lieto. Spectroscopic and laser cooling results on $Yb^{3+}$-doped BaY2F8 single crystal. *Journal of Applied Physics*, 100(1):013109–013109–7, July 2006.

[10] S. Bigotta, A. Di Lieto, A. Toncelli, M. Tonelli, D. Seletskiy, M P Hasselbeck, M. Sheik-Bahae, and R I Epstein. Laser cooling of solids: New results with single fluoride crystals. *Nuovo Cimento Della Societa Italiana Di Fisica BGeneral Physics Relativity Astronomy and Mathematical Physics and Methods*, 122(6-7):685–694, 2007.

[11] S. R. Bowman and C. E. Mungan. New materials for optical cooling. *Appl. Phys. B*, 71:807811, 2000.

[12] A. Mendioroz, J. Fernandez, M. Voda, M. Al-Saleh, and R. Balda. Anti-stokes laser cooling in $Yb^{3+}$-doped $KPb_2Cl_5$ crystal. *Opt. Lett*, 27:15251527, 2002.

[13] C. E. Mungan, M. I. Buchwald, B. C. Edwards, R. I. Epstein, and T. R. Gosnell. Laser cooling of a solid by 16K starting from room temperature. *Phys. Rev. Lett.*, 78:10301033, 1997.

[14] J. Thiede, J. Distel, S. R. Greenfield, and R. I. Epstein. Cooling to 208k by optical refrigeration. *Appl. Phys. Lett.*, 86:154107, 2005.

[15] N. J. Condon, S. R. Bowman, S. P. OConnor, R. S. Quimby, and C. E. Mungan. Optical cooling in $Er^{3+}$:$KPb_2Cl_5$. *Opt. Express*, 17:54665472, 2009.

[16] C. Hoyt. *Laser cooling in thulium-doped solids*. Doctoral dissertation, University of New Mexico, Albuquerque, NM, USA, May 2003.

[17] C. W. Hoyt, M. P. Hasselbeck, M. Sheik-Bahae, R. I. Epstein, S. Greenfield, J. Thiede, J. Distel, and J. Valencia. Advances in laser cooling of thulium-doped glass. *Journal of the Optical Society of America B Optical Physics*, 20:1066–1074, May 2003.

[18] C. W. Hoyt, M. Sheik-Bahae, R. I. Epstein, B. C. Edwards, and J. E. Anderson. Observation of anti-stokes fluorescent cooling in thulium-doped glass. *Phys. Rev. Lett*, page 36003603, 2000.

[19] Wendy Patterson, Stefano Bigotta, Mansoor Sheik-Bahae, Daniela Parisi, Mauro Tonelli, and Richard Epstein. Anti-Stokes luminescence cooling of $Tm^{3+}$doped $BaY_2F_8$. *Optics Express*, 16(3):1704–1710, February 2008.

[20] J. Fernandez, A. J. Garcia-Adeva, and R. Balda. Anti-stokes laser cooling in bulk erbium-doped materials. *Phys. Rev. Lett.*, 97:033001, 2006.

[21] A. J. Garcia-Adeva, R. Balda, and J. Fernández. Anti-Stokes laser cooling in erbium-doped low-phonon materials. In *Society of Photo-Optical Instrumentation Engineers (SPIE) Conference Series*, volume 6461 of *Presented at the Society of Photo-Optical Instrumentation Engineers (SPIE) Conference*, March 2007.

[22] Carl E. Mungan and Timothy R. Gosnell. Laser cooling of solids. volume 40 of *Advances In Atomic, Molecular, and Optical Physics*, pages 161 – 228. Academic Press, 1999.

[23] S. Bigotta. *Energy transfer and cooling processes in rare-earth doped insulating crystals*. Doctoral dissertation, Universitá di Pisa, Pisa, Italy, Nov 2006.

[24] R. Epstein and M. Sheik-Bahae. *Optical refrigeration: science and applications of laser cooling of solids*. Wiley-VCH, 2009.

[25] D. V. Seletskiy, S. D. Melgaard, S. Bigotta, A. di Lieto, M. Tonelli, and M. Sheik-Bahae. Laser cooling of solids to cryogenic temperatures. *Nature Photonics*, 4:161–164, March 2010.

[26] Mansoor Sheik-Bahae and Richard I. Epstein. Optical refrigeration. *Nat Photon*, 1(12):693–699, December 2007.

[27] M. Sheik-Bahae and R. I Epstein. Laser cooling of solids. *Laser & Photonics Reviews*, 3(12):67–84, February 2009.

[28] D. V. Seletskiy, S. Melgaard, M. Sheik-Bahae, S. Bigotta, A. Dilieto, and M. Tonelli. Laser cooling of a semiconductor load using a Yb:YLF optical refrigerator. In *Society of Photo-Optical Instrumentation Engineers (SPIE) Conference Series*, volume 7614 of *Presented at the Society of Photo-Optical Instrumentation Engineers (SPIE) Conference*, February 2010.

[29] R. I Epstein, J. J Brown, B. C Edwards, and A. Gibbs. Measurements of optical refrigeration in ytterbium-doped crystals. *Journal of Applied Physics*, 90(9):4815–4819, November 2001.

[30] A. Mendioroz, A J Garcia, R. Balda, J L Adam, and Fernandez. Anti-stokes laser-induced internal cooling of $Yb^{3+}$-doped glasses. *Physical Review B*, 62(5):3213–3217, 2000.

[31] Denis V. Seletskiy, Seth D. Melgaard, Alberto Di Lieto, Mauro Tonelli, and Mansoor Sheik-Bahae. Laser cooling of a semiconductor load to 165 k. *Opt. Express*, 18(17):18061–18066, Aug 2010.

[32] S. Bigotta, L. Bonelli, D. Parisi, A. Toncelli, M. Tonelli, and A. D. Lieto. Observa- tion of laser cooling in $Yb^{3+}$-doped single crystals. 2nd EPS-QEOD Europhoton Conference, 2006.

[33] S. Melgaard, D. Seletskiy, M. Sheik-Bahae, S. Bigotta, A. di Lieto, M. Tonelli, and R. Epstein. Spectroscopy of Yb-doped YLF crystals for laser cooling. In *Society of Photo-Optical Instrumentation Engineers (SPIE) Conference Series*, volume 7614 of *Presented at the Society of Photo-Optical Instrumentation Engineers (SPIE) Conference*, February 2010.

[34] D. V. Seletskiy, M. P. Hasselbeck, M. Sheik-Bahae, R. I. Epstein, S. Bigotta, and M. Tonelli. Cooling of Yb:YLF using cavity enhanced resonant absorption. *Proc. SPIE 6907*, 2008.

[35] L.A. Riseberg and H.W. Moos. Multiphonon orbit-latice relaxation of excited states of rare-earth ions in crystals. *Phys. Rev.*, 174:429, 1968.

[36] Joseph T. Verdeyen. *Laser electronics / Joseph T. Verdeyen*. Prentice-Hall, Englewood Cliffs, N.J. :, 1994.

[37] D. E. McCumber. Einstein relations connecting broadband emission and absorption spectra. *Phys. Rev.*, 136:A954–A957, 1964.

[38] R. C. Powerl. *Physics of Solid-State Laser Materials: Atomic, Molecular, and Optcial Physics*, volume 1. Springer-Verlag, New York, 1998.

[39] G. Lei, J. E. Anderson, M. I. Buchwald, B. C. Edwards, and R. I. Epstein. Determination of spectral linewidths by voigt profiles in $Yb^{3+}$-doped fluorozirconate glasses. *Phys. Rev. B*, 57(13):7673–7678, Apr 1998.

[40] Wolfgang Demtroder. *Laser Spectroscopy: Basic Concepts and Instrumentation*, volume 5. Springer-Verlag, July 1981.

[41] M.P. Hehlen, R.I. Epstein, and H. Inoue. Model of laser cooling in the $Yb^{3+}$-doped fluorozirconate glass ZBLAN. *Phys. Rev. B*, 75:144302, 2007.

[42] General Electric. Section 410.2. In *Fluid Flow Data Book*. Genium Publishing, 1982.

[43] B. Imangholi, M. P. Hasselbeck, D. A. Bender, C. Wang, M. Sheik-Bahae, R. I. Epstein, and S. Kurtz. Differential luminescence thermometry in semiconductor laser cooling. In M. Osinski, F. Henneberger, & Y. Arakawa, editor, *Society of Photo-Optical Instrumentation Engineers (SPIE) Conference Series*, volume 6115 of *Presented at the Society of Photo-Optical Instrumentation Engineers (SPIE) Conference*, pages 215–220, March 2006.

[44] W. Patterson, E. Soto, M. Fleharty, and M. Sheik-Bahae. Differential luminescence thermometry in laser cooling of solids. In *Society of Photo-Optical Instrumentation Engineers (SPIE) Conference Series*, volume 6461 of *Presented at the Society of Photo-Optical Instrumentation Engineers (SPIE) Conference*, March 2007.

[45] D. V. Seletskiy, M. P. Hasselbeck, M. Sheik-Bahae, and R. I. Epstein. Fast differential luminescence thermometry. In *Society of Photo-Optical Instrumentation Engineers (SPIE) Conference Series*, volume 7228 of *Presented at the Society of Photo-Optical Instrumentation Engineers (SPIE) Conference*, February 2009.

[46] A. E. Siegman. *Lasers*. University Science Books, 1986.

[47] D. V. Seletskiy, M. P. Hasselbeck, and M. Sheik-Bahae. Resonant cavity-enhanced absorption for optical refrigeration. *Appl. Phys. Lett.*, 96:181106, 2010.

[48] D. V. Seletskiy, S. D. Melgaard, M. P. Hasselbeck, M. Sheik-Bahae, R. I. Epstein, S. Bigotta, and M. Tonelli. Recent progress in laser cooling via resonant cavity. In *Society of Photo-Optical Instrumentation Engineers (SPIE) Conference Series*, volume 7228 of *Presented at the Society of Photo-Optical Instrumentation Engineers (SPIE) Conference*, February 2009.

[49] W. Wan, Y. Chong, L. Ge, H. Noh, A. D. Stone, and H. Cao. Time-Reversed Lasing and Interferometric Control of Absorption. *Science*, 331:889–, February 2011.

[50] G. Mills and A. Mord. Performance modeling of optical refrigerators. *Cryogenics*, 46:176182, 2006.

[51] Y. P. Varshni. Temperature dependence of the energy gap in semiconductors. *Physica*, 34(1):149 – 154, 1967.

[52] R. L. Aggarwal, D. J. Ripin, J. R. Ochoa, and T. Y. Fan. Measurement of thermo-optic properties of Y3Al5O12, Lu3Al5O12, YAIO3, LiYF4, LiLuF4, BaY2F8, KGd(WO4)2, and KY(WO4)2 laser crystals in the 80300k temperature range. *Journal of Applied Physics*, 98(10):103514–103514–14, November 2005.

[53] W. M. Patterson, M. Sheik-Bahae, R. I. Epstein, and M. P. Hehlen. Model of laser-induced temperature changes in solid-state optical refrigerators. *Journal of Applied Physics*, 107(6):063108, 2010.

[54] Galina Nemova and Raman Kashyap. Temperature distribution in laser-cooled rare-earth doped solid-state samples. *J. Opt. Soc. Am. B*, 27(12):2460–2464, Dec 2010.

[55] Gang Lei, J.E. Anderson, M.I. Buchwald, B.C. Edwards, R.I. Epstein, M.T. Murtagh, and Jr. Sigel, G.H. Spectroscopic evaluation of yb3+-doped glasses for optical refrigeration. *Quantum Electronics, IEEE Journal of*, 34(10):1839 –1845, oct 1998.

[56] C. E. Mungan, M. I. Buchwald, B. C. Edwards, R. I. Epstein, and T. R. Gosnell. Internal laser cooling of yb[sup 3 + ]-doped glass measured between 100 and 300 k. *Applied Physics Letters*, 71(11):1458–1460, 1997.

[57] J. Fernandez, a. Mendioroz, A. J. Garc?a, R. Balda, J. L. Adam, and M. A. Arriandiaga. On the origin of anti-stokes laser-induced cooling of $yb^{3+}$-doped glass. *Optical Materials*, 16(1-2):173 – 179, 2001.

[58] Michael P. Hasselbeck, Mansoor Sheik-Bahae, and Richard I. Epstein. Effect of high carrier density on luminescence thermometry in semiconductors. pages 646107–646107–5, 2007.

[59] W. M. Patterson, D. V. Seletskiy, M. Sheik-Bahae, R. I. Epstein, and M. P. Hehlen. Measurement of solid-state optical refrigeration by two-band differential luminescence thermometry. *J. Opt. Soc. Am. B*, 27(3):611–618, Mar 2010.

[60] John Parker, David Mar, Steven Von der Porten, John Hankinson, Kevin Byram, Chris Lee, Michael K. Mayeda, Richard Haskell, Qimin Yang, Scott Greenfield, and Richard Epstein. Thermal links for the implementation of an optical refrigerator. *Journal of Applied Physics*, 105(1):013116–013116–11, January 2009.

[61] Wendy M. Patterson, Peter C. Stark, Thomas M. Yoshida, Mansoor Sheik-Bahae, and Markus P. Hehlen. Preparation and characterization of high-purity metal fluorides for photonic applications. *Journal of the American Ceramic Society*, 94(9):2896–2901, 2011.

[62] Alexander R. Albrecht, Denis V. Seletskiy, Jeffrey G. Cederberg, Alberto Di Lieto, Mauro Tonelli, Jerome V. Moloney, Ganesh Balakrishnan, and Mansoor Sheik-Bahae. Intracavity laser cooling using a vecsel. pages 827505–827505–6, 2012.

[63] Alexander R. Albrecht, Mohammadreza Ghasemkhani, Jeffrey G. Cederberg, Denis V. Seletskiy, Seth Melgaard, and Mansoor Sheik-Bahae. Progress towards cryogenic temperatures in intracavity optical refrigeration using a VECSEL. In *Society of Photo-Optical Instrumentation Engineers (SPIE) Conference Series*, volume 8638 of *Presented at the Society of Photo-Optical Instrumentation Engineers (SPIE) Conference*, February 2013.

[64] Mansoor Sheik-Bahae, Mohammadreza Ghasemkhani, Alexander R. Albrecht, Denis V. Seletskiy, Jeffrey G. Cederberg, and Seth Melgaard. Progress towards cryogenic temperatures in intracavity optical refrigeration using a VECSEL. In *Society of Photo-Optical Instrumentation Engineers (SPIE) Conference Series*, volume 8606 of *Presented at the Society of Photo-Optical Instrumentation Engineers (SPIE) Conference*, February 2013.